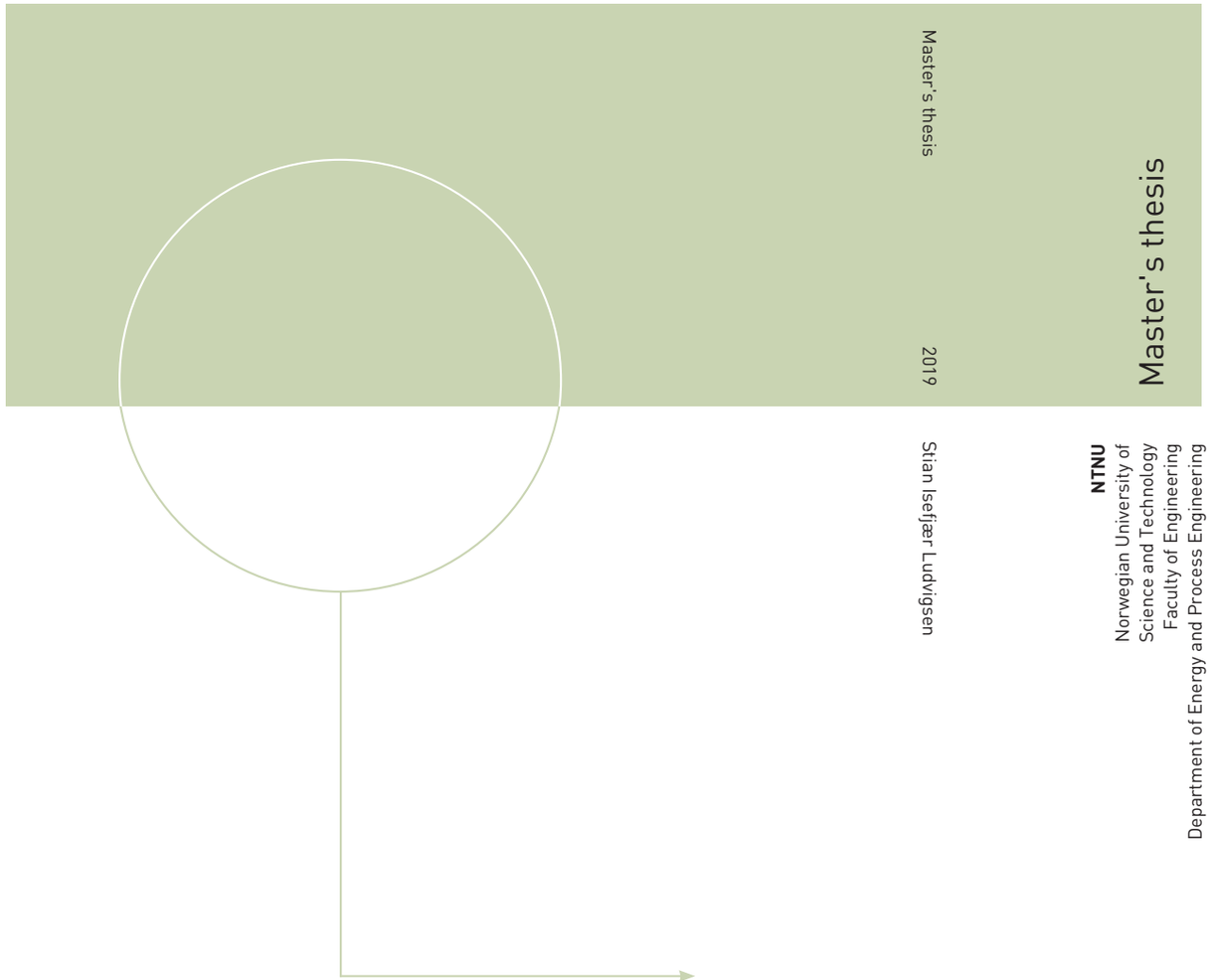

Master's thesis

2019

Stian Isefjær Ludvigsen

NTNU
Norwegian University of
Science and Technology
Faculty of Engineering
Department of Energy and Process Engineering

Stian Isefjær Ludvigsen

Numerical study of curved-mesh tailoring of free-surface shear profile

June 2019

NTNU
Norwegian University of
Science and Technology

NTNU
Norwegian University of
Science and Technology

NTNU
Norwegian University of
Science and Technology

Numerical study of curved-mesh tailoring of free-surface shear profile

Stian Isefjær Ludvigsen

Mechanical Engineering
Submission date: June 2019
Supervisor: Simen Andreas Ådnøy Ellingsen, EPT
Co-supervisor: Are Simonsen, SINTEF

Norwegian University of Science and Technology
Department of Energy and Process Engineering

NTNU

Norwegian University of
Science and Technology

Numerical study of curved-mesh tailoring of free-surface shear profile

Mechanical Engineering
Submission date: June 2019
Supervisor: Simen Andreas Ådnøy Ellingsen, EPT
Co-supervisor: Are Simonsen, SINTEF

Norwegian University of Science and Technology
Department of Energy and Process Engineering

Preface

This master's thesis was carried out during the spring semester of 2019 and was submitted to the Department of Energy and Process Engineering at the Norwegian University of Science and Technology. The master's thesis is submitted as part of the study program Mechanical Engineering, and it comprises of 30ECTS.

I would like to thank my supervisor Simen A. Ådnøy Ellingsen, for guidance and discussions helping me get a better understanding of the physics governing flows passing through curved screens and for giving me feedback on my thesis work. I would also like to thank co-supervisor Are Simonsen, for all the help and guidance in ANSYS Fluent and for fruitful discussions regarding practical and theoretical issues concerning the CFD-model.

I would also like to thank PhD Candidate Benjamin Smeltzer, for providing me with relevant experimental data, and for giving feedback on the CFD-results, and Tufan Arslan, for giving me an introduction on how to use the Vilje cluster for ANSYS Fluent simulations.

Trondheim, June 11, 2019

Stian Isefjær Ludvigsen

Abstract

Curved screens are often used to transform the velocity profile in the test section of experimental facilities. The existing relations for determining the screen shape given the flow conditions upstream and the desired flow conditions in the test section are, unfortunately, limited to moderate changes in the velocity profile. Hence, a lot of time may be spent on trying to determine a screen shape that adequately accurate produces the desired velocity profile. The aim of this thesis is therefore to construct a computational fluid dynamics (CFD) model that accurately simulates flows passing through curved screens within a reasonable amount of time. This model will be used to study how the downstream velocity profile is affected when changing the screen shape/curvature, inlet velocity, and water depth using the commercial CFD solver ANSYS Fluent 19.2.

Resolving all flow structures that are present in flows passing through screens proved to be a computationally intensive task. It was therefore decided to model the flow resistance introduced by a screen using the porous media model (PMM) in ANSYS Fluent, such that the screen was substituted by a porous region. Empirical relations for the pressure drop over screens were used to approximate the loss factors that need to be specified in the PMM.

A closed channel model was created to verify that the PMM accurately modelled the flow obstruction introduced by a physical screen. The verification of the model was performed by comparing the velocity profile resulting from CFD-simulations, using several screen shapes, with the velocity profile predicted by a theoretical relation. This comparison showed that the agreement between the two was almost perfect.

Experimental data provided by PhD Candidate Benjamin Smeltzer was used to validate the CFD-model for open channel flows. Comparison between the measured velocity profile and the profile resulting from the CFD-model showed an adequate agreement between the two.

After the CFD-model had been carefully verified and validated, several cases investigating how certain changes affected the velocity profile downstream of the screen were tested. Simulations showed that:

- Making a screen more convex, as perceived by the flow, results in an even more concave velocity profile and a decrease in the shear in the region near the free-surface.

- Making a screen more concave, as perceived by the flow, results in an even more convex

velocity profile and an increase in the shear in the region near the free-surface.

- For a straight screen, an increase in the angle between the screen normal vector and the streamwise direction results in a greater change in the velocity profile over the screen.
- Increasing the inlet velocity will decrease the change in the velocity profile over the screen.
- Changing the water depth, keeping all other parameters constant, gave no effects on the normalized velocity profile. This result is though not assumed to be general.

Sammendrag

Krummede nettinger blir ofte brukt til å endre hastighetsprofilet i testområdet i eksperimentelle anlegg. De eksisterende uttrykkene som kan brukes til å bestemme formen på nettingen, gitt strømningsforholdene opp- og nedstrøms av testområdet, er dessverre kun gyldig for små endringer i hastighetsprofilet over nettingen. Mye tid kan derfor ende opp med og brukes på å bestemme formen på nettingen som produserer det ønskede hastighetsprofilet med tilstrekkelig nøyaktighet. Målet for denne masteroppgaven er derfor å lage en CFD-modell som kan simulere strømning over krummede nettinger med tilstrekkelig nøyaktighet innen rimelig tid. Denne modellen vil videre brukes til å undersøke hvordan hastighetsprofilet nedstrøms for nettingen endrer seg ved å endre formen på nettingen, innløpshastigheten og vanndybden ved bruk av CFD programmet ANSYS Fluent 19.2.

Å løse opp alle strømningsstrukturene som oppstår i en strømning over en netting viste seg å være en svært tidkrevende beregningsoppgave. Det ble derfor bestemt å modellere strømningsmotstanden som introduseres av en netting ved bruk av porøst medium modellen (PMM) i ANSYS Fluent, hvor nettingen byttes ut med et porøst område. Empiriske sammenhenger for trykktapet over en netting ble brukt til å tilnærme tapsleddene som må spesifiseres i PMM.

En modell for strømning i lukket kanal ble brukt til å verifisere at PMM modellerte strømningsmotstanden til en fysisk netting nøyaktig. Modellen ble verifisert ved å sammenligne hastighetsprofilet fra CFD-simuleringene med hastighetsprofilet predikert av en teoretisk sammenheng. Denne sammenligningen viste en nesten perfekt sammenheng mellom hastighetsprofilene.

Doktorgradsstudenten Benjamin Smeltzer bidro med eksperimentelle data som ble brukt til å validere CFD-modellen for strømning i åpen kanal over en krummet netting. Hastighetsprofilet fra CFD-modellen viste seg å predikere hastighetsprofilet fra de eksperimentelle dataene med tilstrekkelig nøyaktighet.

Etter å ha verifisert og validert CFD-modellen nøye, ble det undersøkt hvordan enkelte endringer påvirket hastighetsprofilet nedstrøms for nettingen. Simuleringene viste at:

- Å gjøre en netting mer konveks, sett av strømningen, resulterer i et mer konkavt hastighetsprofil og reduserer styrken på skjærprofilet nær den frie overflaten.
- Å gjøre en netting mer konkav, sett av strømningen, resulterer i et mer konvekst

hastighetsprofil og øker styrken på skjærprofilet nær den frie overflaten.

- For rette nettinger vil en økning i vinkelen mellom normal vektoren til nettingen og strømningsretningen resultere i en større endring i hastighetsprofilet over nettingen.
- En økning i innløpshastigheten vil redusere endringen i hastighetsprofilet over nettingen.
- Å endre vanndybden, uten å endre andre parametre, viste seg å ikke ha noen effekt på det normaliserte hastighetsprofilet. Dette resultatet er dog ikke antatt å være generelt.

Contents

List of Figures

List of Tables

Nomenclature

Variables and Parameters

d	=	Wire diameter, [m].
l	=	Axis-to-axis spacing between wires in a screen, [m].
σ	=	Screen solidity, [-].
U	=	Mean velocity, $\left[\frac{\mathrm{m}}{\mathrm{s}}\right]$.
ν	=	Kinematic viscosity, $\left[\frac{\mathrm{m}^2}{\mathrm{s}}\right]$.
ρ	=	Fluid density, $\left[\frac{\mathrm{kg}}{\mathrm{m}^3}\right]$
μ	=	Dynamic viscosity, $\left[\frac{\mathrm{kg}}{\mathrm{ms}}\right]$
Re	=	Reynolds number, subscript specify characteristic length, [-].
K	=	Pressure drop coefficient, [-].
B	=	Deflection coefficient, [-].
ψ	=	Stream function, $\left[\frac{m^2}{s}\right]$
γ	=	Effective loss coefficient, [-].
γ_0	=	Mean effective loss coefficient, [-].
θ	=	Angle between screen normal vector and x-axis, [-].
s	=	Resistance variation, [-].
h	=	Channel height/water depth, [m].
α	=	Fourier coefficients, [-].
η	=	Normalized vertical position, [-].
λ, β	=	Shear parameters, [-].
p	=	Pressure, $\left[\frac{\mathrm{kg}}{\mathrm{ms}^2}\right]$.
D	=	Viscous resistance/loss factor, [-].
C	=	Inertial resistance/loss factor, [-].
ϕ	=	Porosity, [-].
$\mathbf{u}$	=	Velocity vector, $\left[\frac{\mathrm{m}}{\mathrm{s}}\right]$.
g	=	Gravitational acceleration, $\left[\frac{\mathrm{m}}{\mathrm{s}^2}\right]$.
Y	=	Volume fraction of a phase, [-].
ς	=	Surface tension, $\left[\frac{\mathrm{kg}}{\mathrm{s}^2}\right]$.

Subscripts

tu	=	Tangential upstream.
td	=	Tangential downstream.
d	=	Downstream.
u	=	Upstream.
q	=	Phase number q.

Abbreviations

NTNU	=	Norwegian University of Science and Technology.
CFD	=	Computational Fluid Dynamics.
i.e.	=	id est meaning that is
e.g.	=	exempli gratia meaning for example.
PMM	=	Porous Media Model.
HPC	=	High Performance Computing.
UDF	=	User Defined Function.
VOF	=	Volume of Fluid.
CSS	=	Continuum Surface Stress.
wrt	=	with respect to.

Chapter 1

Introduction

1.1 Background

Sheared flows are often being studied as useful idealizations of several industrial and environmental flows, e.g. wave propagation at the interface of a fluid subjected to a sheared current. The production of such a flow is often just an initial step of an experimental study, as it often is the effect of the sheared flow, and not how it is generated, that is of interest. The process of producing a specific velocity profile may be a fairly time-consuming process and might not be as straight forward as first thought.

A transformation of the velocity profile may be performed experimentally by introducing an obstruction to the flow that deflects the streamlines. The idea is that a desired velocity profile can be generated by a spatial variation of the flow obstruction, deflecting the flow in such a manner that the desired velocity profile is created. Such obstructions may be rows of parallel cylinders with non-uniform spacing (Owen and Zienkiewcz [23]; Livesey and Turner [20]; McCarthy [22]), screens (Elder [7]; Turner [25]; Castro [3]; Dunn and Tavoularis [6]), tapered honeycombs(Kotansky[16]), and parallel channels in which obstructions adjust the flow rate(Karnik and Tavoularis [15]). Each of these methods has its strengths and weaknesses regarding turbulence production and ability to cause large changes in the velocity profile up- and downstream of the obstruction. Although there have been several attempts at constructing a general theoretical relation relating the up- and downstream flow conditions with the flow obstruction, all of them rely on empirical relations and are mostly restricted to small changes in the velocity profile over the obstruction.

At the wave laboratory in the fluid mechanics building at the Norwegian University of

Science and Technology (NTNU), there is an ongoing study of 3D wave phenomena affected by a sub-surface shear current. The shear current in the laboratory, which set-up is illustrated in figure 1.1, is generated by the use of a curved screen. Today, the screen is adjusted manually until a desired downstream velocity profile is generated. It is therefore desired to get a better understanding of how the produced velocity profile is related to the screen shape. The goal is to get better control of the downstream velocity profile and to save time spent on adjusting the screen in the future if other velocity profiles are desired.

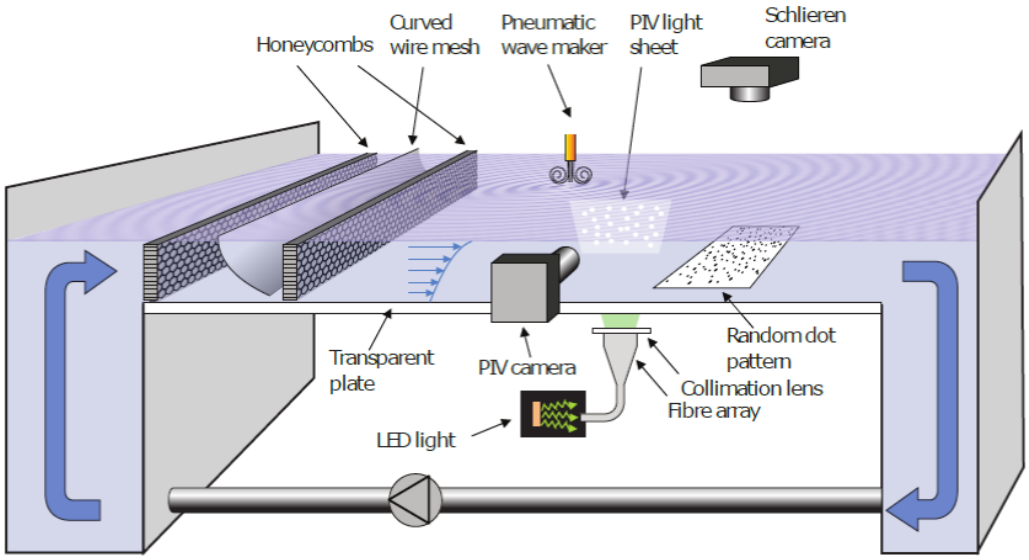

Figure 1.1: Set-up in the wave laboratory (fig. by S.Å.E) [27].

1.1.1 Motivation

An example will be used to motivate this thesis. There may be many reasons why it is desired to transform the velocity profile that is currently available in the test section of a laboratory. For example, to ensure that a component could be operating safely in a given velocity field. So, imagine that it is desired to test the performance of a hydrofoil in a certain velocity profile. The velocity profile in the test section is currently uniform, as illustrated in figure 1.2, while figure 1.3 shows the velocity profile that it is desired to test the performance of the hydrofoil in.

The velocity profile that is currently in the lab may be transformed into the desired profile by placing a screen upstream of the test section. This situation is illustrated in figure 1.4.

Figure 1.2: The current situation in the test section.

Figure 1.3: The velocity profile in which it is desired to test the performance of the hydrofoil.

The desired velocity profile will then be produced by the screen if it has the correct shape, by deflecting the streamlines of the flow such that the desired velocity profile is produced. Although the main objective of the project is to test the performance of the hydrofoil in the given velocity profile, a majority of the time allocated for the project may be spent on determining the correct shape of the screen, such that it will produce the desired velocity profile. A better routine for testing a screen shape without having to reshape the screen and support structure manually is therefore needed, such that less time will be wasted on testing different screen shapes in the future.

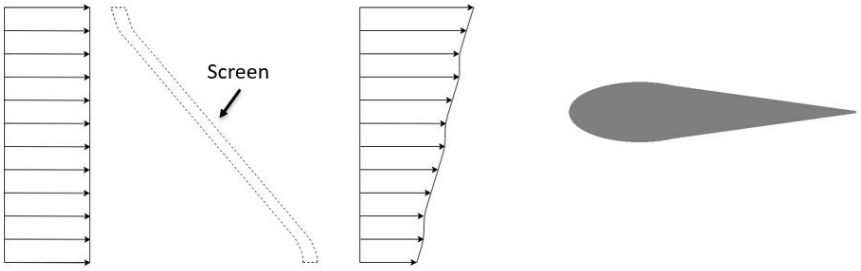

Figure 1.4: The desired velocity profile may be generated by placing a screen upstream of the test section. The screen will transform the uniform profile into the desired profile, if it has the correct shape.

1.2 Research Objectives

The main objective of this thesis is to develop a Computational Fluid Dynamics (CFD) model that accurately simulates laminar flows through curved screens. The idea is that the model can be used to predict the downstream velocity profile resulting from a given screen shape and inlet conditions.

The first step will be to develop a quasi-2D model of one periodic screen length's width using periodic boundary conditions. A periodic screen length's width corresponds to the entity that is repeated in the spanwise direction, an illustration of the replicated entity of square-knitted screens is given in figure 2.1. A model allowing larger spanwise flow structures may be necessary depending on the performance of the quasi-2D model. The CFD-results will be verified and validated using theoretical relations and experimental results.

The CFD-model will then be used to analyze how the velocity profile downstream of the screen is affected by varying:

- Screen shape/curvature.
- Inlet velocity.
- Water depth.

It is desired that these results will give a better insight on how to design a screen such that a desired downstream velocity profile is produced. Version 19.2 of the commercial CFD software ANSYS FLUENT will be used to conduct the CFD-simulations in this thesis. It is also desired that simulations of the CFD-model are time-efficient, such that it may be used as an effective tool for determining the correct screen shape for a given case.

1.3 Chapter outline

To address the research objectives of this thesis, it will start with a chapter presenting the theoretical framework, chapter 2. Where chapter 2.1 will give an introduction to how flows may be transformed by the introduction of a resistance to the flow. This chapter will focus on screens used as velocity profile converters and includes an introduction to the relevant screen parameters and a presentation of the most relevant relations relating screen shape and parameters with up- and downstream flow conditions. Chapter 2.2 will present some

documented attempts on simulating flows through screens. These chapters, chapter 2.1 and 2.2, will be useful when trying to construct a numerical model modelling flows passing through curved screens.

Chapter 3, the methodology chapter, aims at giving a thorough description of the numerical model. Chapter 3.1 will provide a short description of what CFD is. This description is followed by chapter 3.1.1, 3.1.2, and, 3.1.3, describing the governing equations and two numerical methods that will be used in the model of the flow problem. Chapter 3.2 will then present the two numerical models relevant for this thesis, and chapter 3.3 describes the process of verification and validation, and why this is important when conducting a CFD-analysis. Chapter 3 concludes with chapter 3.4 that gives a description of the mesh used for both the models in addition to a discussion about mesh independence.

Chapter 4 presents and discusses the results from the CFD-simulations. The first two chapters, chapter 4.1 and 4.2, will go through the verification and validation process, which is an important step to conclude that the numerical model yields results that compare well with theoretical estimates and experimental data. After the numerical model has been verified and validated three chapters, chapter 4.3, 4.4, and 4.5, will investigate how the flow is affected by changing the screen shape, inlet velocity, and water depth. These chapters will then be followed by chapter 4.6, which discusses the relevant findings in this investigation.

The last chapter, chapter 5, aims at concluding this thesis and discusses how and to what extent the research objectives given in chapter 1.2 have been achieved.

Chapter 2

Theoretical Framework

This chapter aims at presenting the reader with relevant information about how velocity profiles may be transformed experimentally. A thorough description on how screens can modify the velocity profile in a channel will be given, where the linearized theory relating the screen shape with up- and downstream conditions will be used as a benchmark for the CFD-model later. A review of previous attempts using CFD for similar problems will be given as it provided useful information used to construct the CFD-model used in this thesis.

2.1 The generation of shear flows

Throughout history, several attempts have been made to obtain an analytical expression relating the upstream velocity profile, obstruction to the flow, and the resulting downstream velocity profile.

P. R. Owen and H. K. Zienkiewicz [23] produced an almost uniform shear using parallel rods with a non-uniform spacing back in 1957. The purpose of these rods is to introduce a resistance that results in a linear variation of total pressure far downstream of the rods. The resistance is caused by the rods, and the variation in resistance is obtained by the non-uniform spacing between them. Owen and Zienkiewicz [23] were able to derive an expression for the spacing between the rods that would transform a uniform upstream flow to a uniformly sheared downstream flow.

Although they were able to prove that their theory, which was later improved by J. H. McCarthy [22], was valid even for the generation of strongly sheared downstream flows, wire screens are usually preferred as velocity profile converters over parallel rods. Reasons for

this are:

- Parallel rods produce relatively high turbulence levels, about 3-4% compared to $\sim 0.5\%$ for screens [3].
- A small error in the spacing between the rods may have a great impact on the resulting velocity field [18].

This project will focus on screens as shear generators as this is used in the fluid mechanics lab at NTNU.

In 1958, J. W. Elder [7] published his work, in which he was able to relate upstream profile, downstream profile, screen shape, and screen parameters. Knowledge about any three of these four parameters allows the last one to be estimated by the linearized relation derived in his work. Most of the more recent publications regarding screens used for transforming the velocity profile are based on the analysis by Elder. A presentation of the general results from Elder's analysis will be given after having presented some key parameters used in his analysis.

2.1.1 Screen parameters

The screens analyzed in this thesis are assumed to be uniform, i.e. the spacing between the wires, the wire diameters, and the plane screen geometry, i.e. the knitting of the wires, is unchanged over the whole screen. An important parameter describing a screen is its solidity, which is the ratio between the projected blocked area and the total area in the plane of the screen. For a uniform square knitted screen with wire diameter d and axis-to-axis spacing between the wires denoted as l, the solidity may be expressed as in equation (2.1). Figure 2.1 illustrates the relevant lengths and knitting of the screen.

$$\sigma = \frac{\text{Projected blocked Area}}{\text{Total area}} = \frac{l^2 - (l-d)^2}{l^2} = \frac{2dl - d^2}{l^2}. \tag{2.1}$$

The screen solidity defined in equation (2.1) is the one used by W. Dunn and S. Tavoularis [6], while Elder [7] used the projected open area instead, i.e. the porosity $\phi = 1 - \sigma$, in his paper.

The Reynolds number is often specified with respect to the wire diameter d and is assumed to be constant over the screen. With a mean upstream velocity of U and a kinematic viscosity

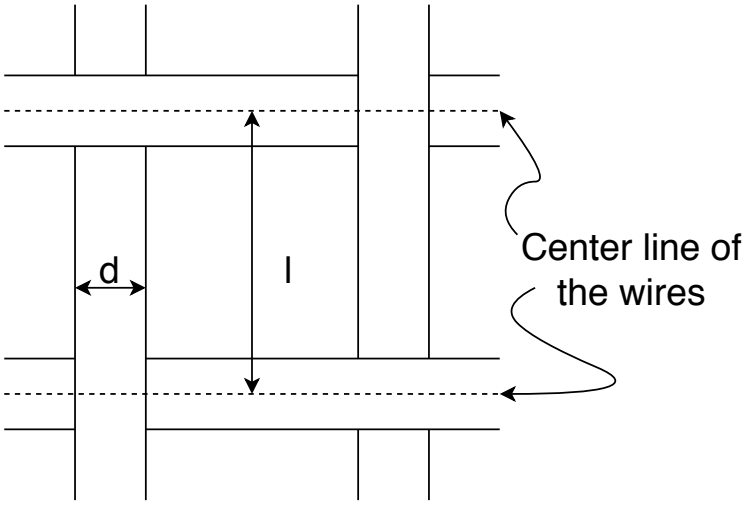

Figure 2.1: Illustration of a square knitted screen with the relevant screen lengths for calculating the solidity, which is defined in equation (2.1).

denoted by ν the Reynolds number is defined as,

$$Re_d = \frac{Ud}{\nu}. \tag{2.2}$$

Another important quantity is the pressure drop over the screen which is often expressed by the dimensionless pressure drop coefficient, defined as the ratio of the pressure drop over the screen and the dynamic pressure of the flow as in equation (2.3).

$$K = \frac{p_u - p_d}{\frac{1}{2}\rho U^2}. \tag{2.3}$$

Where p_u and p_d in equation (2.3) denote upstream and downstream pressure respectively. The pressure drop coefficient is also a measure of the dimensionless resistance caused by the screen to an incompressible flow when viscous effects are assumed to be negligible. The explanation for this is that the momentum flow normal to the screen will be constant for an incompressible flow. The continuity equation then reduces to $U_{nu} = U_{nd}$ where subscript nu and nd denote, respectively, the normal component up- and downstream of the screen.

The screen will experience a lift force, in addition to the drag force caused by the pressure drop and viscous resistance. This lift is caused by a change in the velocity component tangential to the screen, which is a result of the streamlines being deflected in the direction of the normal vector of the screen. It is therefore convenient to define a deflection coefficient as defined in equation (2.4). Where subscripts tu and td denote the tangential component

up- and downstream of the screen. An illustration of the streamline deflection and the change of the velocity components over a curved screen is given in figure 2.2.

$$B = \frac{U_{tu} - U_{td}}{U_{tu}}. \tag{2.4}$$

The definitions given in equation (2.1), (2.3), and (2.4) will be important inputs in the expression relating the screen shape with up- and downstream velocity profiles.

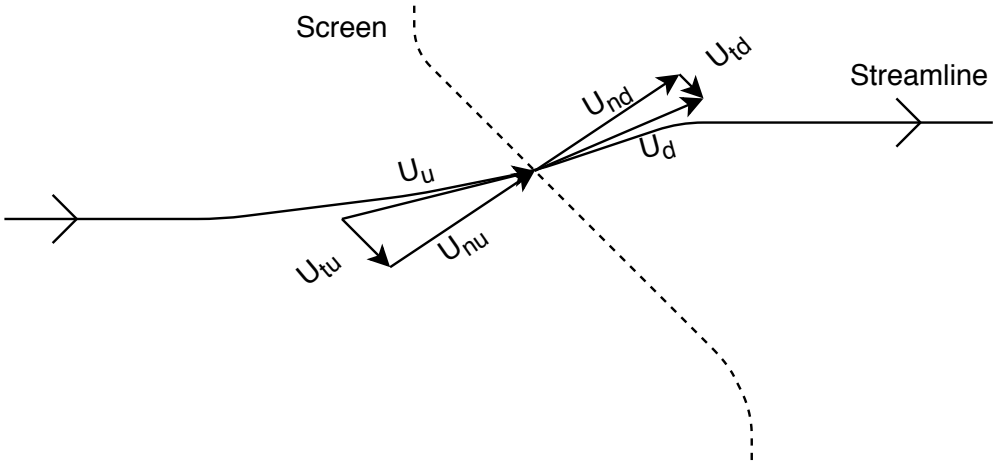

Figure 2.2: The change of the tangential velocity component and deflection of a streamline as a flow passes a curved screen.

2.1.2 Elder's analysis

The mathematical analysis performed by Elder is somewhat cumbersome, but in short, he assumed that the screen caused a small deflection of the streamlines such that the stream function could be written as $\psi + \psi'$. Where ψ represents the stream function without the deflection, i.e. for the present study, the stream function for uniform flow, and ψ' represents the small deflection introduced by the screen. An illustration of the flow problem and the coordinate axis used in the analysis is given in figure 2.3.

Elder used an empirical expression for the pressure drop coefficient, K, in his analysis. This expression was found experimentally by G. Davis [5] in 1957. Davis showed that the pressure drop coefficient for flows through screens could be expressed as,

$$K = K_0(\sigma) + K(\sigma, Re_d) = \left(\frac{0.05 + 0.95\sigma}{0.95(1-\sigma)}\right)^2 + \frac{88\sigma}{Re_d}, \tag{2.5}$$

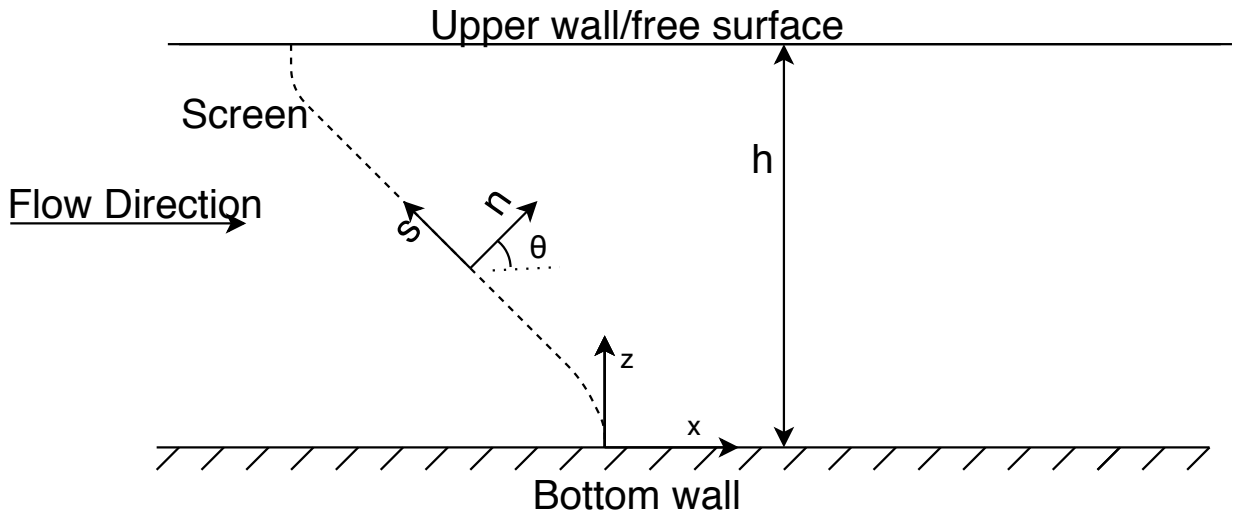

Figure 2.3: The figure is a 2D illustration of the flow problem. Observe that the screen starts at the origin at the bottom of the channel with the x-axis aligned with the flow direction, the z-axis in the normal direction to the flow, while the y-axis is directed into the paper plane. This definition of the coordinate system is used throughout this thesis.

where K_0 is the high Reynolds number limit of K.

In order to obtain an expression for the deflection coefficient, B, Elder assumed the flow to be similar to a uniform flow past a row of vortices. For a square wire screen, as illustrated in figure 2.1, Elder showed that B could be expressed as,

$$B = 1 - \frac{1}{\sqrt{1 + K^{\frac{1}{2}}}}. \tag{2.6}$$

It has been proved that the expression for B given in equation (2.6) over predicts its value [6]. However, as shown by Dunn and Tavoularis [6], more recent expressions for B yields even larger values than the expression in equation (2.6) for $K \geq 2$. The expression for B in equation (2.6) is therefore regarded as a sufficiently realistic approximation for flows through curved screens [6].

Elder linearized the governing equations to obtain an expression relating the empirically estimated screen parameters and screen shape with the up- and downstream flow conditions. This linearization means that all terms of second order or higher have been neglected from the analysis. Elder's derivation is somewhat cumbersome, so this section focuses on how to calculate the parameters and functions present in the final expression rather than the derivation itself. The full derivation can be found in [7].

In his final expression Elder makes use of an effective loss coefficient, γ, defined as,

$$\gamma = K\cos^2(\theta_s) \approx \gamma_0(1 + s(z)), \tag{2.7}$$

where the approximation is a result of the linearization of the expression. Where γ_0 is the average effective loss coefficient and $s(z)$ governs the deviation from this mean value. γ_0 is defined as,

$$\gamma_0 = \frac{1}{h}\int_0^h K\cos^2(\theta_s)dz, \tag{2.8}$$

where h is the channel height, or water depth for open channel flow, and θ the angle between the screen normal vector and the streamwise direction, as defined in figure 2.3. $s(z)$ will by the definition of γ_0 be restricted by

$$\int_0^h s(z)dz = 0.$$

Elder presented the following expression, which is a general result relating upstream- and downstream flow conditions with screen shape and screen parameters:

$$u_d - 1 = A(u_u - 1) - \frac{1}{2}(1 - A)s + E\mathcal{H}[Btan(\theta_s)], \tag{2.9}$$

where u_u and u_d are, respectively, the up- and downstream velocity profile normalized by the average velocity, i.e. for uniform upstream flow conditions $u_u = 1$ for all z. $E = \frac{\gamma_0}{2+\gamma_0-B}$, $A = 1 - \gamma_0(1 - E)$, and $\mathcal{H}$ is a transformation, quite similar to a Fourier transform, defined such that:

$$\begin{aligned} g^*(\pi\eta) = \mathcal{H}(g(\pi\eta)) &= \sum_{n=1}^{\infty}\alpha_n\cos(n\pi\eta), \\ g(\pi\eta) = \mathcal{H}^*(g*(\pi\eta)) &= \sum_{n=1}^{\infty}\alpha_n\sin(n\pi\eta), \end{aligned} \tag{2.10}$$

where $\eta = \frac{z}{h}$, such that both functions are defined for $0 \leq \pi\eta \leq \pi$ for any arbitrary function g. α_n are the Fourier coefficients corresponding to g. Equation (2.9) may be solved for the screen shape when both upstream and downstream conditions are known, i.e. for a known upstream flow and a desired downstream flow field, the equation then reads:

$$\frac{dx_s}{dz_s} = \tan(\theta) = \frac{1}{B}\sum_{n=1}^{\infty}\alpha_n sin(n\pi\eta), \tag{2.11}$$

where subscript s denotes that these coordinates describe the shape of the screen. The Fourier coefficients α_n are determined in the following way:

$$\begin{aligned} n = 1 : \alpha_1 &= \int_0^1 F(\eta) d\eta, \\ n > 1 : \alpha_n &= 2 \int_0^1 F(\eta) \cos(n\pi\eta) d\eta, \end{aligned} \tag{2.12}$$

with $F(\eta) = \frac{u_d - 1}{E} - \frac{A(u_u - 1)}{E} + \frac{1}{2E}(1 - A)s$. The first Fourier coefficient, i.e for $n = 1$, in equation (2.12) has to be zero for the solution to satisfy mass conservation.

Equation (2.9) may also be solved for the downstream velocity profile for a given upstream condition and screen shape and parameters. The solution then reads

$$\begin{aligned} B \tan(\theta) &= \sum_{n=1}^{\infty} \alpha_n \sin(n\pi\eta), \\ n = 1 : \alpha_1 &= \int_0^1 B \tan(\theta) d\eta, \\ n > 1 : \alpha_n &= 2 \int_0^1 B \tan(\theta) \sin(n\pi\eta) d\eta, \\ u_d = 1 + A(u_u - 1) - \frac{1}{2}(1 - A)s &+ E \sum_{n=1}^{\infty} \alpha_n \cos(n\pi\eta). \end{aligned} \tag{2.13}$$

Elder was able to solve equation (2.9) for the screen shape analytically under the assumption of a uniform upstream flow and a uniformly sheared downstream flow. To describe the downstream flow, he used the following definition of the shear parameter:

$$\lambda = 2 \frac{u_d - 1}{2\eta - 1}. \tag{2.14}$$

The integral solution of equation (2.9) then reads:

$$x_s(\eta) = \frac{\lambda h}{EB\pi^2} \int_0^a \left[\frac{2}{\pi} \int_0^{a + \frac{\pi}{2}} \log \left(\tan(\frac{1}{2}t) \right) dt \right] d\omega,$$

which Elder claimed had the following solution:

$$x_s(\eta) \approx \frac{\lambda h}{EB\pi^3} \left[-0.915a + \frac{1}{3}a^3 + \frac{1}{60}a^5 + \frac{1}{1680}a^7 \right], \tag{2.15}$$

where $\omega = \pi\eta$ and $a = \pi\eta - \frac{\pi}{2}$.

2.1.3 Comments and modifications to Elder's analysis

The way Elder evaluated the inner integral in equation (2.15) was unfortunately wrong, as pointed out by D. J. Maull [21] and Y. L. Lau and W. D. Baines [18]. I. P. Castro [3] calculated the integral and showed that the actual expression for the screen shape should have been the following:

$$\frac{x_s(\eta)EB\pi^3}{4\lambda h} = \left(\frac{\pi\eta}{2}\right)^2 \ln\left(\frac{\pi\eta}{2}\right) - \frac{3}{2}\left(\frac{\pi\eta}{2}\right)^2 + \frac{1}{18}\left(\frac{\pi\eta}{2}\right)^4 + \frac{7}{1350}\left(\frac{\pi\eta}{2}\right)^6 + \mathcal{O}((\pi\eta)^8), \quad (2.16)$$

The difference between this corrected solution and the erroneous results by Elder in equation (2.15) is considerable, something that can be seen in figure 2.4.

Another problem with equation (2.15) is that Elder assumed the screen loss coefficient to be constant for all η, i.e. he assumed $s(\eta) = 0$ and $\gamma_0 = K$. This error was pointed out by both Lau and Baines [18] and J. T. Turner [25]. Lau and Baines [18] developed a more general expression for any stratified fluid, i.e. not only a homogeneous fluid as Elder did. When comparing the resulting velocity profile using the screen shape resulting from their expression and the screen shape using Elder's analysis, they observed only small differences in the velocity profiles downstream of the screens [18].

Turner [25] pointed out that equation (2.9) should be solved iteratively for most cases, as both the resistance variation, $s(\eta)$, and the mean loss coefficient, γ_0, are unknown and their values should be updated for each iteration. He described an iterative procedure for solving equation (2.9), where $s(\eta) = 0$ and $\gamma_0 = K$ for the first iteration.

Castro [3] observed convergence problems with the iterative scheme given by Turner for $\frac{\lambda}{K} > 0.2$, when trying to calculate screen shapes that would produce uniformly sheared velocity profiles. Castro attempted to enhance stability by introducing a relaxation scheme, but this did not solve the convergence issue. He further states that Elder's analysis becomes increasingly invalid for increasing $\frac{\lambda}{K}$, which is intuitive as higher order terms become gradually more important with an increasing change of the velocity profile over the screen. Hence, violating the assumption that higher order terms are negligible.

Castro [3] did also include a discussion of the order of magnitude of the terms neglected in Elder's analysis. In which he argues that the resistance variation, governed by the $s(\eta)$-term, is in fact, a second-order term for small screen inclinations, which makes the solution including this term a "pseudo"-second order solution [3]. The s-term tends to reduce the screen inclination, but experimental results suggest that the screen is not sufficiently curved

for the desired shear when the s-term is included when calculating the screen shape [3]. J. L. Livesey and E. M. Laws [19] experienced that the desired downstream velocity profile was more accurately produced when the resistance variation, $s(\eta)$, was excluded when determining the screen shape.

Castro does also discuss the difficulty of determining an accurate value for the deflection coefficient, B, and that it might be reasonable to assume it to be variable over the screen. A variable B would make the formulation of even a linearized solution more difficult. He, therefore, suggests to use the linearized relation as an initial guess for the screen shape and then adjust the shape empirically, as Maull [21] did, to achieve a desired downstream velocity profile.

2.1.4 Dunn and Tavoularis' screen shape

The latest known attempt in relating the screen shape and parameters with a uniform upstream flow and a uniformly sheared downstream flow was performed by Dunn and Tavoularis in 2007 [6]. In developing their expression they made use of Elder's expressions for the pressure drop and deflection coefficient, defined in equation (2.5) and (2.6), respectively. Furthermore, they made use of a dimensionless shear parameter defined as,

$$\beta = \frac{h}{U_c}\frac{du(z)}{dz}, \tag{2.17}$$

where h is channel height, or water depth for an open channel flow, U_c is the center line velocity, and $u(z)$ the downstream velocity profile. Observe that this definition is equal to the one used by Elder, see equation (2.14), for a uniform upstream flow and a uniformly sheared downstream flow.

Dunn and Tavoularis made use of Maull's [21] solution which can be stated as,

$$x_s = \frac{(2 + K - B)\beta h}{KB} f\left(\frac{z_s}{h}\right), \tag{2.18}$$

where x_s and z_s are, respectively, the x and z coordinates of the screen. The function $f\left(\frac{z_s}{h}\right)$ are what differs between Maull's and Dunn and Tavoularis's solutions. Maull solved equation (2.9) for the problem for linear shear analytically using Fourier cosine series and modified the shape in order to get a uniform downstream shear experimentally. While Dunn and Tavoularis simplified Maull's expression as a fitted sixth order polynomial as given in

equation (2.19). The maximum difference between Maull's solution and the solution by Dunn and Tavoularis for the screen shape is 0.07% [6].

$$f\left(\frac{z_s}{h}\right) = -0.739\left(\frac{z_s}{h}\right)^6 + 2.812\left(\frac{z_s}{h}\right)^5 - 3.839\left(\frac{z_s}{h}\right)^4 + 2.687\left(\frac{z_s}{h}\right)^3 - 1.224\left(\frac{z_s}{h}\right)^2 - 0.0054\left(\frac{z_s}{h}\right). \tag{2.19}$$

An illustration of the normalized screen shape produced by equation (2.18) with (2.19) is shown in figure 2.4.

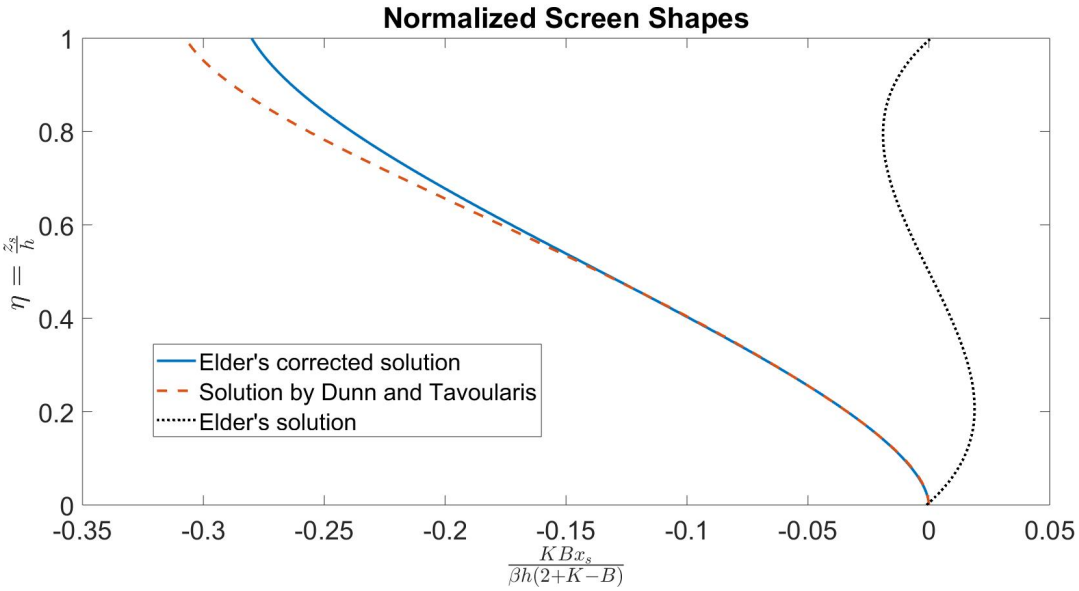

Figure 2.4: The plot illustrates the normalized screen shape, i.e. $\frac{KBx_s}{\beta h(2+K-B)} = f(\eta)$. Elder's solution, equation (2.15), and Elder's corrected solution, equation (2.16), were calcutated using $\gamma_0 = K$ and $s(\eta) = 0$.

Dunn and Tavoularis performed several experiments to validate that a screen whose shape is given by equation (2.18) using (2.19) would actually produce a uniformly sheared downstream velocity profile. The experiments were performed in an open channel flow of water with a depth of $h = 0.69$m. In their experiments, two screens were used, with a solidity of $\sigma = 0.46$ and $\sigma = 0.59$, a shear parameter, β, ranging from $0.16 - 0.43$, and a pressure loss coefficient, K, ranging from $1.5 - 9$. The maximum β/K ratio tested in their experiments was 0.22, which is relatively low and one may say that the assumptions for the linearized theory of Elder are not seriously violated for the given flow conditions [3, 6]. The resulting

downstream velocity profiles, measured at a distance 0.4m downstream of the screen and at several spanwise locations, were in relatively good agreement with theory [6]. The results may be found in figure 10 in the paper by Dunn and Tavoularis [6].

2.2 Previous simulations of flow through screens

This section will present some previous attempts at simulating flows through screens. Results from these attempts will be useful for constructing a CFD-model for flows through curved screens.

2.2.1 S.I. Green et al.

In 2007 S. I. Green et al. [13] performed simulations of flows through straight woven screens using ANSYS Fluent [13]. Due to limited computational time, the simulations were performed on a geometry consisting of only 6 wires, 2 vertical and 4 horizontal, see figure 2.5. An illustration of the computational domain can be found in figure 2.6. They performed a few simulations on more extended wire geometries and longer inlet and outlet domains in which the results differed with less than 1% compared to simulations using the domain depicted in figure 2.6[13].

The hybrid mesh used in the simulations performed by Green et al. is illustrated in figure 2.7. Observe how the small cells are contained to the screen region only, while larger structured cells are used in the inlet and outlet regions. Velocity inlet and pressure outlet boundary conditions were used, while periodic boundary conditions were used at the side walls.

When performing a mesh independence test, they observed that approximately 1.6 million mesh volumes were needed in the screen domain to produce a solution that was within 1% of the asymptotic value of the pressure drop over the screen [13]. The simulations showed similar behaviour for several screens and screen Reynolds numbers. This shows that simulations of flows through screens are very computationally intensive. Vortex shedding over the wires in a screen, like vortex shedding over a cylinder in a cross flow, is likely to happen when the Reynolds number exceeds a specific value. Therefore, a comparison between steady and unsteady simulations was investigated by Green et al. The comparison showed that the results differed by less than 1.5% even though vortex shedding over the wires was expected

to occur [13]. This indicates that the unsteadiness of the flow has little effect on the solution, and it is, therefore, reasonable to use steady-state solvers to reduce computational time.

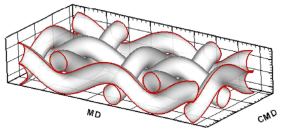

Figure 2.5: This illustration, taken from [13], shows the wire geometry used by Green et al. in their simulations. MD and CMD are, respectively, machine direction and counter machine direction and are used to describe the orientation of the wires in woven screens.

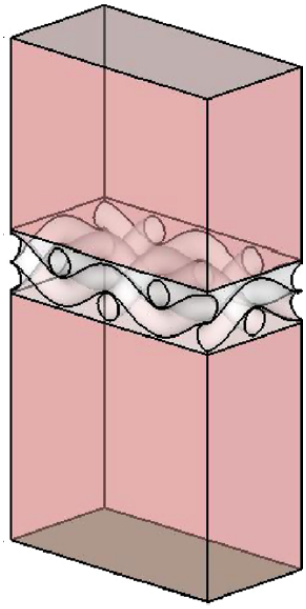

Figure 2.6: The illustration is taken from [13] and shows the computational domain used by Green et al.

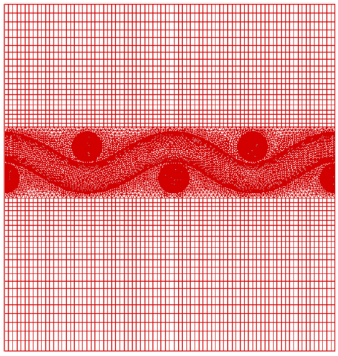

Figure 2.7: The illustration is taken from [13] and shows the mesh used in the simulations performed by Green et al. Observe how the hybrid mesh ensures that the fine cells are contained to the screen region only.

2.2.2 M. Teitel

M. Teitel [24] performed several simulations of flows through woven screens in 2009 to investigate the pressure drop over the screens. Teitel performed simulations on two distinct models for flows through screens in a squared channel. The first model was an accurate representation of the screen, resolving the whole flow field upstream, within, and downstream

of the screen, something which is very computationally intensive, see chapter 2.2.1. In the second model, he substituted the screen with a porous zone. The flow resistance in this porous zone was then modelled using the porous media model (PMM) in ANSYS Fluent. The results from this model were then compared with experimental data and results using the model where the flow field within the screen was fully resolved. The porous media model will be explained in chapter 3.1.2.

As a benchmark for both simulations Teitel made use of empirical relations and experimental data for the pressure drop over woven screens. The empirical relations used for evaluating the pressure drop of uniform flows were those of B. J. Bailey et al. [1] and E. Brundrett [2] given in equation (2.20) and (2.21) respectively. ϕ and θ, in equation (2.20) and (2.21), are, respectively, the porosity of the screen and the approach angle of the incoming flow, i.e. angle between screen normal vector and the streamwise direction. Ten is the base number for the logarithmic functions in both equation (2.20) and (2.21). The porosity, ϕ, is given as the projected open area of the screen in these equations, i.e. $\phi = 1 - \sigma$ where σ is the screen solidity defined in equation (2.1). The first term in equation (2.21), i.e. $\frac{7.125}{Re\cos(\theta)}$, is usually multiplied by the ratio of the momentum flux and the flux of kinetic energy. This ratio is assumed to be 1, corresponding to uniform flow, for all cases investigated in this thesis.

$$K = \frac{1-\phi^2}{\phi^2}\left[\frac{18}{Re} + \frac{0.75}{\log_{10}(Re+1.25)} + 0.055\log_{10}(Re)\right]. \tag{2.20}$$

$$\frac{K_\theta}{\cos^2(\theta)} = \frac{1-\phi^2}{\phi^2}\left[\frac{7.125}{Re\cos(\theta)} + \frac{0.88}{\log_{10}(Re\cos(\theta)+1.25)} + 0.055\log_{10}(Re\cos(\theta))\right]. \tag{2.21}$$

The pressure drops from the CFD-simulations resolving the whole flow field around screens were in excellent agreement with the experimentally measured pressure drop. Both the experimental data and CFD-results showed that the pressure drop relation given in equation (2.21) performs better than equation (2.20) for the low and moderate porosity screens at the given Reynolds numbers, $0 \leq Re_d \leq 60$, at an approach angle of zero. This is illustrated in figure 2.8, which is figure 2a in Teitel's paper [24], where it may be observed that both the experimental data and CFD-results lies closer to stippled line given by equation (2.21) than the solid line given by equation (2.20).

As resolving the whole flow field within the screen is time-consuming, Teitel suggested using the PMM when the flow structures within and in the near vicinity of the screen are not of interest. The screen is then substituted by a porous zone where the PMM approximates the pressure drop using the Darcy-Forchheimer law of porous media, which can be expressed

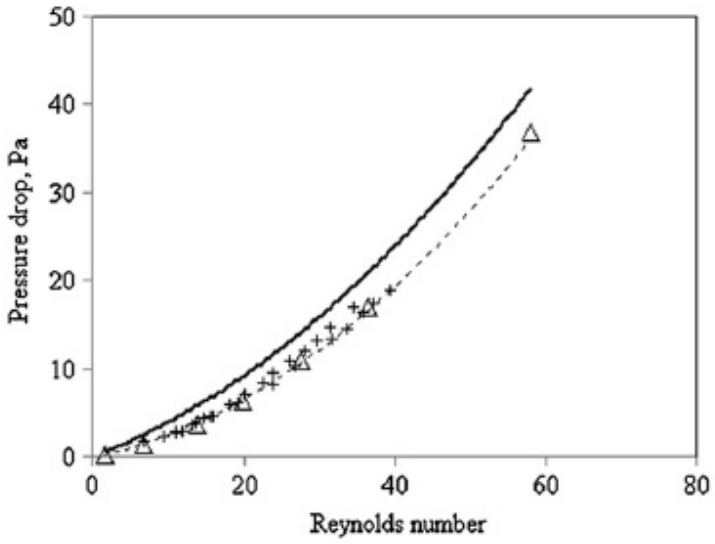

Figure 2.8: Comparison of experimental results (+), CFD-simulations (Δ), and the solid and stippled line are the predicted pressure drop using equation (2.20) and (2.21) for a screen with a porosity of 0.36. The illustration is figure 2a in [24].

as:

$$\frac{\partial p_i}{\partial x_i} = \sum_{j=1}^{j=3} \left[D_{i,j}\mu u_j + C_{i,j}\frac{1}{2}\rho|u|u_j \right], \tag{2.22}$$

where $D_{i,j}$ and $C_{i,j}$ are, respectively, the jth component of the viscous and inertial loss factors in the ith direction. In order to specify the viscous and inertial loss factors in equation (2.22), Teitel assumed the screen to be a homogeneous porous medium such that the flow resistance is equal for all velocity components in all directions, i.e. $D_{i,j} = D$ and $C_{i,j} = C$. To determine D and C Teitel made use of a curve-fit tool to represent the pressure drop over a screen for a given set of velocities on the following form:

$$\Delta p = Au + Bu^2, \tag{2.23}$$

where u is the velocity upstream of the screen and A and B are coefficients defined by the curve-fit tool. A and B are then related to C and D by the following:

$$\begin{aligned} C &= \frac{A}{\mu \Delta x}, \\ D &= \frac{2B}{\rho \Delta x}, \end{aligned} \tag{2.24}$$

where Δx is the thickness of the porous region modelling the screen.

Teitel showed that this model, where the screen is modelled by the PMM, predicts the pressure drop for flows through screens accurately. The pressure drop predicted by using this model was almost the same as the pressure drop predicted using the model where the whole flow field was resolved within the screen. From figure 3 in Teitel's paper [24] it can be seen that it is only at the higher Reynolds number for the high porosity screen that the PMM tends to underestimate the pressure drop over the screen.

Chapter 3

Methodology

This chapter aims to thoroughly describe the CFD-model that will be used to generate the results in this thesis. This includes a presentation of the relevant methods and models, how to solve the linearized solution by Elder to determine theoretical estimates, and a thorough description of how the screen has been modelled using the PMM. A presentation of the mesh used for the CFD-model, in addition to a mesh independence study, will be given at the end of this chapter.

3.1 Computational Fluid Dynamics

The commercial CFD software ANSYS Fluent 19.2 was used for the numerical simulations in this thesis. ANSYS Fluent is a finite volume based CFD solver which solves a discretized set of governing equations for a given flow problem on a mesh. This mesh consists of a finite number of fluid volumes in which all these volumes combined represents the domain of interest for the given problem, where boundary conditions are specified at all the boundaries of the given domain. The governing equations are then solved for each of these volumes.

3.1.1 The Governing Equations

The flow problem to be analyzed in the present thesis, i.e. fluid flows through curved screens, is assumed to be incompressible. For the case of incompressible flow the Navier-Stokes equations consists of the incompressible continuity and momentum equations, which

are given in equation (3.1) and (3.2) respectively.

$$\nabla \cdot \mathbf{u} = 0. \tag{3.1}$$

$$\frac{\partial \mathbf{u}}{\partial t} + (\mathbf{u} \cdot \nabla)\mathbf{u} = -\frac{1}{\rho}\nabla p + \nu \nabla^2 \mathbf{u} + \mathbf{g}. \tag{3.2}$$

In equation (3.1) and (3.2) $\mathbf{u}$ represents the velocity vector, ρ density, p pressure, ν the kinematic viscosity, and $\mathbf{g}$ the gravitational acceleration vector. These equations are discretized using the finite volume method and solved on a computational mesh using ANSYS Fluent 19.2.

Quality Measures of the Computational Mesh

Care must be taken when generating a computational mesh, as the quality of the cell volumes in the mesh may influence the final solution of a flow problem using that mesh. Two quality measures that can be used to determine whether the generated mesh should be used or not are the skewness and the orthogonal quality of the cells. The skewness is a comparison of the actual cell and the ideal cell. Meshes that includes cells whose skewness is above 0.95 should be avoided, and the average value should be well below this. The reason for this is that highly skewed cells are associated with less accurate solutions [8]. An illustration of ideal and skewed cells are given in figure 3.1. Orthogonal quality is defined as "the minimum of the cosines of the angle between the face normal vector and the corresponding vector from the centroid of the cell to the centroid of that cell face" (ANSYS Fluent Meshing Users Guide (2017)) [8]. The closer to one the orthogonal quality is the better, and attention should be given to cells with low orthogonal qualities.

A mesh independence test should also be conducted to ensure that the solution obtained by a CFD-simulation is independent of the mesh. Such an analysis can be performed by investigating how the solution changes when refining the mesh. The mesh should be refined until further refinement does not change the solution.

3.1.2 Porous Media Model

An initial concern was the huge difference in the length scales that are important to the problem. Small-scale flow structures will be generated within and in the wake of the screen, as screens usually consist of very thin wires with a small spacing between them. These small-scale flow structures may be important to resolve to obtain the correct pressure drop

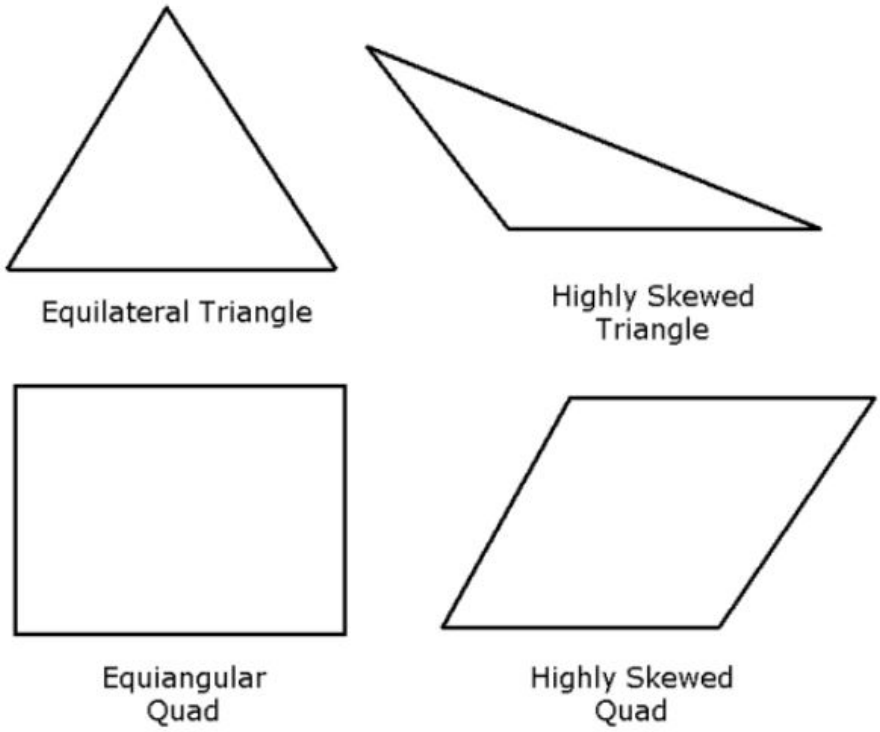

Figure 3.1: The illustration is taken from the ANSYS Fluent Meshing User's Guide [8], and illustrates the concept of skewness.

over the screen. Getting this pressure drop correct will be important, as this is one of the effects that cause the change in velocity profile over the screen. The channel height, or water depth, for the cases investigated in this thesis, will be in the order of 0.1m, and the combined streamwise extent needed to resolve the flow problem accurately is assumed to be in the order of a couple of water depths. A problem regarding the number of cells needed in a numerical model may occur as the length scales of the channel are much larger than the length scales of the flow structures produced by the screen.

A large number of cells would, therefore, be required to get the correct pressure drop over a screen. Assuming that the number of cells required in the simulations by Green et al. [13] is an accurate estimate for the cells required to resolve the flow through curved screens, 1.6 million cells are needed to resolve the flow over four horizontal wires. Such that a channel of a depth $h \sim 0.1$m and a screen with diameter and wire spacing of $d = 0.25mm$ and $l = 0.75mm$ respectively, would require at least $N = \frac{h}{4l} 1.6 \cdot 10^6 = 53.33$ million cells. This will be the minimum number of cells required to get within 1% of the asymptotic value of the pressure

drop over a straight screen. The number of cells required for a curved screen used to transform the velocity profile as described in chapter 2.1, would be even larger as the fluid volume in the region around the screen increases. Performing the numerical calculations for a domain with so many cells will be time-consuming, ineffective and would require access to HPC-resources (high-performance computing resources) for most applications due to both memory issues and computational time. The fact that transient analysis will most likely be necessary for multiphase flow simulations strengthens the argument that model simplifications are needed to study the behaviour of flows through curved screens.

Furthermore, as stated in the research objectives, see chapter 1.2, it is desired that the CFD-model should be an efficient tool that estimates the downstream velocity profile for a given screen shape within a reasonable amount of time. This objective cannot be fulfilled simultaneously as resolving all the length scales of the physical screen.

Teitel [24] showed that the PMM in ANSYS Fluent accurately predicted the pressure drop associated with flows through straight screens, see chapter 2.2.2. Therefore, it is reason to believe that this may be an adequate simplification for curved screens as well. The ANSYS Fluent Theory guide [9] gives a thorough description of the PMM. The PMM introduces a momentum loss to the flow inside regions which are specified as porous. The porous regions must be specified by the user. The porous region modelling a screen will take on the same shape as the physical screen it is modelling in this thesis. The momentum loss introduced in the porous regions is given in equation (3.3), which may be interpreted as a pressure gradient or a resistance to the flow in the respective direction. The momentum loss introduced in the porous region will model how physical flows are affected by screens. The PMM fails to predict the velocity field in the near vicinity of the screen, as the velocity increase that occurs in the pores of the screen is neglected when the screen is replaced by the artificial momentum loss given in equation (3.3). Far downstream of the screen, it is assumed that this limitation will have a negligible effect on the velocity profile.

$$S_i = -\left[\sum_j \left(D_{i,j}\mu u_j + C_{i,j}\frac{1}{2}\rho|u|u_j\right)\right]. \tag{3.3}$$

The terms $D_{i,j}$ and $C_{i,j}$ in equation (3.3) are, respectively, the viscous and inertial loss factors, and they need to be specified by the user for each case. These loss factors can be approximated using experimental data or empirical relations.

Brundrett's [2] expression for the pressure loss given in equation (2.21) will be used to

determine $D_{i,j}$ and $C_{i,j}$ in this thesis. Teitel [24] showed that equation (2.21) was in good agreement with CFD and experimental results. Hence, using this expression opens for the possibility to run simulations on screens where experimental data for the pressure loss is not available. The resistance in the porous medium is assumed to be homogeneous, i.e. D and C are constant in all directions and for all velocity components. The loss factors can then be determined by fitting the second order polynomial given in equation (2.23) to the pressure drop predicted by equation (2.21) assuming an approach angle of zero, using a closed set of velocities relevant for the specific case. The loss factors are then approximated using the coefficients obtained by the curve-fit using equation (2.24). This is similar to the procedure used by Teitel [24] and it was also suggested in ANSYS Fluent Theory Guide [9].

The resistance in the porous region, modelling the screen, is assumed to be homogeneous, i.e. D and C are constant for all velocity components in the normal and tangential direction of the screen. As the extent of the porous region is usually several orders of magnitude larger in the tangential direction compared to the normal direction of the screen, the total resistance in the tangential direction becomes much larger. As the flow seeks the path of minimum resistance, it will be deflected in the direction of the normal vector of the porous region, which is the case for a physical screen as well. A user-defined function (UDF) will, therefore, be needed to determine the normal vector of the porous region at every location. This normal vector will then be used to specify the loss factors in the direction normal to the porous region, such that the path of the least resistance will always be in the same direction as the normal vector. This will also ensure that the total loss over the screen in this direction will correspond to the loss predicted by equation (2.21).

Most screen shapes are not given by an analytical function. These screen shapes and normal vectors are then estimated using the curve-fit toolbox in MATLAB. Curve-fits using polynomials up to ninth order can be generated to represent a specific screen shape as accurately as possible. The angle between the normal vector of the screen and the x-axis can be determined using equation (3.4), as soon as an adequate curve-fit, expressing the screen shape as $x_s(z_s)$, has been defined. As the screen shape and the corresponding screen normal vector is different for most cases, a new and updated UDF is needed for each case where the screen shape is changed.

$$\theta_n = \tan^{-1}\left(-\frac{dx_s}{dz_s}\right) \tag{3.4}$$

The Modelling of Honeycomb

A honeycomb, which may be seen up- and downstream of the screen in figure 1.1, functions as a flow straightener which is used to deteriorate the velocity components normal to the flow direction. For the purposes of this thesis, it is assumed that a honeycomb may be accurately modelled by the PMM. The reason for this is that it resembles a screen with an elongated streamwise extent that is placed normal to the flow.

The pressure drop over the honeycomb will be determined using the same equation as used for the screen, see equation (2.21), only adjusted for porosity. The reason for this choice is that no relation for pressure drop over honeycombs was found in literature. The porosity of the honeycomb is given by the ratio of the projected open area to the total area as perceived by the flow. For a honeycomb consisting of hexagonal elements the porosity is given as the following:

$$\phi = \frac{dw + 2w^2 \sin(\beta)\cos(\beta)}{dw + 2w^2 \sin(\beta)\cos(\beta) + 6\frac{t}{2}w + \frac{\sqrt{3}}{2}t^2}. \tag{3.5}$$

The cell dimensions used in equation (3.5) are defined in figure 3.2. The blocked area of each cell is approximated as $6\frac{t}{2}w + \frac{\sqrt{3}}{2}t^2$.

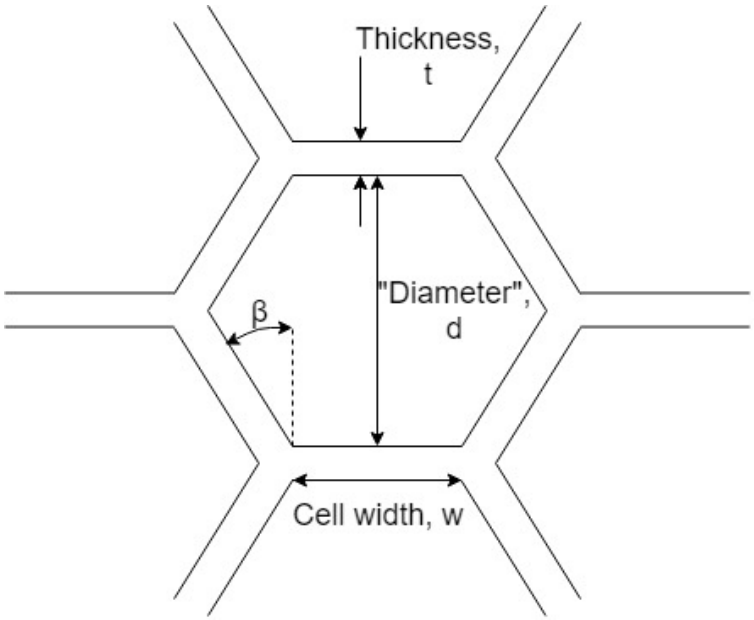

Figure 3.2: Illustration of a the relevant dimensions of a hexagonal cell in a honeycomb.

The viscous and inertial loss factor, the $C_{i,j}$ and $D_{i,j}$ in equation (3.3), will be determined using the same procedure as for the screen. The pressure drop will be calculated using equation (2.21) for a set of relevant velocities. This pressure drop will then be approximated using a second-order polynomial curve-fit determined using the curve-fit toolbox in MATLAB. The coefficients resulting from this curve-fit will then be used to determine the loss factors using equation (2.24).

3.1.3 Volume of Fluid

Volume of Fluid (VOF) is a method for solving problems where two or more immiscible fluids are present using only a single set of the momentum equations. A thorough description of the VOF-model used in ANSYS Fluent may be found in the ANSYS Fluent Theory Guide [10]. For this thesis, flows in both closed and open channels are of interest, in which a multiphase solver is needed for the latter.

The VOF-model uses a modified set of the Navier-Stokes equations that track the volume fraction of each of the phases in every cell of the computational domain. As the VOF-model only computes the volume fraction of the phases in each cell, an interface reconstruction will be needed unless the interface is located precisely at the cell boundaries.

For the open channel cases, air and water are assumed to be incompressible with no mass transfer mechanism between them, i.e. the effect of evaporation is considered negligible and will not be considered. The continuity equation can then be expressed as

$$\frac{\partial Y_q}{\partial t} + \nabla \cdot (Y_q \mathbf{u}_q) = 0, \tag{3.6}$$

where Y_q and $\mathbf{u}_q$ is, respectively, the volume fraction and velocity vector of phase q. The volume fraction of the primary phase, defined as air for the cases in this thesis, is not obtained from equation (3.6), but from the following constraint:

$$\sum_{q=1}^{n} Y_q = 1. \tag{3.7}$$

This constraint in equation (3.7), ensures that the sum of the volume fractions in a cell never exceeds one to ensure that total mass is conserved. Only a single set of the momentum equations are solved when using the VOF-model, as all phases are assumed to share the same velocity field. This assumption will not hold for cases where large velocity gradients are present at the interface between two phases [10]. The velocity in the cases studied in

this thesis will be fairly low, i.e. in the order of $0.1\frac{\mathrm{m}}{\mathrm{s}}$, such that large velocity gradients at the air-water interface are not likely to occur. The momentum equations in the VOF-model are given as

$$\frac{\partial \mathbf{u}}{\partial t} + \nabla \cdot (\mathbf{u}\mathbf{u}) = -\nabla p + \nabla \cdot [\mu(\nabla \mathbf{u} + \nabla^T \mathbf{u})] + \rho \mathbf{g} + \mathbf{F}, \tag{3.8}$$

where the bold $\mathbf{u}$, $\mathbf{g}$, and $\mathbf{F}$ are, respectively, the velocity vector, the vector of the gravitational acceleration, and the vector containing the effect of surface tension. The T in ∇^T denotes the transpose, and the fluid properties in equation (3.8) are approximated using the volumetric average of the cell, i.e.

$$\begin{aligned} \rho &= \sum_q Y_q \rho_q, \\ \mu &= \sum_q Y_q \mu_q. \end{aligned} \tag{3.9}$$

The Weber number, which is defined as the ratio of inertial and surface tension forces, can be used to estimate whether surface tension effects can be neglected or not for cases of $Re = \frac{\rho U L}{\mu} >> 1$. It is defined as $We = \frac{\rho L U^2}{\varsigma}$, where ρ, L, and ς denotes, respectively, the density, characteristic length, and surface tension. For flows of water with an air-water interface, i.e. $\rho = 998.2\frac{\mathrm{kg}}{\mathrm{m}^3}$, $\mu = 0.001003\frac{\mathrm{kg}}{\mathrm{ms}}$, and $\varsigma = 0.072\frac{\mathrm{N}}{\mathrm{m}}$, the Reynolds number will usually be in the region of $10^3 - 10^4$ for velocity, U, and channel height, h, in the order of $0.1\frac{\mathrm{m}}{\mathrm{s}}$ and 0.1m, respectively. This results in a Weber number in the order of $We = \mathcal{O}\left(10^2\right)$, and it could be argued that $We >> 1$ such that the effect of surface tension can be neglected. Surface tension effects will be neglected for most of the simulations performed in this thesis. A comparison of the velocity profile resulting from a case neglecting surface tension effects and one that includes these effects will be given in chapter 4.6.4.

The VOF-model in ANSYS Fluent offers two options for modelling the effects of surface tension. In which one of them is the continuum surface stress (CSS) model, which will be used for the case including surface tension effects in the thesis. The stress tensor used to model the surface tension effects in the CSS model is defined as

$$T = \varsigma \left(|\nabla Y| \mathbf{I} - \frac{\nabla Y \otimes \nabla Y}{|\nabla Y|} \right), \tag{3.10}$$

where $\mathbf{I}$ is the identity matrix, and $\otimes$ is the outer product of two vectors. The surface tension force, given in equation (3.11), is expressed in a conservative form in the CSS model.

$$\mathbf{F} = \nabla \cdot T = \nabla \cdot \varsigma \left(|\nabla Y| \mathbf{I} - \frac{\nabla Y \otimes \nabla Y}{|\nabla Y|} \right). \tag{3.11}$$

The VOF-model also has an Open Channel Flow option, in which the user may specify the free-surface level for the outlet regions. The pressure at the outlet is then determined by the adjacent cell, such that the pressure gradient normal to the outlet boundary is zero. This option was used in the simulations in this thesis, as the flow through a screen resembles an open channel flow, with zero pressure gradient in the streamwise direction at the outlet. The pressure at the outlet can also be specified by the user, but this option was not used in this thesis as the pressure at the outlet is unknown before conducting the simulations.

3.2 Numerical Model

This chapter aims at describing the CFD-model, including model approximations, boundary conditions, and how the screen shape was determined. A lot of time was spent on developing a model resolving the whole flow field within the screen at the beginning of the thesis work. However, for reasons given at the beginning of chapter 3.1.2, it was apparent that it would be time-consuming to get a solution as it would become very computationally intensive. The PMM explained in chapter 3.1.2, has proved to be an effective solution for screens normal to the flow direction, see [24]. The PMM effectively reduces the computational time, as the effect of the screen is modelled by adding the momentum sink given in equation (3.3).

3.2.1 Screen shape

As stated by Turner [25], equation (2.9) needs to be solved iteratively for most cases as no general analytical solution exists. This section aims at describing the iterative scheme used to solve this equation for the screen shape given screen parameters, upstream velocity profile, and the desired downstream velocity profile. The MATLAB script using this iterative solution method for calculating the screen shape is given in appendix A.1. A scheme predicting the downstream velocity profile given screen shape, screen parameters, and upstream velocity profile was also constructed. The MATLAB function for this is given in appendix A.2.

Iterative Solution for the Screen Shape

Equation (2.9) is a general solution of the linearized problem for flows through screens when the effect of viscosity is neglected everywhere except in the near vicinity of the screens. It

may, therefore, be used to determine the screen shape for arbitrary up- and downstream velocity profiles, given that the approximations are satisfied, e.g. small flow deflections such that the negligence of the higher order terms can be justified.

In this thesis, equation (2.9) has been solved iteratively with MATLAB using numerical integration to determine the Fourier coefficients defined in equation (2.12). The iterative procedure used to determine the screen shape for the desired downstream velocity profile reads:

1. Calculate K and B given the mean inlet velocity and screen parameters and define two tolerances. One for the two-norm of the difference of the k'th and $(k-1)$'th iteration and one for the ratio of this and the two norm of the difference between the first iteration and the initially straight screen shape. The two-norm of the difference of the k'th and $(k-1)$'th iteration is defined in equation (3.12). These tolerances will be used as convergence criteria for the iterative procedure.

2. Set $\gamma_0 = K$ as an approximation for the first iteration. Define the vector z_s, which contains the positions in the vertical direction that the x-position of the screen, x_s, will be determined for.

3. Calculate $E = \frac{\gamma_0}{2+\gamma_0-B}$ and $A = 1-\gamma_0(1-E)$, and define $F(\eta) = \frac{u_d-1}{E} - \frac{A(u_u-1)}{E}$.

4. Calculate the Fourier coefficients, defined in equation (2.12), using numerical integration.

5. Perform the summation given in equation (2.11) to determine the screen slope.

6. Calculate the discrete screen positions in the following way: $x_{s_{i+1}} = x_{s_i} + \frac{1}{2}[\tan(\theta_{s_{i+1}}) + \tan(\theta_{s_i})](z_{s_{i+1}} - z_{s_i})$.

7. Given the new screen shape calculate γ_0 using equation (2.8).

8. Calculate the two-norm of the difference between the new screen shape and the screen shape of the previous iteration.

9. If the two-norm of the difference for iteration k and $k-1$ and the ratio of this difference and the two-norm of the difference for first iteration and initial screen shape are less than the tolerances defined in step 1, the iterative procedure has converged and the

calculated screen shape satisfies equation (2.9). If one, or more, of the convergence criteria are not met, return to step 3.

$$\epsilon^k = \left[\Delta z_s \sum_i \left(x_{s_i}^k - x_{s_i}^{k-1} \right)^2 \right]^{\frac{1}{2}} \tag{3.12}$$

The resistance variation, $s(\eta)$, is not included in the iterative procedure because Livesey and Laws [19] observed that the results were better when this term was omitted. From results to be presented later, it is clear that the solution for the screen shape where the resistance variation is neglected performs better at producing the desired velocity profile. The MATLAB script used to determine the screen shape for some of the cases in this thesis is given in appendix A.1. The solution algorithms described by Turner [25] and Castro [3] were used as inspiration for the solution algorithm presented in this section. The presented solution algorithm does only provide reasonable results for moderate changes of the velocity profile over the screen, such that the negligence of higher order terms can be justified.

3.2.2 Set-up of the numerical model

Two distinctive set-ups will be investigated in this thesis, namely, flows through screens in closed and open channels. The screen will be replaced by a porous region in both set-ups, where the viscous and inertial loss factors are approximated using the procedure described in chapter 3.1.2.

The Porous Screen Region

The screen shape will vary from case to case, but common for all is that the screen shape will be specified in a text-file. This text-file contains discrete points on the screen and consists of five columns. The first column specifies the part number, this will always be one in this thesis as only one part will be specified by this text-file. The second column describes the sequence in which the points are connected, i.e. one is connected to two, which is further connected to three, and so on. The last three columns specify the x, y, z- coordinates, respectively. An example of such a text-file is given in figure 3.3. This text-file is imported into ANSYS DesignModeller, by using the 3D curve tool, to create a line that has the same shape as the screen defined by the discrete coordinates given in the text-file.

Part Number	Sequence	x-coordinate	y-coordinate	z-coordinate
1	1	0	0	0
1	2	-0.003036125	0	0.000858586
1	3	-0.005900977	0	0.001717172
1	4	-0.008607098	0	0.002575758
1	5	-0.011166364	0	0.003434343
1	6	-0.013590009	0	0.004292929
1	7	-0.015888647	0	0.005151515

Figure 3.3: Illustration of the set-up of the text-file that can be imported to ANSYS Design-Modeller to produce a line specified by the coordinates in this file.

This line specifying the screen shape is then imported into ANSYS Spaceclaim. A new line is then extruded along the path that represents the screen shape, creating a region with a thickness equal to one wire diameter of the screen to be modelled. This region will later be specified as porous and will model the screen.

The viscous and inertial loss factors that model the flow resistance that a screen introduces to the flow are determined using the procedure described in chapter 3.1.2. UDF's will then be needed such that the flow resistance can be defined in the normal and tangential direction of the porous region. Two UDF's are required to determine the x- and z-component of the normal vector, with respect to the x-axis, of the screen in every single point. These UDF's are then compiled into ANSYS Fluent and used to define the flow resistance in the normal and tangential direction of the screen. The flow resistance factors, determined by the procedure described in chapter 3.1.2, is then defined in both the direction normal and tangential to the screen. Such that the resistance normal to the screen will always be the same as predicted by equation (2.21). The total resistance will then be much larger in the tangential direction than the normal direction of the screen, as the thickness of the screen perceived by the flow will be much larger in the tangential direction. The reason for this is that the flow resistance is defined as a momentum loss per unit length in the PMM. An illustration of a UDF calculating the x-component of the screen normal vector can be found in figure 3.5. This UDF corresponds to the curve fit of the iteratively calculated screen shape, obtained using the procedure described in chapter 3.2.1, which is illustrated in figure 3.4. A sixth-order polynomial was used to for the curve-fit for this screen.

Two different screens will be modelled in this thesis, and the parameters of these screens are given in table 3.1

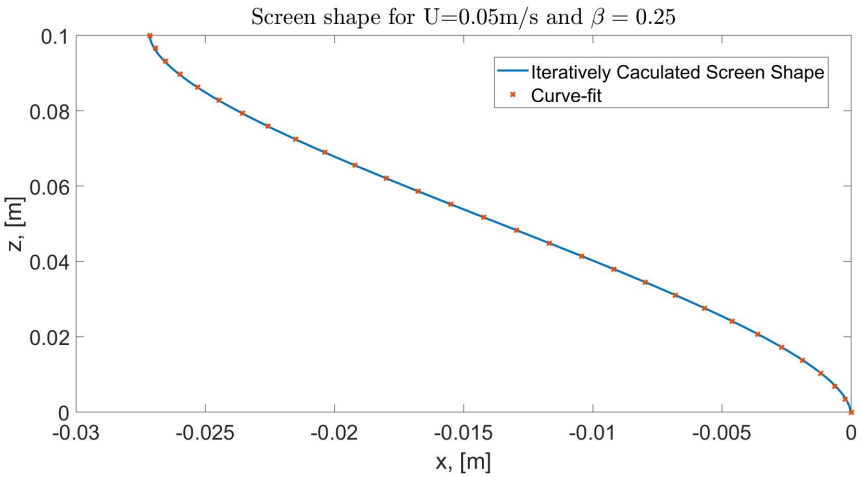

Figure 3.4: A plot of the iteratively calculated screen shape, and the corresponding curve-fit, for a uniform inlet flow and a uniformly sheared downstream flow.

Table 3.1: Screen parameters for the screens relevant in this thesis.

	Screen 1	Screen 2
Wire Diameter, d	0.45mm	0.25mm
Axis-to-axis spacing, l	1.59 mm	0.75mm
Solidity, σ,	0.4859	0.5666
Porosity, ϕ	0.5141	0.4444

Model 1: Closed Channel Flow

The closed channel model is an efficient way of testing the performance of a specific screen shape, as it only contains one phase. The set-up for these cases is relatively simple, and a steady-state solution of the flow is obtained fast, using the steady-state solver in ANSYS Fluent 19.2. The effect of gravity was also included in the model and was set to $\mathbf{g} = -9.81\vec{e_z}$. The boundary conditions used for these cases are:

- Inlet: The velocity is specified at the inlet, and the velocity profile will be uniform at the inlet for all cases investigated in this thesis.
- Outlet: At the outlet, the outflow boundary condition is used, as neither pressure nor velocity profile at the boundary is known prior to the simulation. The outflow boundary condition assumes zero streamwise gradients for all properties except the pressure [11].

```
#include "udf.h"
/*Uout = U + beta(z/h-0.5);*/

DEFINE_PROFILE(xdirection_vec, t, i)
{
    real z, x[ND_ND], p1, p2, p3, p4, p5, p6, dxdy, theta; /* variable
      declarations */

    face_t f;
    /*Curve-fit parameters*/
    p1 = 3.179e-10;
    p2 = 3290;
    p3 = -822.4;
    p4 = 113.1;
    p5 = -8.734;
    p6 = -0.03571;

    begin_f_loop(f, t)
    {
        F_CENTROID(x, f, t);
        z = x[1]; /*Extracting z-values for cells within the screen*/
        dxdy = (p6 + 2 * p5 * z + 3 * p4 * pow(z, 2) + 4 * p3 * pow(z, 3) +
           5 * p2 * pow(z, 4) + 6 * p1 * pow(z, 5)); /*Screen slope*/
        theta = atan(-dxdy);/*Screen normal angle*/


        F_PROFILE(f, t, i) = cos(theta); /*x-component of the screen
          normal*/

    }
    end_f_loop(f, t)
}
```

Figure 3.5: The UDF calculating the x-component of the screen normal angle corresponding to the sixth-order polynomial curve-fit shown in figure 3.4.

- Walls: As the linearized relation by Elder, described in chapter 2.1.2, assumes that viscous effects only are present in the near vicinity of the screen slip walls, i.e. wall with no shear stress are used in the simulations of the closed channel model in this thesis.

The screen is defined as a porous region modelled by the PMM, where the viscous and inertial loss factors in the porous region are determined using the procedure described in chapter 3.1.2. This model provides an efficient way to verify that the PMM is an accurate way of modelling the flow resistance introduced by a screen. The reason is that the model satisfies the assumptions for the linearized relation in equation (2.9) for small changes in

the velocity profile over the screen. Such that the velocity profile predicted by this relation can be used as a benchmark when verifying the numerical model. It may also provide an accurate description of flows through screens in closed channels when no-slip walls are used. The model may also be used as an initial test of the performance of a screen to be used in an open channel, by using a slip-wall at the top and a no-slip wall at the bottom. An illustration of the set-up for the closed channel model is given in figure 3.6.

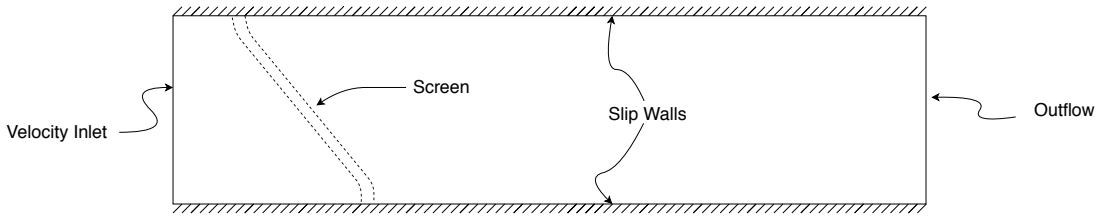

Figure 3.6: A schematic representation of the set-up for the closed channel flow model.

Model 2: Open Channel Flow

The open channel flow model is more intricate than the closed channel model, as it involves interaction between two phases and a free-surface that may deform depending on the flow conditions. The free-surface will generally experience a drop over the screen due to the momentum loss introduced by the screen, which is modelled by the PMM. The geometry in the open channel flow model is fairly similar to the closed channel model, except that an air domain is introduced, such that the screen stretches a little over the initial free-surface. A honeycomb is also introduced downstream of the screen. The multiphase solver used in this thesis is the VOF-model, which was described in chapter 3.1.3, using the open channel flow option. This enables the user to specify a free-surface level at the outlet. The boundary conditions used in this model are the following:

- Inlet: A uniform velocity profile is specified at the inlet.
- Wall: A no-slip condition is used at the bottom wall.
- Outlet: All boundaries except the inlet and the bottom wall of the open channel model are assigned as pressure outlets using the open channel flow option. The pressure is then specified by the adjacent cell at the outlet boundaries, ensuring a zero-pressure

gradient normal to the boundary. This boundary condition will also make sure that the free-surface level at the outlet corresponds to that prescribed by the user.

The screen is defined as a porous region, and it is modelled using the PMM, where the viscous and inertial loss factors are determined using the procedure described in chapter 3.1.2. The loss coefficients need to be approximated for all the phases present in the model, i.e. both air and water in this thesis. The honeycomb will also be modelled as a porous medium, similar to the screen. The loss coefficients will be determined using the procedure given in the part about honeycombs in chapter 3.1.2.

Figure 3.7 illustrates the set-up for the open channel flow model. The honeycomb which appears after the screen was first neglected, but was added for reasons to be explained in chapter 4.2. Honeycomb is also used as flow straightener after the screen in the lab, see figure 1.1.

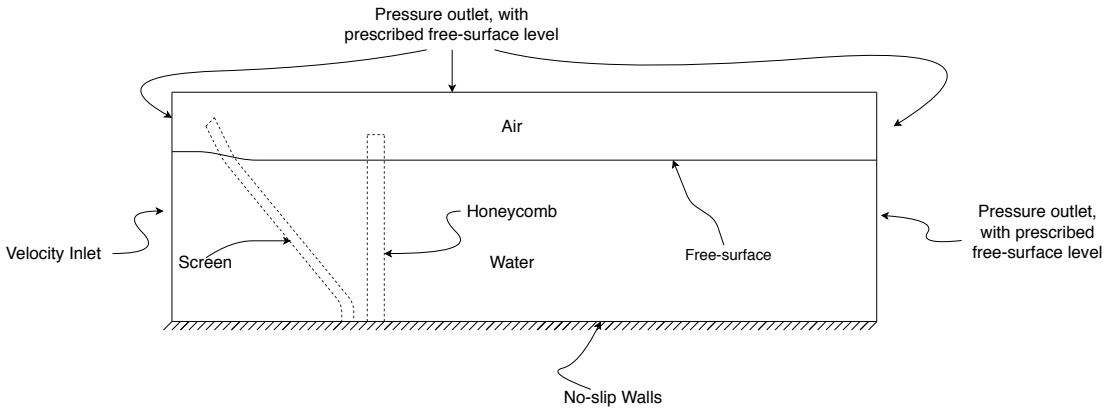

Figure 3.7: A schematic representation of the set-up for the open channel flow model.

Assumptions

The research objectives in chapter 1.2 states that a quasi-2D model or a model with a broader domain, allowing larger spanwise flow structures, should be constructed. However, resolving all flow structures within the screen proved to be a very computationally intensive task. Thus, making the model an inefficient way of simulating flows through screens. The effects of the screen will, therefore, be modelled by the PMM. The screen is then replaced by a homogeneous porous medium that is represented in 2D, and it is therefore assumed that no important spanwise flow structures are present in fluid flows through screens.

Furthermore, as stated in the research objectives in chapter 1.2, the flow is assumed to be laminar, but a quick look at the typical Reynolds numbers associated with the closed and open channel model reveals that this might not be the case. The closed channel flow model is essentially a representation of flow through an infinitely wide screen between two infinitely wide parallel plates. The transitional Reynolds number for a flow between two infinite parallel plates depends on the flow profile. For Poiseuille flow, the critical Reynolds number is around 2510, while Couette flows remains laminar until higher Reynolds numbers [17]. The cases to be studied in this thesis will use water as fluid, with $\rho = 998.2\frac{\text{kg}}{\text{m}^3}$ and $\mu = 0.001003\frac{\text{kg}}{\text{ms}}$, and typical velocities will be in the order of $0.1\frac{\text{m}}{\text{s}}$ with channel height in the order of 0.1m. This results in a Reynolds number of $Re = \frac{\rho U h}{\mu} = \mathcal{O}(10^4)$, which suggests that the flow might be turbulent.

Open channel flows have a transitional Reynolds number around $500 \leq Re \leq 2500$ [4]. The cases to be studied in this thesis will have velocities and water depth in the same order as the closed channel model, i.e. $U = \mathcal{O}(0.1)\frac{\text{m}}{\text{s}}$ and $h = \mathcal{O}(0.1)$m. The hydraulic diameter associated with a 2D open channel flow is the depth of the channel, as the channel essentially has an infinite width. Hence, the Reynolds number associated with the open channel flow to be investigated will be in the order of $Re = \mathcal{O}(10^4)$, which is well above the transitional limit.

However, the flow will be assumed laminar for the cases studied in this thesis, even though that the Reynolds number associated with both the closed and open channel model suggests that the flow might be turbulent. The argument for this is that the screen, and honeycomb, will break the turbulent structures present in the incoming flow down to a scale in the order of the spacing between the wires in the screen, and openings in the honeycomb. This reduction of the turbulent length scales will reduce the turbulence levels downstream of the screen. Cases studied in this thesis will, therefore, not include turbulence modelling as the effects of turbulence are assumed to be negligible. Turbulence reduction caused by screens was well documented by J. Groth and A. Johansson [14].

The following flow assumptions are made:

- Incompressible flow: The flow is assumed to be incompressible, compressible effects are unlikely to occur considering the relatively low velocities that are associated with the cases studied in this thesis.

- Laminar flow: The flow is assumed to be laminar for all cases studied in this thesis.

- Uniform inlet velocity: This is assumed for both the open and closed channel flow, but an inlet length in the order of one channel height/water depth is used in all simulations.
- Outlet: A zero streamwise pressure gradient is assumed for the open channel model. A zero streamwise gradient is assumed for all properties except the pressure for the closed channel model.
- Negligible surface tension effects: The Weber number, calculated in chapter 3.1.3 suggests that the effect of surface tension may be neglected. A case simulated with and without including surface tension modelling will be presented to investigate the effect of surface tension.
- The flow resistance introduced by a screen may be accurately predicted by a homogeneous porous medium. It is also assumed that the pressure drop coefficient suggested by Brundrett [2] given in equation (2.21) accurately predicts the pressure drop coefficient of screens. The same accounts for honeycombs, which are modelled in a similar way using the same equation with an adjusted porosity to approximate the flow resistance. The Reynolds number used when calculating the pressure drop over the honeycomb was calculated using the diameter of screen 2 in table 3.1.
- Walls are assumed to be accurately represented by no-slip and no-penetration boundary conditions.
- No relevant spanwise flow structures as only 2D models will be investigated in this thesis.
- No relevant thermal effects.

3.3 Verification and Validation

CFD is a powerful tool that may generate an enormous amount of data and provide accurate solutions for fluid flows for numerous applications. It may also provide solutions that seem reasonable despite having no root in reality. It is therefore essential to critically evaluate the results through a proper verification and validation process. Verification is the process of making sure that the numerical model solves the physical model accurately, while validation is the process of determining if the model is an accurate representation of real life flows [26].

3.3.1 Verification

For most purposes, only an isolated domain of a system or process, including the most relevant physical effects are analyzed. The reason is that resolving the whole system will often be very computationally intensive and sometimes also technically impossible. A physical model representing an isolated domain of the system, in which the system behaviour and physical phenomena need to be better understood, is then made. As only a part of the system is analyzed, a proper set of boundary conditions are needed. These boundary conditions are predictions of the flow conditions at the boundaries of the isolated domain. The verification process uses certain benchmarks to verify that the CFD-model adequately represents the physical model, and such benchmarks may be exact analytical or accurate numerical solutions [26]. A proper verification process includes an investigation of the CFD code, i.e. ensuring that the governing equations are solved correctly with the desired order of the truncation errors etc. As ANSYS Fluent is a commercial software, this part of the verification process is assumed to have been carried out by the developer. The verification process in this thesis will, therefore, focus on how well the numerical model performs compared to the physical model.

The solutions by Elder [7], equation (2.9), and Dunn and Tavoularis [6], equation (2.18) with (2.19), are assumed to be accurate solutions for the given problem and they will be used as benchmarks in order to verify that the CFD-model adequately represents the physical model. Furthermore, it is important to check the consistency and convergence of the iterative solution, i.e. ensuring that the solution is physical and that the residuals and other quantities relevant to the flow, e.g. pressure drop over the porous region, converges. Another important step in the verification procedure is to analyze the discretization error, which may be performed by a mesh convergence test. This is also a crucial step used to ensure that the solution is independent of the mesh.

3.3.2 Validation

The validation process may start once the numerical model has been verified to give an accurate representation of the physical model. CFD-results are often compared to experimental data to determine to what degree of accuracy the model reproduces the phenomena that occur in real life. A conclusion on whether or not the CFD-model is an accurate representation of real life is the main purpose of the validation process [26], where experimental

data are used as a benchmark for the numerical solution. A difficulty with validation using experimental data is that these data are not free of errors themselves, and the uncertainty in the experimental data should be considered when validating the numerical model.

PhD Candidate Benjamin Smeltzer has provided experimental data for flow through screens using the set-up in the fluid mechanics lab at NTNU. These data will be used for validation purposes in this thesis.

3.4 Mesh and Mesh Independence

This chapter describes how the mesh has been constructed for the models in this thesis and discuss the results of the mesh independence study.

3.4.1 Mesh for the Closed Channel Flow Model

A simple mesh, only restricting the maximum cell size was used for the closed channel flow model for the case with slip walls. If a no-slip condition is applied at the walls, a refinement close to the walls should be used to resolve the boundary layers adequately. This can be performed by using the "Inflation layers"-option in ANSYS Meshing, 8-10 of these layers will usually be enough to resolve the boundary layers properly. Figure 3.8 shows the geometry used in the mesh independence test. The screen, in this case, is designed to transform a flow of water with a uniform inlet velocity of $0.05\frac{\mathrm{m}}{\mathrm{s}}$ into a uniformly sheared outlet velocity profile with a shear parameter $\beta = 0.25$. An illustration of the mesh for the geometry given in figure 3.8 is given in figure 3.9. This is how a typical mesh for the closed channel flow model with slip walls looks like. The porous region, in this case, models the effect caused by screen 1 in table 3.1, such that the thickness of the porous region is 0.45mm.

3.4.2 Mesh for the Open Channel Flow Model

The mesh used for model 2, the open channel model, needs more mesh controls than the one for the closed channel model. One reason is that a no-slip boundary condition is used at the bottom wall, such that a local refinement is needed close to this wall to resolve the boundary layer properly. The geometry for the case that models the set-up of the lab, which is illustrated in figure 1.1, is given in figure 3.10. Observe that bottom 4mm of the geometry has been divided from the rest. The reason for this is to simplify the mesh refinement close

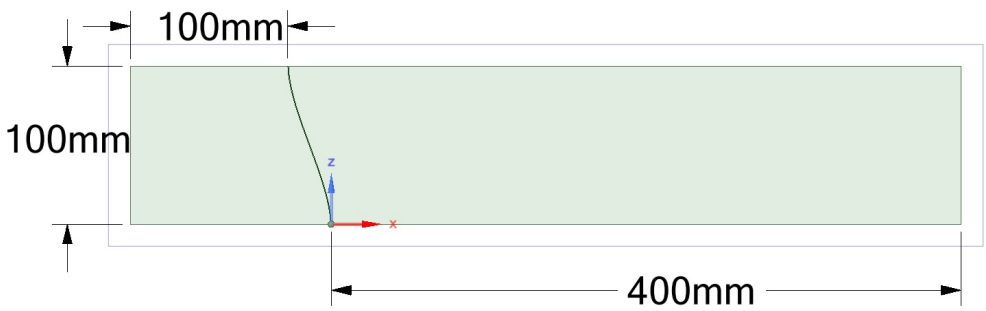

Figure 3.8: Illustration of a typical geometry used for the cases of the closed channel flow model, Model 1. The screen shape will vary from case to case, where the present screen is designed to transform a flow of water with a uniform inlet velocity of $0.05\frac{\mathrm{m}}{\mathrm{s}}$ into a uniformly sheared outlet velocity profile with a shear parameter of $\beta = 0.25$.

to the wall. The difference in the water depth between the inlet and the outlet is 2mm, and this is because the water depth will decrease over the screen due to the pressure drop. The value of 2mm was determined by first running a simulation with no difference and then look at the water depth upstream of the screen. This simulation showed that the water depth upstream of the screen increased by 2mm.

Figure 3.11 shows the mesh in the region around the porous regions modelling the screen and the honeycomb close to the bottom wall. The cell refinement close to the wall is well illustrated along the bottom of this figure. The figure also shows that the mesh consists of mostly structured cells, which is possible due to the simple geometry. As already mentioned, the bottom 4mm of the channel has been divided from the rest of the geometry, this was performed to get better control of the cell refinement close to the wall. The cell refinement was generated using the "Number of divisions" option on the vertical edges of the bottom region. A total of 40 divisions was used, creating 40 cells layers in the bottom 4mm of the channel. The bias-function was used such that the cells were gradually refined the closer the cells were to the wall. A bias-factor of 8 proved to give good results. The quality of the mesh using the mesh metrics discussed in chapter 3.1.1 will be presented together with the result of the mesh independence analysis in chapter 3.4.3.

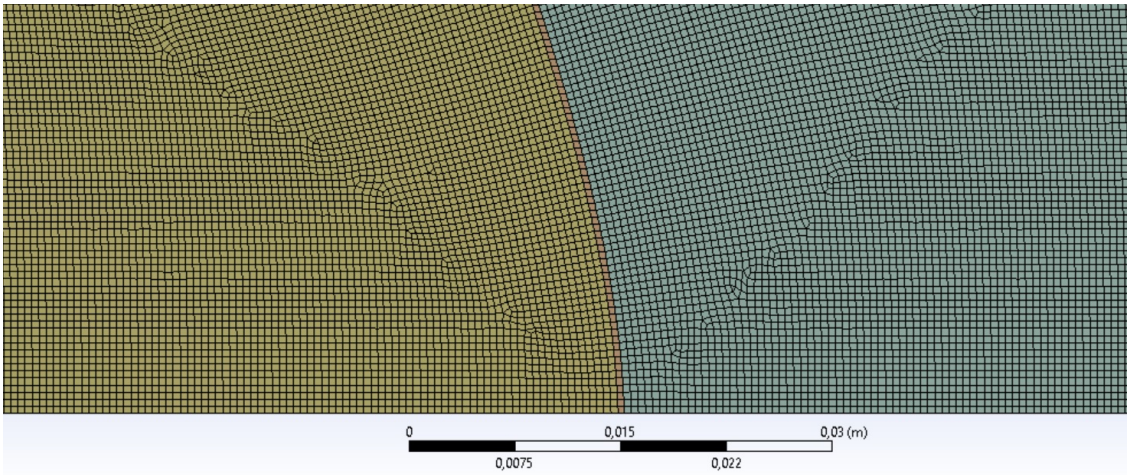

Figure 3.9: Illustration of how a typical mesh for the closed channel flow model looks like. This figure shows the mesh in the region around the porous region modelling the screen.

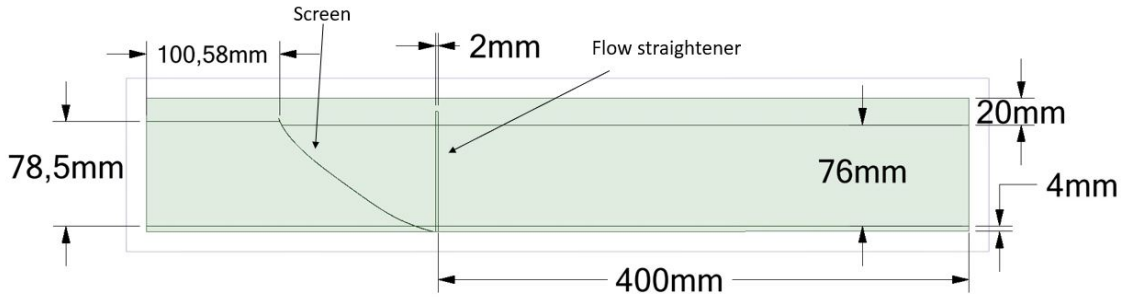

Figure 3.10: Description of the geometry used for a typical case of the open channel model. The inlet and outlet are always placed, respectively, $\sim$ 100mm upstream and $\sim$ 400mm downstream of the screen.

3.4.3 Mesh Independence

As mentioned in chapter 3.3.1, a mesh convergence study is a crucial step to verify the CFD-model. This must be performed to ensure that the solutions obtained through the CFD-simulations are independent of the mesh.

Mesh convergence for the Closed Channel Flow Model

The mesh convergence study for the closed channel flow model was performed by computing the resulting outlet velocity profile for several meshes, where the only difference was the cell size restriction. Meshes of maximum cell size ranging from 40mm down to 0.4mm were used

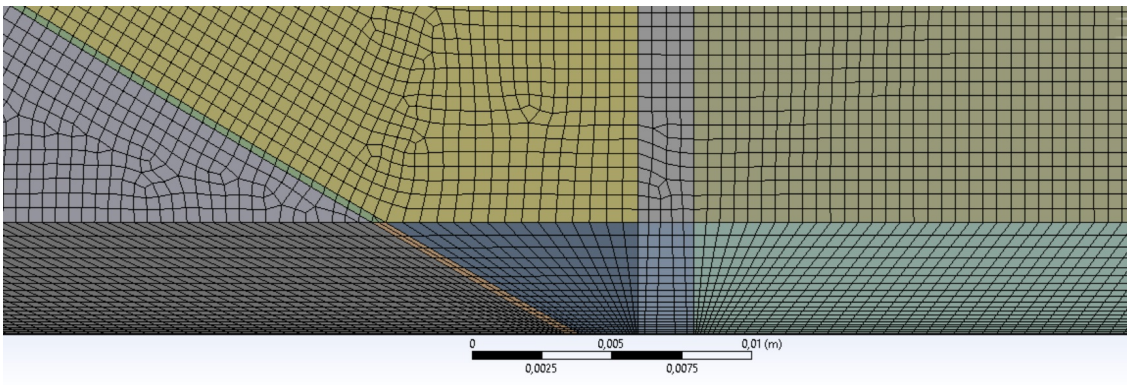

Figure 3.11: Illustration of the mesh in the region around the screen close to the bottom wall for the open channel model.

to study the convergence of the solution. The result of the mesh convergence study can be found in figure 3.12. This figure shows that the relative difference between the design downstream profile and the downstream profile resulting from the CFD-analysis is practically unchanged when the number of mesh nodes exceeds about $4 \cdot 10^3$. The maximum cell size used for some of the meshes in the mesh convergence study may be seen from the legend in figure 3.12. It may be argued that the solution has sufficiently converged at around $4 \cdot 10^3$ mesh nodes, as the relative error does not change considerably when increasing the number of mesh nodes from here on. For this mesh convergence study slip walls have been used, as the results from this model will be compared to the velocity profile predicted by the linearized relation in equation (2.9). Slip walls are used to get a better agreement, as the viscous effect is neglected everywhere except in the near vicinity of the screen in the derivation of equation (2.9).

Mesh convergence for the Open Channel Flow Model

The mesh convergence test for the open channel model was performed in the same way as for the closed channel model, i.e. by gradually refining the cells. The velocity profile resulting from each mesh was then compared with experimental data and the profile of the finest mesh, to determine whether the solution had converged or not. The result of this analysis may be found in figure 3.13. In this figure, the relative difference and the two-norm of the difference of the velocity profile resulting from each mesh are compared with experimental data and the solution using the finest mesh. The viscous and inertial loss factor, D and C,

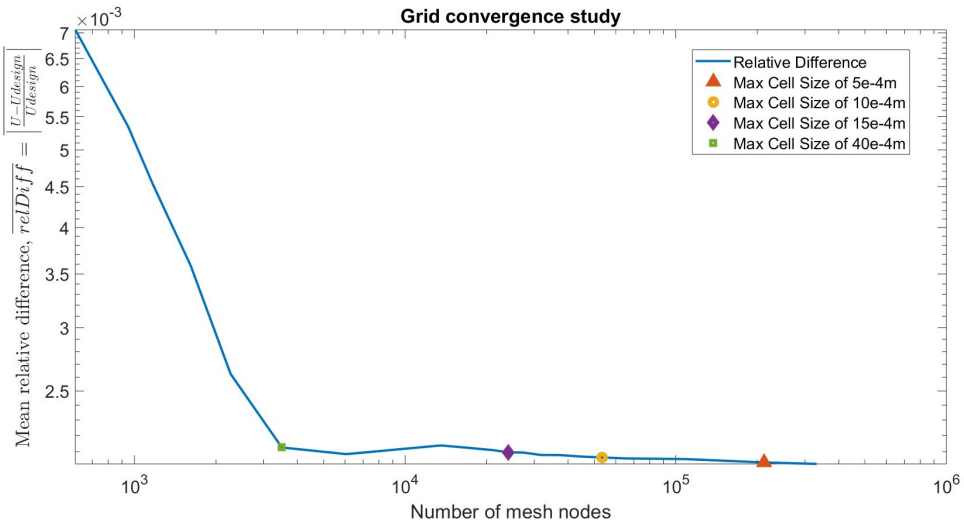

Figure 3.12: The plot shows how the solution becomes independent of the mesh when the mesh is gradually refined for the closed channel flow model. Observe how the relative difference between the design profile and the profile resulting from the CFD-analysis approaches a constant value when the mesh is refined.

was determined using the screen parameters of screen 2 in table 3.1 and the procedure given in chapter 3.1.2. The reason for using this screen is that it was used when the experimental data was gathered by PhD Candidate Benjamin Smeltzer. These experimental data and the solution using the finest mesh will be used to determine when the solution of the model becomes mesh independent.

The result of the mesh independence study, given in figure 3.13, shows that the difference between the solution on each of the tested meshes is small, even though the cell sizes used ranges from 30mm to 0.35mm. The change in the differences, relative and two-norm, tends to vanish when increasing the number of nodes from above around $2 \cdot 10^5$ as seen in the plots of figure 3.13. The solution is therefore said to be mesh independent, as a further refinement of the cells does not change the solution. The maximum cell size for the mesh resulting in $\sim 2 \cdot 10^5$ nodes is 0.5mm, and this will be used for the cases to be presented later.

An explanation to why the relative error compared to the experimental measurements is relatively large, is that the experimental measurements did not contain any data for the bottom 25% of the channel. The volume flow rate was therefore approximated using these data, knowing that the velocity had to be zero at the wall. This will be discussed more in chapter 4.2, where these experimental data have been used to validate the model.

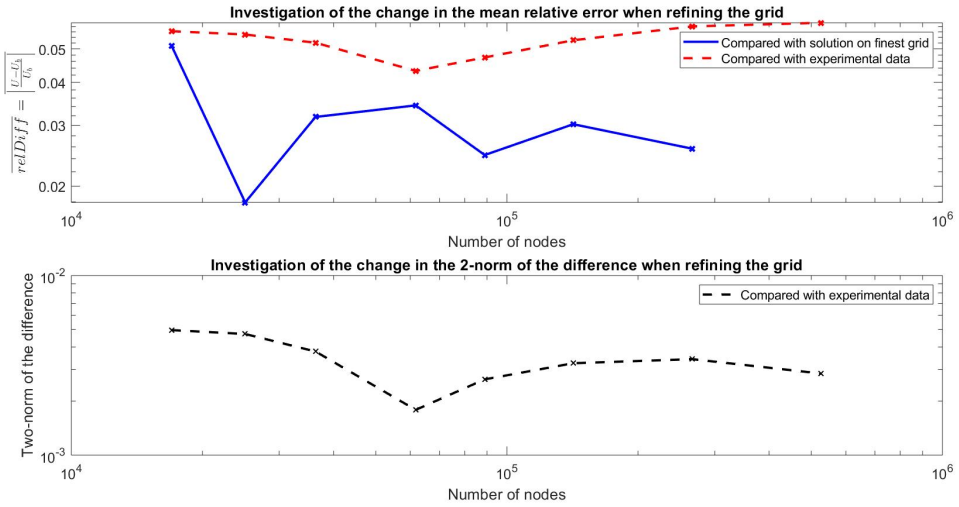

Figure 3.13: Plot of the relative difference (top plot) and two-norm of the difference (bottom plot) of the velocity profile resulting from the CFD-analysis of a gradually refined mesh compared to the velocity profile from experimental data and on the finest mesh.

The mesh metrics discussed in chapter 3.1.1 are used to evaluate the quality of the meshes used in this mesh independence study, and the average values of the mesh metrics are given in table 3.2. The minimum and maximum values present in this table are averages of the minimum and maximum values for all the meshes used in the study of the open channel flow model. Although the average maximum skewness value is relatively high, almost 0.85, it is still below the deterioration limit of 0.95 [8]. The average skewness is also very close to zero, in addition to the fact that the average orthogonal quality is very close to one. This suggests that this mesh set-up yields good quality meshes. Refinement of the mesh gives even better values for the mesh metrics, e.g. max and average skewness are reduced, while minimum and average orthogonal quality increases.

Table 3.2: The average mesh metrics of the meshes used in the mesh independence study, where min and max values are averages of the minimum and maximum values for the meshes present in this study.

	Min	Average	Max
Skewness	-	0.104	0.846
Orthogonal Quality	0.261	0.943	-

Chapter 4

Results and Discussion

This chapter will present and discuss the most relevant results from the simulations using the CFD-models presented in chapter 3.2. The chapter will start with a verification section, where residuals are inspected, and the resulting outlet velocity profile from a variety of closed channel flows will be compared with the design and theoretically estimated outlet profile given the flow conditions. This is followed by a validation section where the results from an open channel flow simulation of the lab set-up are validated using experimental data. After the numerical model has been thoroughly verified and validated, the results of several cases investigating how the flow is affected by varying:

- the screen shape and curvature,
- the inlet velocity,
- the water depth on the channel,

will be presented and discussed.

4.1 Verification of model

Parts of the verification process have already been conducted, as stated in chapter 3.3.1 it is assumed that the algorithms and solution schemes provided in ANSYS Fluent 19.2 already have been verified by the developer. Furthermore, a grid convergence test has been performed for the closed channel model, and the result was given in chapter 3.4.3. This result showed that the solution for the closed channel flow model was essentially unchanged when the cells

were refined to produce cells smaller than a max cell size of 4mm, which corresponds to about $3.5 \cdot 10^3$ number of mesh nodes. A max cell size of 0.5mm, which is much smaller than the cell size needed to get a grid independent solution, was used to produce the results from the closed channel simulations that will be presented in this chapter. A grid convergence test was also performed for the open channel model, and the result of this test was given in chapter 3.4.3. This test showed that a grid independent solution was obtained through the CFD-analysis when the maximum cell size was 0.5mm, and 20 wall layers were used in the bottom 4mm of the channel. These mesh controls were used to generate the results of the open channel flow model that will be presented in this thesis.

Another important step of the verification process is to ensure that the solution of the CFD-model converges, this may be performed by a comparison of the initial and final residual for an iterative solution. Such a comparison may be seen in figure 4.1, where the scaled residuals are plotted for every iteration until the convergence criterion is met for a closed channel flow case. The convergence criterion used in this simulation was 10^{-10}, i.e. all the scaled residuals should be equal or lower than this limit before stopping the iteration process. The definition of these residuals, and how they are scaled, may be found in [12]. A look at the residuals alone is often not enough, as some solutions may be unphysical although the iterations have converged. A quick check that the solution is mass conserving should always be performed. This may easily be checked by computing the mass flux into and out of the domain for the solution. For the specific case represented in the residual plot, the net mass flux into the domain was $8.88 \cdot 10^{-16} \frac{\text{kg}}{\text{s}}$, whereas the inlet mass flow rate was $4.99 \frac{\text{kg}}{\text{s}}$. As the net mass flow rate is much lower than the inlet mass flow rate, the solution is considered to be mass conserving.

The convergence criterion set for the open channel model is different from the one described for the closed channel model. The reason is that the CFD-model for the open channel flow case needs to be solved using a transient solver. A convergence criterion will then be defined for the iterations that are performed for each time step. The convergence criterion used in the simulations presented in this thesis was 10^{-6}, with a maximum of 25 iterations per time step. The solver would then iterate until the convergence criterion is met, or until the maximum number of iterations have been performed before calculating the solution for the next time-step.

Four different cases using the closed channel model with slip-walls were tested to verify that the PMM accurately models the effects that a physical screen introduces to a flow.

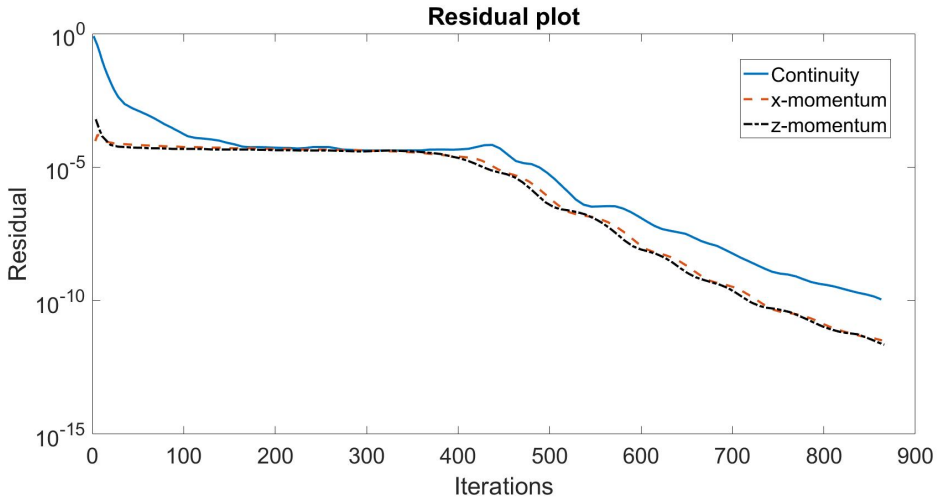

Figure 4.1: Typical residual plot for the closed channel flow model. This plot illustrates how the residuals change as a function of iteration number.

The screen shapes for these four cases are shown in figure 4.2, in which all the shapes were determined using the MATLAB script given in appendix A.1. This script uses the iterative procedure given in chapter 3.2.1. The four screen shapes were generated using the screen parameters of screen 1 in table 3.1 and a uniform inlet flow of $0.05\frac{\mathrm{m}}{\mathrm{s}}$. The loss factors used in the PMM were estimated using the procedure given in chapter 3.1.2 and are given in table 4.1. These values are used for all the closed channel flow cases presented in this thesis. The difference between the screen shapes given in figure 4.2 is the outlet velocity profiles that the screens are designed for, which may be seen in figure 4.3. This figure shows a comparison between the design profiles and the profiles resulting from the CFD-simulations.

Table 4.1: The loss factors used for all the closed channel flow cases presented in this thesis.

C	3009
D	$7.7589 \cdot 10^7$

Figure 4.3 shows an almost perfect agreement between the velocity profile resulting from the CFD-analysis and the velocity profile that the screens were designed for. This verifies that the PMM accurately predicts the flow disturbance introduced by a screen. At least the effects governed by the linearized relation, equation (2.9), which was used to determine the screen shapes.

Another verification test was performed as well, but for this test, three different screen

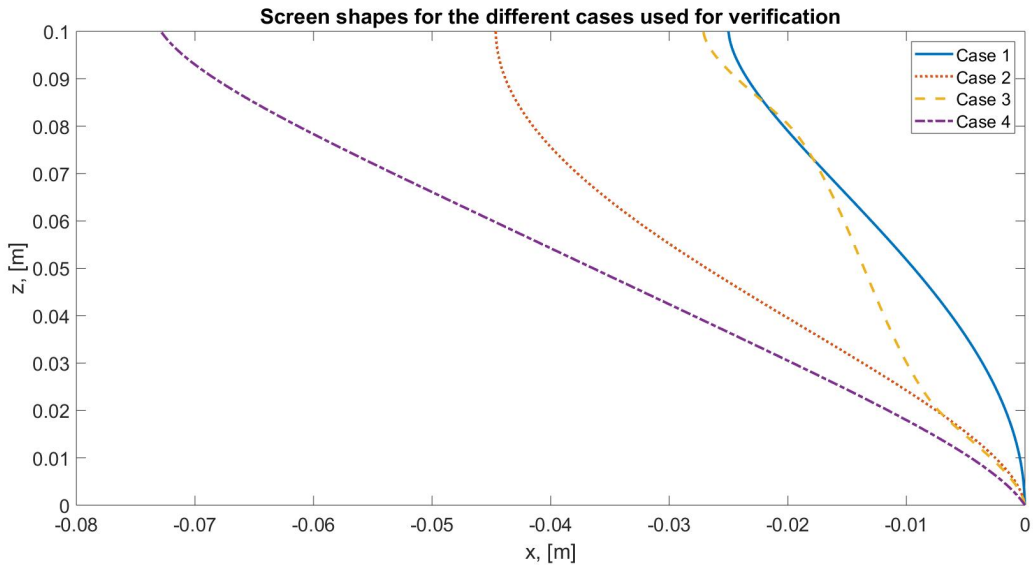

Figure 4.2: The solution provided by the linearized relation for the screen shape assuming uniform inlet flow and four different downstream velocity profiles, which are shown in figure 4.3, using the parameters of screen 1 in table 3.1.

shapes were tested using four different inlet velocities. These cases were constructed to test the performance of the screen shapes outside the design conditions. The three different screen shapes were determined by using the parameters for screen 1 in table 3.1 and using the same design inlet and outlet velocity profiles. The inlet was defined as a uniform velocity of $U = 0.05\frac{\mathrm{m}}{\mathrm{s}}$, while the outlet profile was defined as a uniformly sheared velocity profile with a shear parameter $\beta = 0.25$. The difference between the screens was the expression used to determine the screen shape. In which one was determined by the expression of Dunn and Tavoularis [6], i.e. equation (2.18) with (2.19). Whereas the remaining two were determined by the iterative procedure described in chapter 3.2.1, where one of the shapes was calculated including the term that describes the variation in the resistance of the screen, the s-term, and the other without taking this term into account. The resulting screen shapes can be seen in figure 4.4. From this figure, it can be seen that the screen shapes determined by the expression by Dunn and Tavoularis [6] and the iterative solution without including the s-term look very similar. However, the screen shape determined by the latter method is slightly more curved upwards at the top of the channel such that it has a smaller extent in the streamwise direction. The screen determined by the iterative solution including the

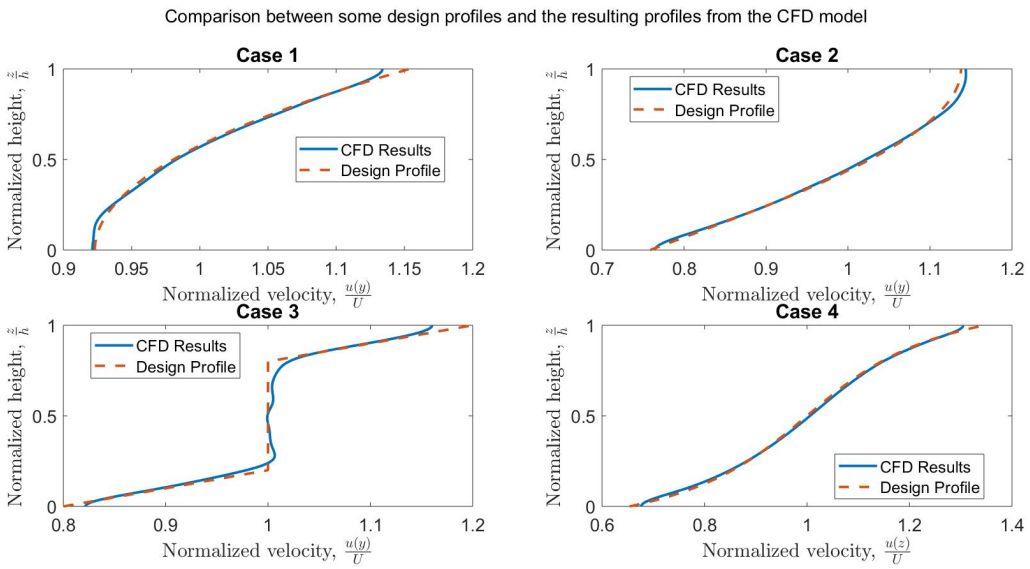

Figure 4.3: Comparison between the velocity profile the screens were designed for and the velocity profiles resulting from the CFD-simulations using these screen shapes. The cases in this figure corresponds to the cases specifying the screen shapes in figure 4.2.

s-term has a slightly different shape than the other two, see figure 4.4, and it does also have the smallest extent in the streamwise direction. The reason for this is that the resistance variation term, $s(z)$, tends to reduce the inclination of the screen [3].

The performance of each of these screen shapes were then tested using the closed channel model at four uniform inlet velocities ranging from $U = 0.03\frac{\mathrm{m}}{\mathrm{s}}$ to $U = 0.08\frac{\mathrm{m}}{\mathrm{s}}$. The resulting downstream velocity profile for each of these screens can be seen in figure 4.5. From this figure, it can be seen that the screen shape determined by the iterative solution of equation (2.9), taking the resistance variation into account does not perform very well at producing a uniform shear. This proves that the screen shape calculated by neglecting this term performs better at producing the desired velocity profile, at least for cases similar to this one. The resistance variation term, $s(z)$, has therefore been neglected from the calculations of all other screen shapes in this thesis.

The screens determined by the expression suggested by Dunn and Tavoularis [6], equation (2.18) with (2.19), and the iterative solution of equation (2.9) without taking the resistance variation into account, produce approximately uniformly sheared downstream velocity profiles close to the theoretical prediction. The theoretically predicted velocity profiles were

calculated using the MATLAB function provided in appendix A.2, which solves equation (2.9) neglecting the effect of the resistance variation. From this figure, it is also evident that the iteratively calculated screen shape determined using equation (2.9) performs better at producing the desired velocity profile, even for different velocities than the design velocity. An explanation to why the iterative screen shape performs better than the one suggested by Dunn and Tavoularis [6] may be that their expression can be interpreted as a first iteration solution as γ_0 is set equal to K and that their solution is an approximation of the analytical solution. It should also be mentioned that the expression by Dunn and Tavoularis, equation (2.18) using (2.19), is applicable to produce uniformly sheared downstream velocity profiles from uniform inlet conditions only.

The shear parameter, β, for the theoretically predicted velocity profiles are tabulated in table 4.2. This table shows a clear trend of decreasing shear parameter with increasing inlet velocity. Which suggests that the screen is less able to transform the velocity profile of flows with a higher mean velocity, which is an effect that will be investigated further in chapter 4.4.

Table 4.2: Comparison of the shear parameter of the downstream velocity profiles corresponding to the cases with different inlet velocities illustrated in figure 4.5.

U	$0.03\frac{\mathrm{m}}{\mathrm{s}}$	$0.05\frac{\mathrm{m}}{\mathrm{s}}$	$0.06\frac{\mathrm{m}}{\mathrm{s}}$	$0.08\frac{\mathrm{m}}{\mathrm{s}}$
β	0.308	0.250	0.234	0.209

The screen shape determined by the iterative solution of equation (2.9) without taking the resistance variation, i.e. the $s(z)$-term, performs best at producing the desired velocity profile as seen from figure 4.5. This method should, therefore, be preferred when determining the screen shape needed to generate a specific downstream velocity profile. The mesh independence test, the inspection of residuals, and this comparison to the theoretically estimated velocity profiles make up the verification process. The results verify that the CFD-model using a porous region to model the flow resistance introduced by a physical screen is an adequate representation of the physical model. This is concluded based upon the almost perfect agreement between the theoretically estimated velocity profiles and the velocity profiles resulting from the CFD-simulations, see figure 4.3 and 4.5.

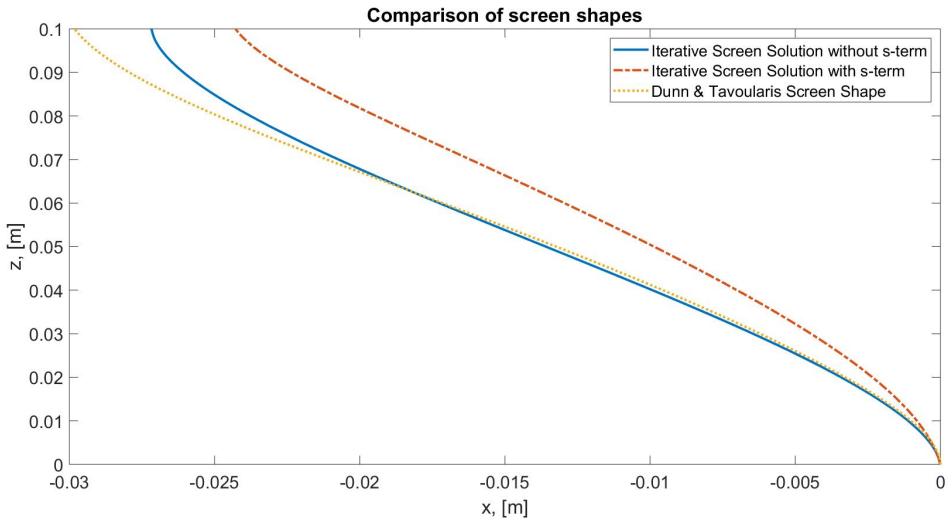

Figure 4.4: Comparison the screen shapes determined using the expression by Dunn and Tavoularis [6], equation (2.18) with (2.19), and using the iterative procedure for calculating the screen shape using equation (2.9), both with and without taking the resistance variation into account, i.e. the $s(z)$-term. The screens are designed for a uniform inlet velocity of $U = 0.05\frac{\mathrm{m}}{\mathrm{s}}$ and a downstream shear parameter $\beta = 0.25$.

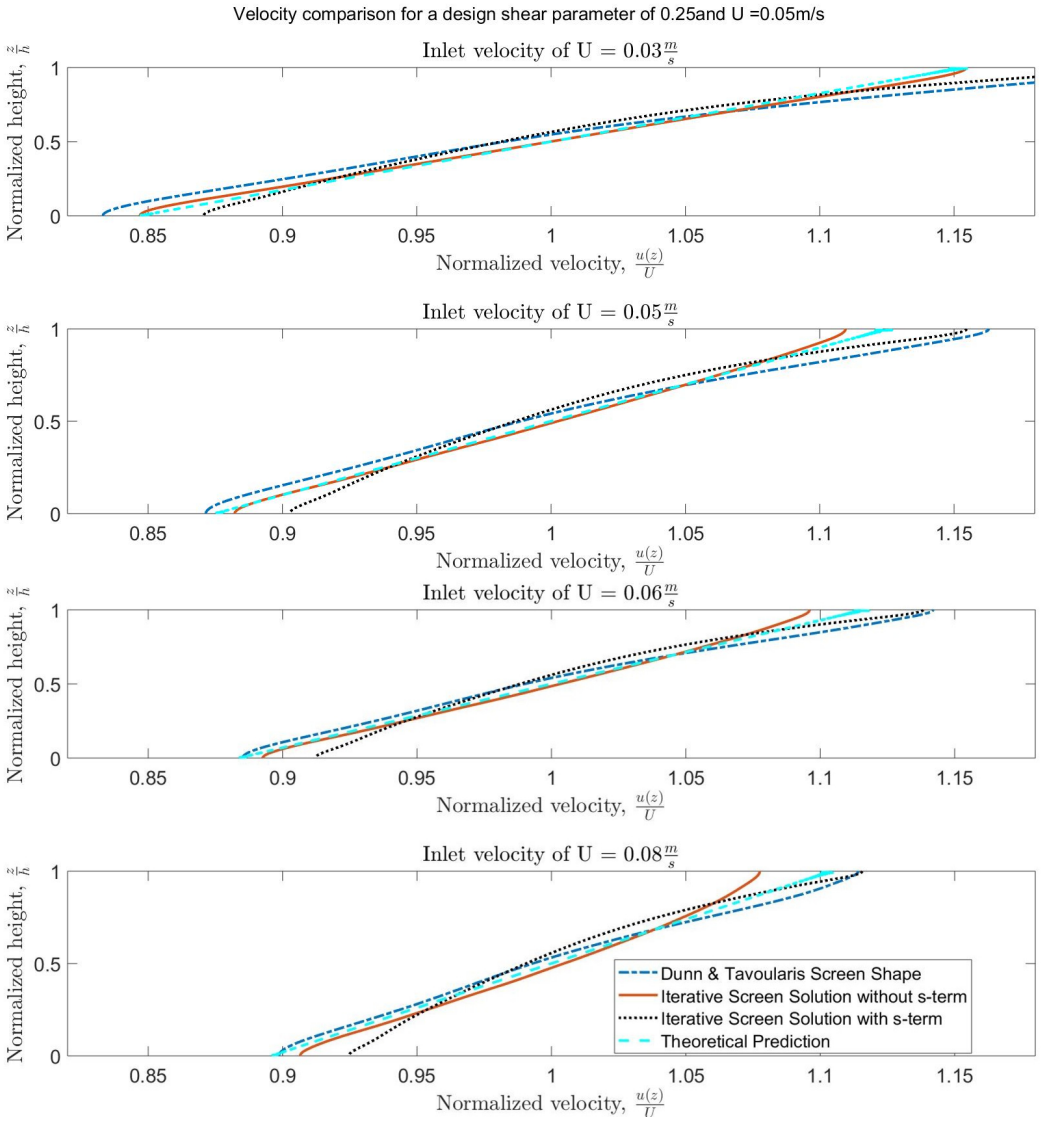

Figure 4.5: Comparison of the velocity profiles resulting from the CFD-analysis using the closed channel model for the screens illustrated in figure 4.4. The legend in the bottom plot applies to all four plots.

4.2 Validation of model

Validation of the CFD-model will be performed by comparing the velocity profile downstream of the screen resulting from a CFD-simulation with experimental measurements from the lab provided by PhD Candidate Benjamin Smeltzer.

The screen in the lab had unfortunately only been shaped manually by adjusting the screen shape until a preferable downstream velocity profile was produced. Such that the shape of the screen in the lab was unknown and had to be measured before a numerical model of the lab set-up could be constructed. The screen shape was, in lack of a better option, extrapolated by hand. This was done by placing a piece of paper at one of the ends of the screen and then drawing a line along with the shadow of the screen that was visible on the paper. This paper was then scanned such that this line could be translated into a set of discrete points defining the shape of the screen to be used in the numerical model. The screen shape used in the numerical model of the lab is given in figure 4.6.

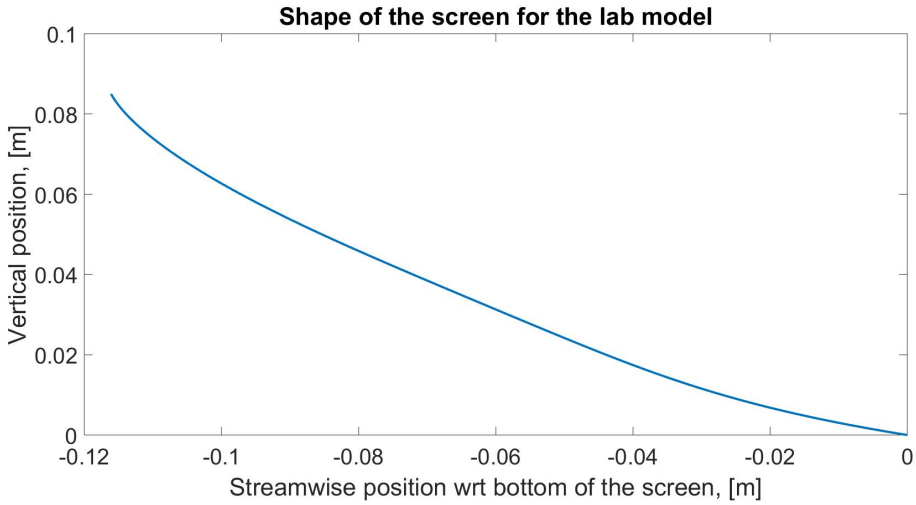

Figure 4.6: Shape of the screen in the CFD-model of the lab set-up.

The inlet velocity used in the numerical model of the lab had to be estimated using the experimental data, as the mean velocity of the flow will influence the velocity profile produced by the screen. This was observed in chapter 4.1, see figure 4.5, and this effect will also be investigated further in chapter 4.4. Experimental measurements are unfortunately not available for the bottom 25% of the channel. The reason for this is that near the bottom there tend to be more stray reflections and scattering of particles, which will contaminate the result near the bottom of the channel. The velocity field in this region is of no interest for the ongoing research in the lab, so no attempts have therefore been made to fix this flaw. The velocity profile for the bottom 25% of the channel was therefore estimated by assuming a no-slip condition at the bottom and fitting a typical boundary layer influenced velocity profile to the measured profile. By using this procedure, the mean velocity of the

measurements was estimated to $0.12\frac{\mathrm{m}}{\mathrm{s}}$, such that the uniform inlet velocity of the numerical model was set to $U_{in} = 0.117\frac{\mathrm{m}}{\mathrm{s}}$. This is slightly less as the water depth decreases a little over the screen, such that the difference in water depth up and downstream of the screen is 2mm in the CFD-model.

The loss factors for the screen and the honeycomb used in the PMM were estimated using the procedure given in chapter 3.1.2 and are presented in table 4.3. These values were calculated using the parameters of screen 2 in table 3.1. All open channel flow cases investigated in this thesis have used the values for the loss factors given in table 4.3.

Table 4.3: The loss factors used in all the open channel flow cases investigated in this thesis.

	Screen		Honeycomb	
	Water	Air	Water	Air
C	7948	4807	88.3	800
D	$3.5541 \cdot 10^8$	$6.2727 \cdot 10^7$	$3.2173 \cdot 10^6$	$1.5410 \cdot 10^7$

The honeycomb present after the screen in the lab set-up, see figure 1.1, was not included in the first CFD-model of the lab. The reason for adding a porous region modelling the flow straightening effect that a honeycomb introduces to a flow, was that the flow never seemed to reach a uniform state behind the screen without this straight porous medium. The explanation for this is that vortices are created right downstream of the screen near the bottom of the channel. These vortices grow until they suddenly detached from the screen and are convected downstream in the channel, and a new vortex starts to build up. An explanation to why these vortices occur may be the large angle between the flow direction and the screen normal vector near the bottom of the channel. This results in a large deflection of the streamlines resulting in a recirculation zone, a vortex, right downstream of the screen and that this vortex sometimes detaches from the screen and is convected downstream with the flow. This effect can be seen in figure 4.7, which is the resulting contour plot of a CFD-simulation of the numerical model of the lab without including a flow straightening porous medium. This figure clearly shows the vortices that are convected downstream with the flow, where rings illustrating the vortices have been drawn in the bottom contour plot. The free-surface is roughly located in the region where the velocity suddenly drops, i.e. where there is a sharp transition from light to dark in the upper half of the contour plots. A velocity contour plot of the same set-up, including a porous medium modelling the flow straightening

effect of the honeycomb, can be seen in figure 4.8. The vortices present in figure 4.7 have almost disappeared, and only a minor effect of these vortices are still present near the bottom of the channel. Hence, resulting in a more uniform velocity field downstream of the screen. The slight drawback with using a porous medium as flow straightener is that standing waves occur downstream of the screen, as seen from the wobbly structures in the upper half of the contour plot in figure 4.8. These waves do also occur downstream of the honeycomb in the lab.

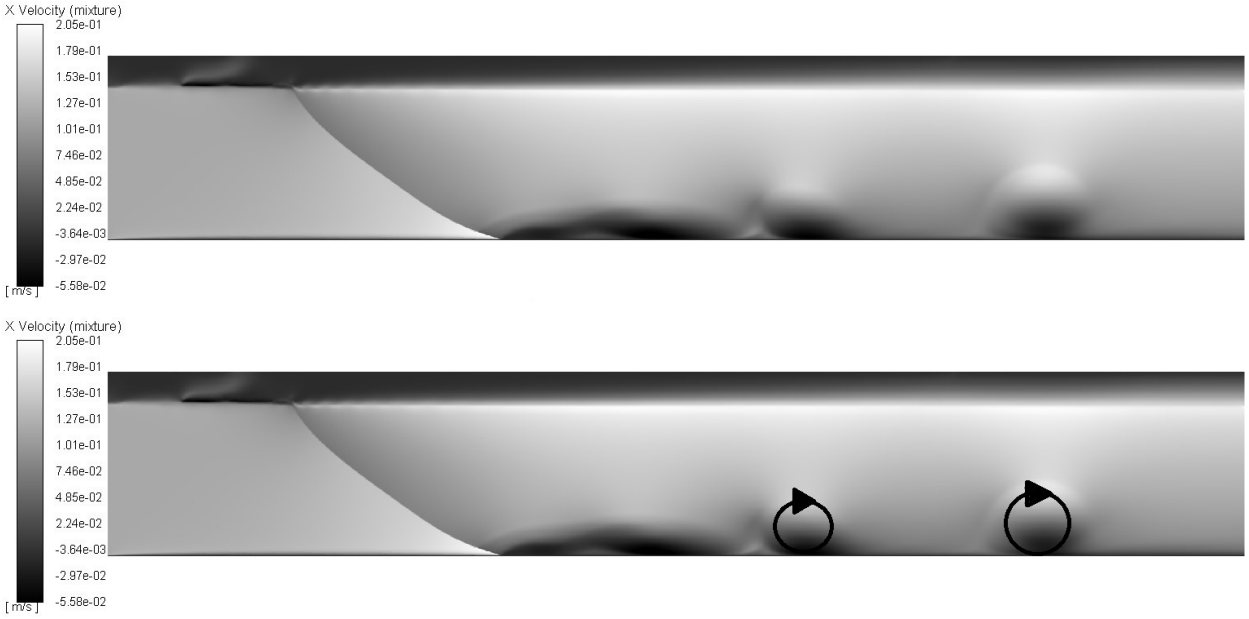

Figure 4.7: Velocity contour plot of the case where a flow straightening porous region, modelling the effect of a honeycomb, is not present downstream of the screen. Observe the vortices that are convected with the flow. Both figures are taken at the same time-instant.

Figure 4.8: Velocity contour plot when a flow straightening porous region, modelling the effect of a honeycomb, is present downstream of the screen. Observe that the vortices present in figure 4.7 have almost disappeared. This contour plot is taken at the same time-instant as those in figure 4.7.

The lab measurements were time-averaged over a minute, such that effects of vortices will not be present in the measurements. Instead of running simulations to a flow time above one minute, a spatial average is used for estimating the velocity profile resulting from the CFD-simulations. The reason for this is that producing a time-averaged velocity profile over one minute for the CFD-simulations would be very time-consuming in comparison. For the lab case, in which the water depth is 8cm, the velocity profile was averaged over a region that spans 18cm in the streamwise direction of the downstream region. Stretching from 20cm to 38cm downstream of the screen. This spatial averaging was performed to suppress the effect of vortices that may be present in the flow. The CFD-simulation was run until a flow time of 15 seconds, in which the velocity profile had reached a seemingly steady-state solution when the effect of the vortices was neglected. The mean relative difference between the velocity profile at several instants and the velocity profile at a flow time of 15s is given in the plot in figure 4.9. The mean relative difference between the velocity profile at flow time at both 13s and 14s compared to the velocity profile at 15s is about 1.3%. This difference is presumably due to the effect the vortices present in the flow. It is therefore assumed that the flow has reached a steady-state at a flow time of 15s.

A comparison between the spatially averaged velocity profile from the CFD-analysis and the velocity profile measured in the lab can be found in figure 4.10. This figure shows that the CFD-model performs well at predicting the velocity profile, as the CFD-result almost coincides with the average velocity profile from the measurements made in the lab in most of the vertical positions in the channel. The bars included for the experimental measurements

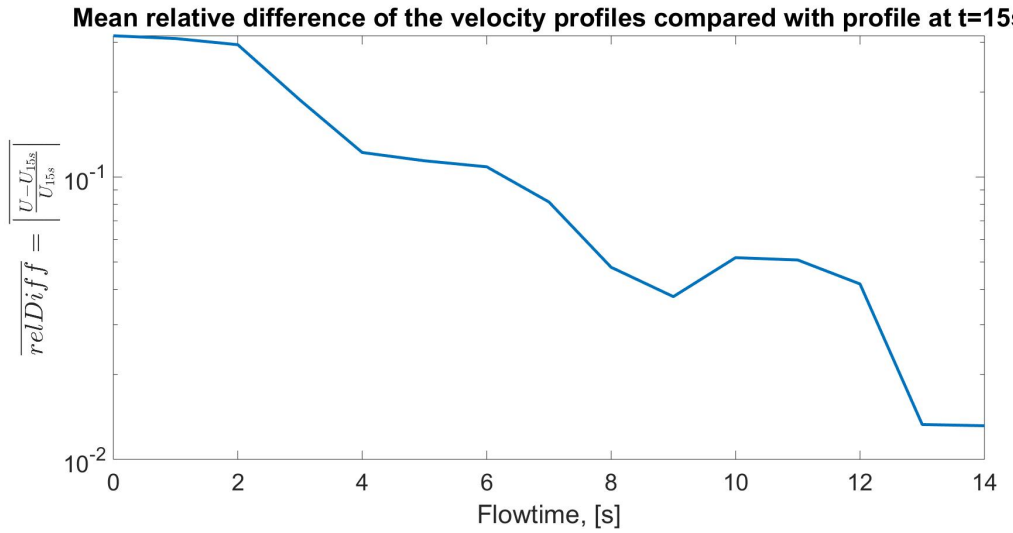

Figure 4.9: Plot of the mean relative difference between the velocity profile at several flow time instants and the velocity profile at a flow time of 15s.

represent the spatial variation measured in the channel in the lab, as the velocity profile was measured at several downstream and spanwise positions. The CFD-simulation was unfortunately not able to predict the strong shear present near the free-surface in the lab, but the CFD-model yields an adequately accurate prediction of the velocity profile for $\frac{z}{h} < 0.9$. Why the CFD-model fails to predict this strong shear near the free-surface may be explained by the following:

- The inlet velocity profile is not entirely uniform.
- Errors introduced by the model of the honeycomb.
- Errors in the screen shape. Including errors made when measuring the shape, spanwise variations of the shape of the screen in the lab, and deformation of the screen due to flow-induced drag when running the experiments in the lab.

The model of the honeycomb used in the CFD-model may not be the most realistic, but it was decided to stick with this model due to the lack of a better option. However, the spatially averaged velocity profile resulting from the CFD-simulations corresponds well with the measured velocity profile in most parts of the channel, proving that the CFD-model is an adequately accurate representation of the flow that would occur in real life.

All velocity profiles resulting from the simulations of the open channel model that will be presented in this thesis have been spatially averaged. The spatial average has been taken over the region spanning from 20-38cm downstream of the screen at the flow time of 15s. The loss factors given in table 4.3, for the screen and honeycomb, have been used for all cases of the open channel model in which results will be presented in this thesis. The inlet velocity and water depth used to generate the results will be $U = 0.117\frac{\mathrm{m}}{\mathrm{s}}$ and $h = 0.08\mathrm{m}$, unless something else has been specified.

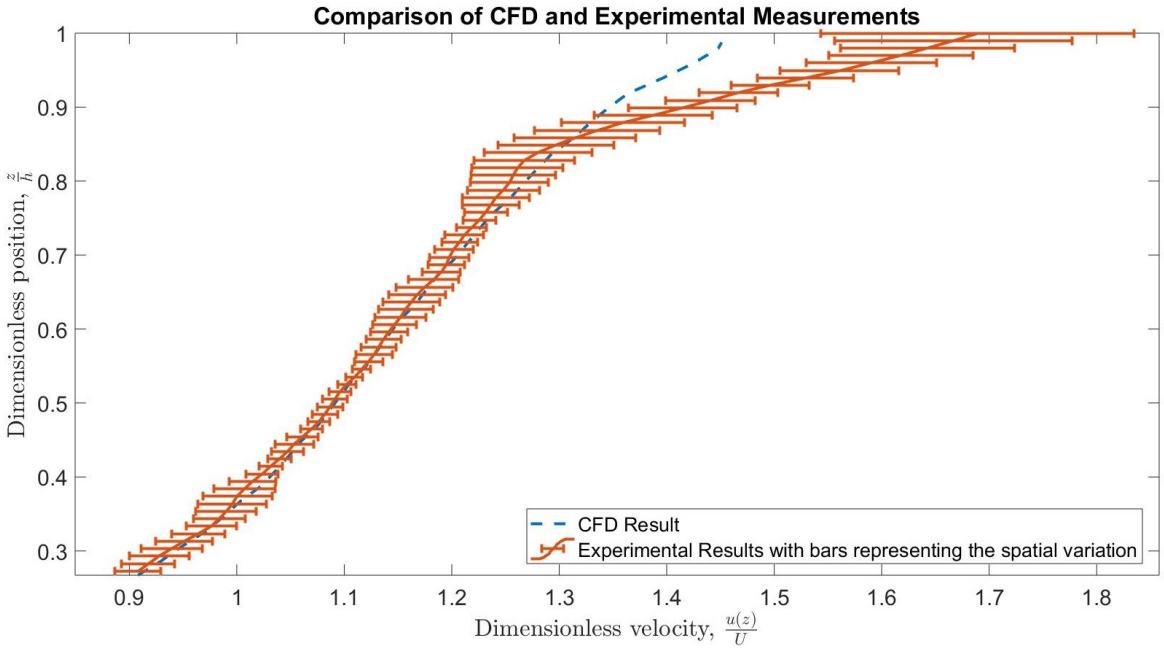

Figure 4.10: A plot comparing the velocity profile measured in the lab, including bars that represent the spatial variation in the measurements, and the spatially averaged velocity profile resulting from the CFD-calculation. Both profiles are normalized by the mean velocity, U.

4.3 Effect of Changing Screen Curvature

Investigating how the flow is affected by varying the screen curvature is one of the research objectives of this thesis, see chapter 1.2. This objective was addressed by investigating the effect of gradually reducing the radius of curvature for an initially straight screen mounted at a given angle. Two different screen shapes may be produced when the radius of curvature is

reduced, one that appears convex and one that appears concave to the flow. Both cases were investigated to analyze how the flow was affected by such a change in the screen curvature. Figure 4.11 and 4.12 illustrate the screen shapes that were investigated in this analysis. These screens were constructed by starting with a straight screen defined by the two endpoints of the screen in the CFD-model of the lab set-up, see figure 4.6. This results in an angle of 54° between the streamwise direction and the normal vector of the screen. The screens produced by reducing the radius of curvature were constructed by assuming that the screen was a part of a circular arc stretching between the endpoints of the screen in the lab, in which the radius of this circle was gradually reduced to produce screens with increasing curvature.

A case was constructed for each of the 13 different screen shapes given in figure 4.11 and 4.12, both the convex and concave screen shapes. The inlet velocity and water depth was equal for all cases studied in this section, and was set to $U_{in} = 0.117\frac{\mathrm{m}}{\mathrm{s}}$ and $h = 0.08\mathrm{m}$. The CFD-simulations were run until a flow time of 15 seconds, the same as for the lab case used for validation. From each of these cases, a spatially averaged velocity profile was calculated, taking the spatial average spanning over an 18cm streamwise region, stretching from 20-38cm downstream of the screen. In addition to these cases, two additional cases with straight screens were constructed. These cases were constructed to analyze how the downstream velocity profile is affected by a change in the angle between the screen normal vector and the streamwise direction. Three straight screens are illustrated in figure 4.13, in which the screen whose normal vector has an angle of 54° with respect to the streamwise direction is the same as the straight screen given with the gradually more curved screens in figure 4.11 and 4.12.

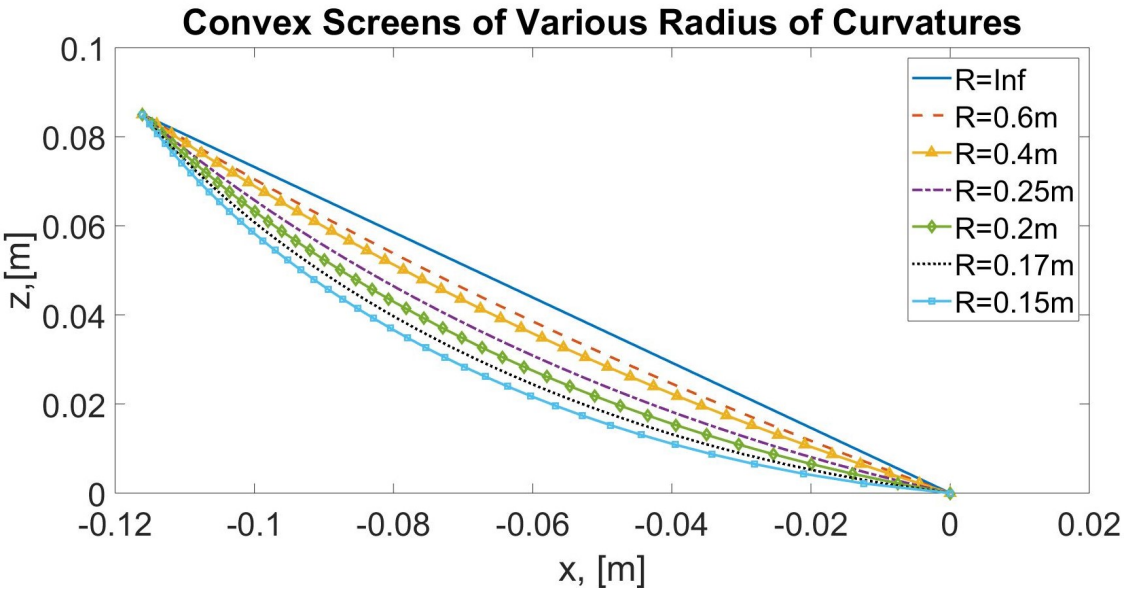

Figure 4.11: Illustration of the convex screens used to investigate the effect of changing the screen curvature.

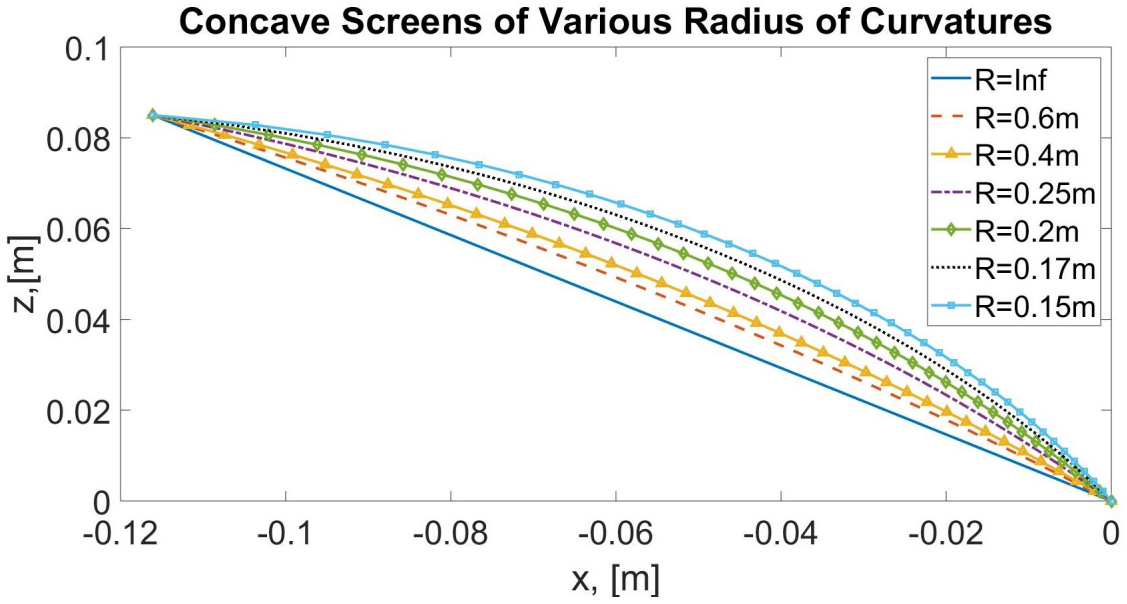

Figure 4.12: Illustration of the concave screens used to investigate the effect of changing the screen curvature.

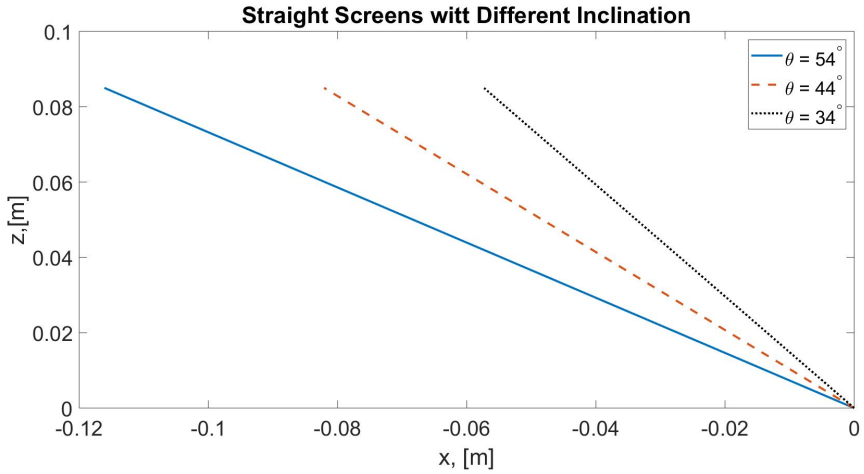

Figure 4.13: The three different straight screens that were tested to investigate the effect of varying the angle, θ, between the screen normal vector and the streamwise direction.

4.3.1 Results for the Convex Screens

A comparison of the velocity profiles resulting from the CFD-simulations using each of the convex screen shapes given in figure 4.11 can be seen in figure 4.14.

The velocity profiles in figure 4.14 have been normalized by the mean velocity in the channel, U. When comparing the velocity profiles in the center part of the channel, i.e. from $\frac{z}{h}$ equal to ~ 0.3 to ~ 0.9, one can see that the mean velocity in this region decreases with increasing radius of curvature of the convex screen. The velocity profile gets gradually more curved, making the velocity profile more concave, when the radius of curvature of the screen is reduced. Another remark is that the shear near the free-surface, i.e. for $\frac{z}{h} > 0.9$, increases with increasing radius of curvature. To summarize these results:

1. Center part of the channel: Decreasing the radius of curvature increases the mean velocity and the curvature of the velocity profile, making it more concave.

2. Near the free-surface: The shear near the free-surface increases with increasing radius of curvature.

4.3.2 Results for the Concave Screens

A comparison of the velocity profiles resulting from the CFD-simulations using each of the concave screen shapes can be seen in figure 4.15.

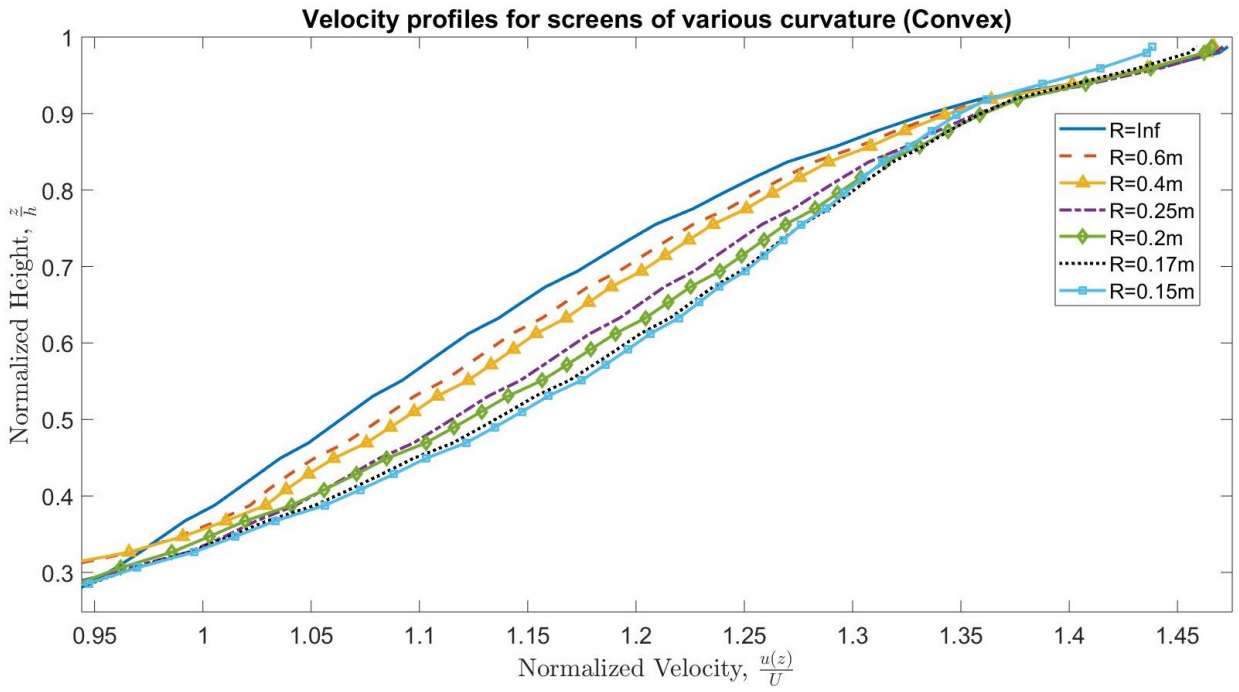

Figure 4.14: Comparison of the spatially averaged velocity profiles resulting from each of the convex screens given in figure 4.11. The velocity profiles have been normalized by the mean velocity in the channel, U.

From the plot in figure 4.15 it can be seen that the curvature of the produced velocity profile increases, making the velocity profile more convex, with a decreasing radius of curvature of the screen. Similar to the convex screens, which produced concave velocity profiles, as seen in figure 4.14. The relative change in the velocity profile when reducing the radius of curvature is less for the concave screens than the convex screens, which can be seen when comparing figure 4.14 and 4.15.

The increasingly more convex velocity profile results in a shear that gradually increases in the vertical direction, z-direction, of the channel when the radius of curvature is reduced for the concave screens. This results in an increase in the shear in the region close to the free-surface when reducing the radius of curvature. So, to summarize:

- Decreasing the radius of curvature of a concave screen will increase the curvature of the produced velocity profile, making it more convex. The shear near the free-surface increases with decreasing radius of curvature of the concave screen.

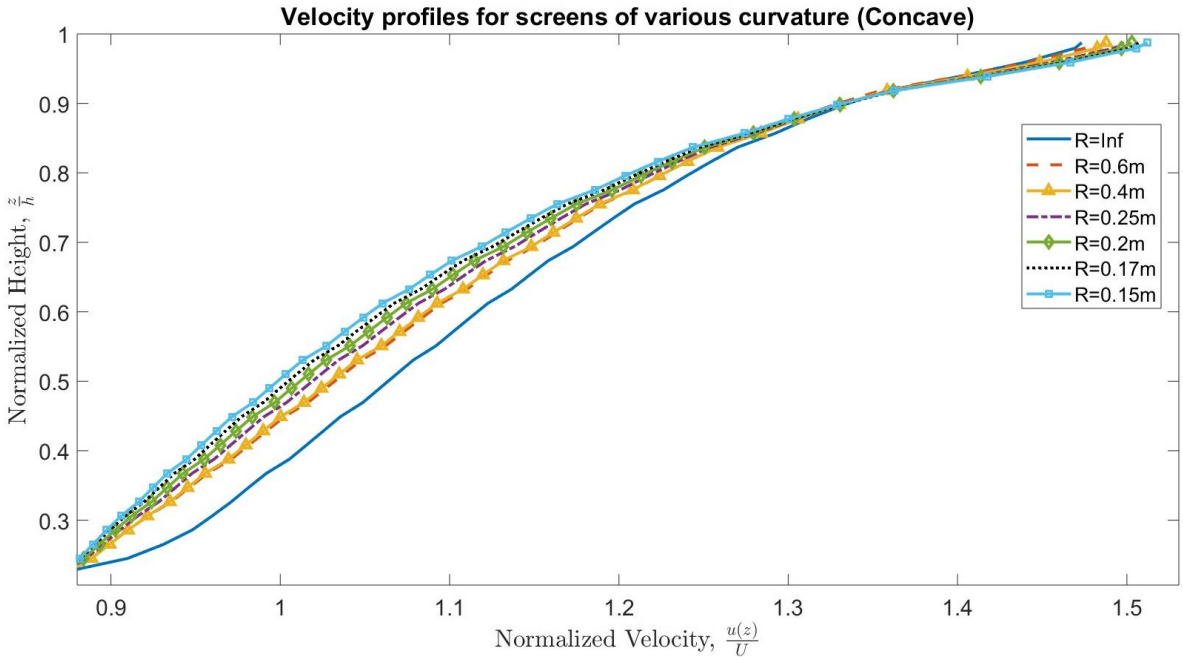

Figure 4.15: Comparison of the spatially averaged velocity profiles resulting from each of the concave screens given in figure 4.12. The velocity profiles have been normalized by the mean velocity in the channel, U.

4.3.3 Results for Straight Screens Mounted at Different Angles

As previously mentioned, it was decided to have a look at the effect of changing the angle between the screen normal vector and the streamwise direction that straight screens have on the velocity profile downstream of the screens. Three CFD-cases with straight screens mounted at three different angles, see figure 4.13, were constructed and the spatially averaged velocity profiles resulting from the CFD-simulations of these cases can be seen in figure 4.16.

The spatially averaged velocity profiles given in figure 4.16 show that the deviation from uniform flow decrease with a decreasing angle between the screen normal vector and the streamwise direction, θ. This is an intuitive result as the streamlines are being deflected in the direction of the normal vector of the screen. Furthermore, as seen in figure 4.16, the straight screen produces an almost uniform shear in the center part of the channel, and this shear increases with an increasing θ. Another effect that can be deduced from this plot is that the thickness of the strong shear layer at the bottom of the channel increases with increasing θ, this is probably due to the effect of the more significant streamline deflection

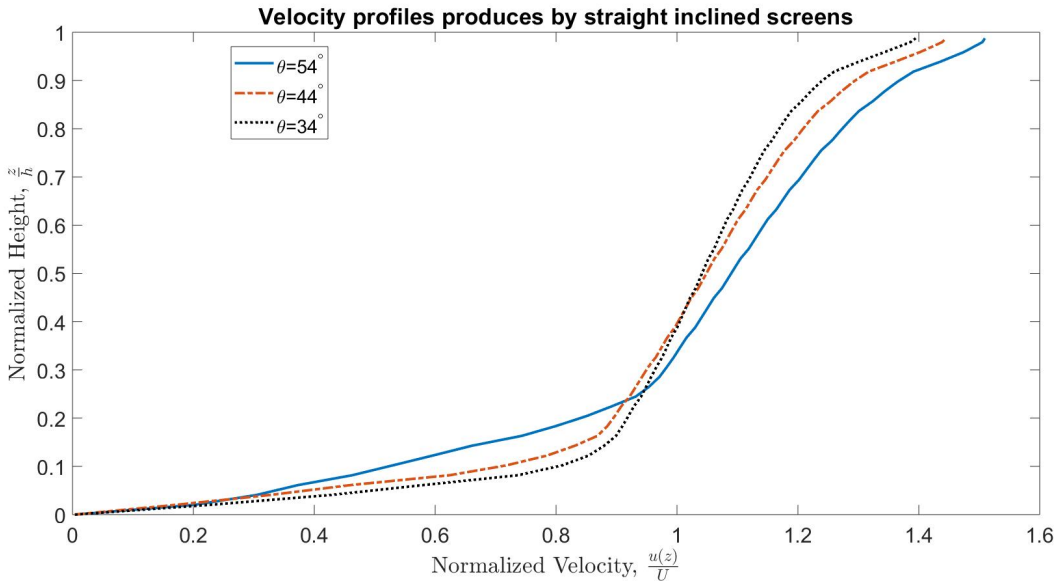

Figure 4.16: Plot of the normalized velocity profiles resulting from the CFD-model of a straight screen mounted at three different angles. The angle θ is defined as the angle between the screen normal vector and the streamwise direction.

that occurs when θ increases. I.e. decreasing θ will cause a decrease in the deflection of the streamlines, which again results in a thinner strong shear layer at the bottom of the channel. The reason for calling it a strong shear region is that the effect observed near the bottom of the channel is caused by both a viscous boundary layer and the streamline deflection caused by the screen, where the latter effect is assumed to be dominating.

Another observation made from the plot in figure 4.16 is that the shear parameter, β, near the free-surface increases with decreasing θ, although the change is fairly moderate. The mean shear parameter for the region near the free-surface, i.e. $0.92 \leq \frac{z}{h} \leq 1$, for each of the profiles in figure 4.16 is given in table 4.4. This table includes the shear parameter near the free-surface for a straight screen as well. The effect of an increasing shear in the region near the free-surface with a decreasing θ may be explained by the fact that the flow obstruction as perceived by the flow is greater for a more inclined screen. This increased flow resistance will result in an increased momentum loss and restrict the acceleration of the flow in the region near the free-surface more than less inclined screens.

Table 4.4: Mean shear parameter, β, near the free-surface for the straight screens with different inclination.

θ	54°	44°	34°	0°
β	1.71	1.85	1.95	1.99

4.4 Effect of Changing Inlet Velocity

Some additional cases using the CFD-model of the lab were simulated to test the effect the inlet velocity has on the resulting downstream velocity profile. The three inlet velocities investigated in this analysis were $0.08\frac{\mathrm{m}}{\mathrm{s}}$, $0.12\frac{\mathrm{m}}{\mathrm{s}}$, and $0.15\frac{\mathrm{m}}{\mathrm{s}}$. The normalized spatially averaged velocity profiles downstream of the screen resulting from the CFD-simulations can be seen in figure 4.17.

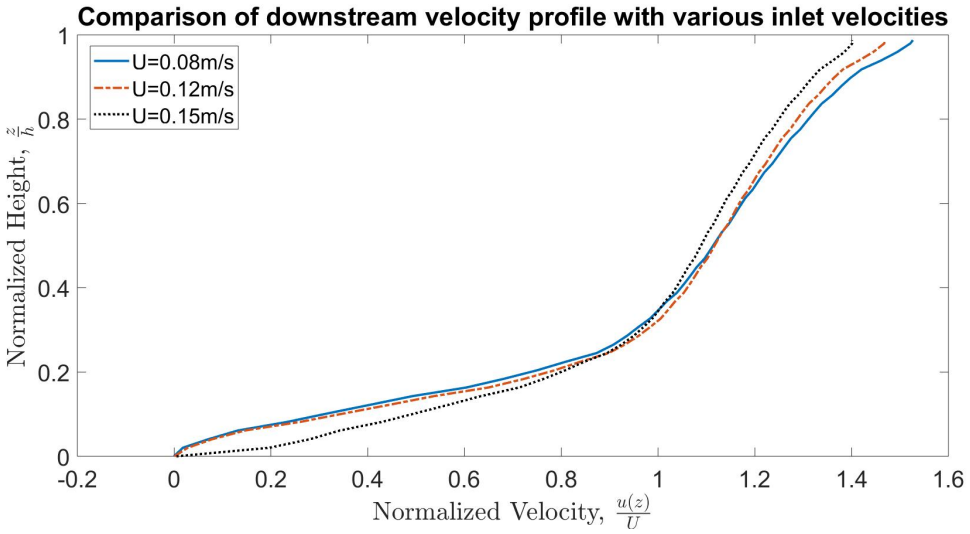

Figure 4.17: Plot of the normalized spatially averaged velocity profiles resulting from three different inlet velocities using the CFD-model of the lab set-up.

From the plot of the resulting velocity profiles for the different inlet velocities in figure 4.17 it can clearly be seen that the shear of the velocity profiles gradually decreases when the inlet velocity is increased. This results in velocity profiles that become more similar to the uniform profile at the inlet when increasing the inlet velocity. This suggests that the screens ability to transform the velocity profile is reduced when the inlet velocity, or mean velocity of the flow, is increased. The same effect was observed in figure 4.5 in chapter

4.1, where a screen designed to produce a uniformly sheared outlet velocity profile with a shear parameter, β, of 0.25 was tested at various inlet velocities. The shear parameter for the theoretically predicted velocity profile and the velocity profile resulting from the CFD-simulations increased for velocities below the design velocity and decreased for inlet velocities above the design value, see table 4.2. This suggests that flows with higher inertia require a more significant flow obstruction for the velocity profile to be transformed at the same rate as a flow of lower inertia.

The flows ability to penetrate the screen at the bottom of the channel increases with increasing inlet velocity. This can clearly be observed when comparing the case with an inlet velocity of $0.15\frac{\mathrm{m}}{\mathrm{s}}$ with the other cases, as the shear in the immediate vicinity of the wall is much stronger, suggesting a smaller deflection of the streamlines near the bottom for this case.

4.5 Effect of Changing Water Depth

The CFD-model of the lab set-up was used to study the effect of varying the water depth of a channel while keeping the screen parameters, inlet velocity, and screen shape constant. Three cases, each with different water depths, were simulated to investigate the effect water depth has on the resulting velocity profile. The three water depths tested were 0.08m, 0.07m, and 0.06m.

The normalized velocity profiles for each water depth were again spatially averaged, spanning the same region as for the other cases, i.e. the region from 20-38cm downstream of the screen at a flow time of 15s, and the result may be seen in figure 4.18. Surprisingly enough, it appears that changing the water depth only has a small, almost negligible effect, on the normalized velocity profile. The plots of the velocity profiles roughly coincide for the respective water depths. Another surprising effect is that the thickness of the strong shear region at the bottom of the channel covers the same normalized region, i.e. the physical thickness of it shrinks when the water depth is decreased. This suggests that it is not a viscous boundary layer that creates this strong shear region, as the normalized thickness of a viscous boundary layer would most likely increase with decreasing water depth.

The fact that the normalized velocity profile does not change when changing the water depth can probably not be generalized for all screen shapes. The explanation for this is that a change of the water depth in a channel with a screen whose shape varies a lot in different

regions would most likely result in a change in the normalized velocity profile downstream of that screen.

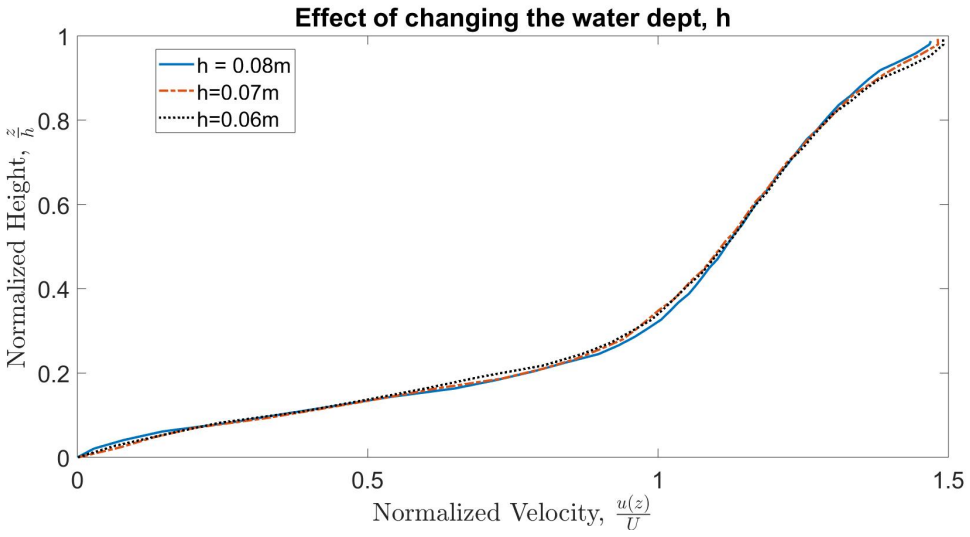

Figure 4.18: Spatially averaged velocity profiles downstream of the screen normalized by the mean velocity, U, and water depth, h, for the respective cases.

4.6 Discussion of the Results

This chapter will give a discussion of the results and attempt to explain why these changes of the velocity profile occur for the different cases. Furthermore, a comparison between the theoretically predicted velocity profile and the velocity profile resulting from the CFD-simulations will be given for some of the cases. This chapter will also include a discussion about vortex production by the different screen shapes, and a suggestion for improving the present model.

4.6.1 General Remarks

The results from the increasingly convex and concave screens are somewhat intuitive, considering that the streamlines are deflected in the direction of the normal vector of the screen. Figure 4.19 illustrates why this result is intuitive, showing how the streamlines are deflected over convex and concave screens. The streamlines are deflected similarly as light rays in convex and concave lenses.

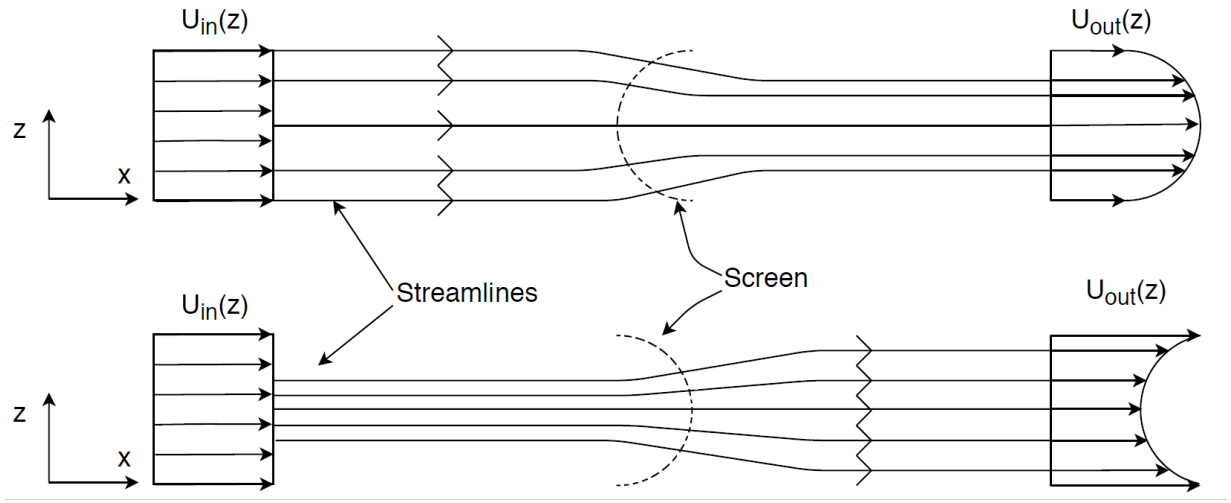

Figure 4.19: Illustration of how streamlines are deflected over convex and concave screens.

In the cases tested in chapter 4.3.1 and 4.3.2, the screens are not only curved, but they are also tilted. A study on how the flow was affected when a straight screen was mounted at different angles was conducted in chapter 4.3.3. The results from chapter 4.3.3 showed that more inclined screens produced greater shears, which again is an intuitive result as streamlines are deflected in the direction of the normal angle of the screen. A not so trivial result was discovered for the shear near the free-surface, in which the shear in the region close to the free-surface increased when the inclination of the screen decreased. An effect that presumably occurs as the resistance introduced to the flow by the screen in the region near the free-surface increases with increasing inclination of the screen, as the blockage perceived by the flow increases.

The investigation of the shear in the region near the free-surface of the convex screens showed that the shear decreased with decreasing radius of curvature. The reason why this is happening is not so straight forward, as two counteracting effects occur when reducing the radius of curvature of the screen. Firstly, the decreased radius of curvature will produce a more concave velocity profile, which tends to decrease the shear in the region close to the free-surface. Whereas the second effect will tend to increase the free-surface shear as the screen becomes increasingly vertical, i.e. θ decreases, in the region close to the free-surface. This effect was observed for the straight screens mounted at various angles. However, the first effect seems to dominate in these cases, as the shear in the region near the free-surface decreases with decreasing radius of curvature. From table 4.4 it can be seen that changing

the inclination of the screen has a relatively small effect on the shear near the free-surface.

The situation is completely turned around for the concave screens, where the screen becomes more and more inclined near the free-surface as the radius of curvature decreases. The increasing inclination of the screen near the free-surface tends to decelerate the flow in this region, while the decreasing radius of curvature of the concave screen tends to accelerate it. Again, the effect of the increased curvature of the screen dominates, such that the shear in the region close to the free-surface increases with decreasing radius of curvature for the concave screens.

From the simulations of the lab set-up at different inlet velocities, it was discovered that increasing the inlet velocity resulted in a smaller change of the velocity profile. This result agrees with the predictions by the linearized theory for the closed channel cases tested in chapter 4.1, where the results are shown in figure 4.5. An explanation for this may be that the increased inlet velocity increases the inertia of the flow. This increase in the inertia of the flow would then require a greater flow resistance than a flow of lower inertia to produce the same normalized downstream velocity profile. The flow resistance is indeed a function of the fluid velocity, see relations for the pressure drop coefficient K (equation (2.3), (2.5), (2.20),and (2.21)), but the effect of the increased flow inertia dominates for the cases tested in chapter 4.4.

The results of the cases testing the effect of varying the depth of the channel proved to give the most surprising result, as the normalized velocity profile was unchanged despite the changes to the water depth in the channel. This effect is tougher to explain and would need to be investigated further as this may be a coincidence for these cases. Screens that vary more in shape, e.g. consisting of both concave and convex regions, are not expected to show the same behaviour. However, this needs to be investigated further before drawing any conclusions.

4.6.2 Comparison to Theoretical Estimates

The velocity profile resulting from a given screen shape, screen parameters, and inlet conditions may be predicted by solving equation (2.9), i.e. the linearized solution by Elder [7], using the MATLAB function given in appendix A.2. This solution only includes first-order effects, such that the solution predicted by this equation becomes increasingly invalid for increasing screen curvatures, which results in increasing changes in the velocity profile over

the screen.

Figure 4.20 presents a comparison between the velocity profile predicted by equation (2.9) and the velocity profile resulting from the CFD-simulation of four of the open channel flow cases. The plots for the straight screen mounted at $\theta = 56°$ shows a decent agreement between the normalized velocity profiles. This shape introduces the least changes to the velocity profile over the screen of those present in figure 4.20, such that it may be justified that the assumptions behind the linearized solution are not seriously violated for this screen shape. The remaining plots in figure 4.20 do not show an excellent agreement between CFD-results and the theoretically predicted velocity profile. The linearized theory is only to able predict the shear in some regions for these three cases, e.g. the center region for the concave screen with a radius of curvature of 0.25m. The linearized solution does unfortunately not provide an adequately accurate prediction of the velocity profiles, except maybe the case with the straight screen mounted at $\theta = 56°$. These erroneous velocity predictions are presumably due to violation of the assumptions in which the linearized solution is derived upon. Another remark is that the linearized theory is based upon the assumption that viscous effects only are present in the near vicinity of the screen, hence it will not be able to predict any viscous effects introduced by the bottom wall. This shows that the linearized solution, relating the screen shape to up- and downstream flow conditions, is only applicable for a limited range of cases, which was one of the motivations for this thesis.

4.6.3 Vortex Generation

A small discussion on the vortex generation will be presented, due to some interesting trends between the screen shape and vortex generation in the simulations.

The vortex generation reduces with a reduced inclination for the straight screens. This is probably a result of the reduced streamline deflection when reducing the inclination of the screen. The surprising result here is the rate at which the vortex generation is reduced. The effect of vortex generation is clearly visible in the velocity contour plot for the screen mounted at $\theta = 54°$, while no vortices are apparent in the case where the screen is mounted at an angle of $\theta = 44°$. This result suggests that the vortex generation caused by the screen is an effect that is very sensitive to the shape of the screen. These contour plots can be found in appendix B.3.

This sensitivity is also observed when making the screen shapes slightly more curved,

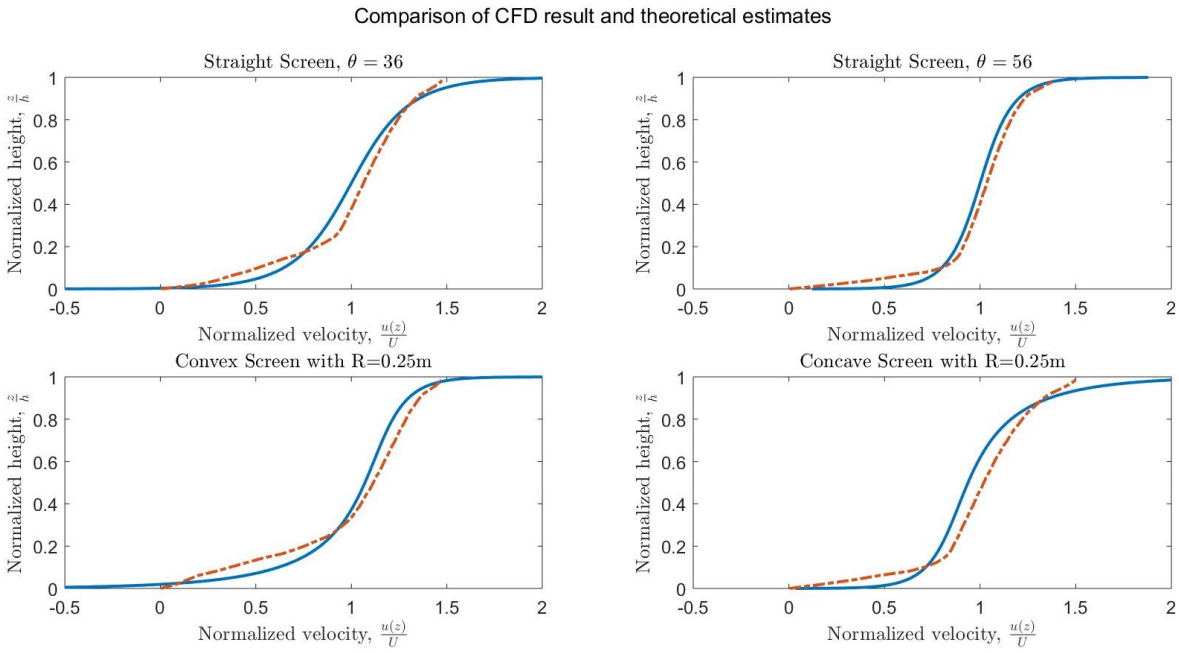

Figure 4.20: Comparison between the velocity profile predicted by the linearized theory using equation (2.9) and the velocity profile resulting from the CFD-simulations. ——, equation (2.9); — – —, CFD-results.

especially more concave. The effect of the vortices are eliminated by reducing the radius of curvature to $R = 0.4$m for the concave cases, while the radius of curvature has to be reduced to about $R = 0.2$m before the effect of the vortices disappears for the convex screens. This indicates that the vortex generation effect is much more sensitive to changes making the screen more concave than convex. Furthermore, the effect of the vortices seems to increase with increasing inlet velocity, probably due to the increased flow instability that occurs at higher Reynolds number. Contour plots from several of the cases investigated in this thesis can be found in appendix B.

It should be noted that a better modelling of the flow straightening effect of honeycombs may reduce, and even eliminate, the effect of the vortices discussed here.

4.6.4 Effect of Surface Tension

The effect of surface tension has been neglected from the cases simulated in this thesis, as it was assumed negligible. A simulation using the model of the lab set-up, including the CSS

surface tension model was simulated to investigate the effect that surface tension had on the downstream velocity profile. The velocity profile resulting from this simulation is shown in figure 4.21, where it is compared to the result from a simulation of the same model where surface tension has been neglected. A plot of the relative difference between the velocity profiles resulting from these simulations is also included. This figure clearly illustrates that surface tension has a minor effect on the velocity profile, which supports the negligence of surface tension in the other cases simulated in this thesis.

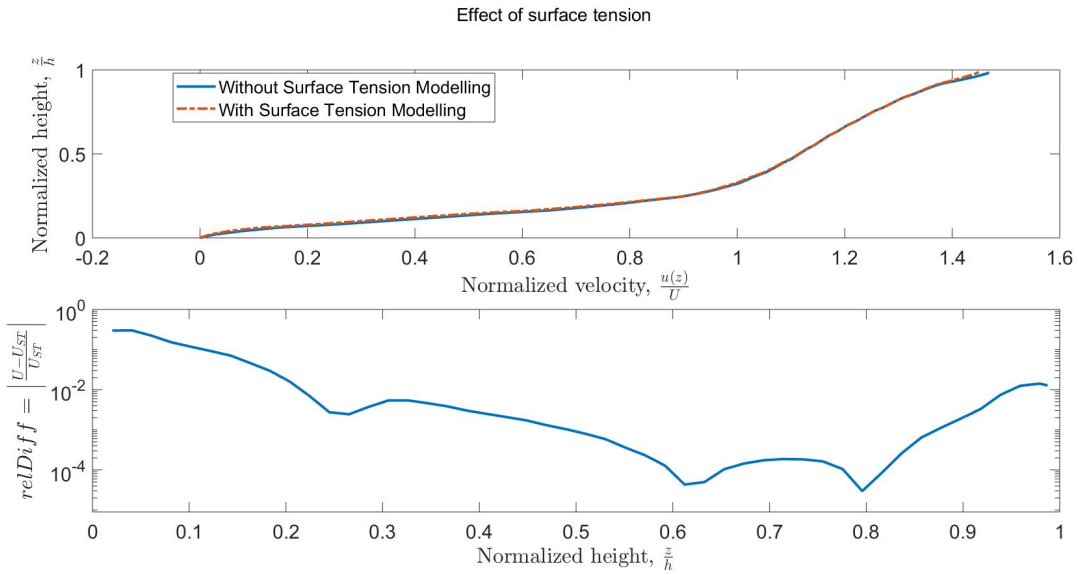

Figure 4.21: Plot comparing the velocity profile resulting from CFD-simulations of the lab set-up both with and without including the effects of surface tension. The bottom plot shows the relative difference between the profiles.

4.6.5 A Suggestion for Improvement

The CFD-model presented in this thesis proved to give adequately accurate results when compared with experimental measurements in chapter 4.2. An almost perfect agreement between the velocity profiles was observed in the center part of the channel, but the CFD-model was unfortunately not able to predict the strong shear experienced in the region close to the free-surface. The reason for this may be errors introduced when assuming the inlet profile to be uniform, differences in the screen shapes in the CFD-model and in the lab, or errors introduced in the modelling of the honeycomb.

The honeycomb has been modelled by a straight porous region, where the flow resistance has been approximated using the same equation and procedure as for the screen, i.e. equation (2.21). This relation was used as no other relation for the pressure drop over a honeycomb was found. The pressure drop over the honeycomb was then calculated using the parameters of screen 2 in table 3.1 and setting the porosity to 0.875, which is the same as the porosity of the honeycomb in the lab. The loss factors used for the honeycomb are given in table 4.3. This is probably not a very accurate way to model honeycombs, and the way to model the loss should be corrected as soon as a better relation for the pressure drop is found. The PMM may not be the best way to model honeycombs either due to the large aperture. However, as the objective of this thesis was to model the effects of screens and not the effects introduced by adding a honeycomb, it was assumed that this was an adequate way to model the honeycomb for the purposes of this thesis.

Chapter 5

Conclusion

The main objective of this master's thesis was to generate a CFD-model that accurately simulated flows passing through curved screens. Initially, it was desired to construct a model that resolved all the flow structures within the screen, by using either a quasi-2D model or a model allowing spanwise flow structures larger than the periodic screen length's width. This proved to be very computationally intensive, and it was therefore decided that the flow obstruction introduced by a screen had to be modelled. Another reason for this choice was that it was desired that the CFD-model could be used as an efficient tool to test different screen configurations.

The porous media model (PMM) was chosen to model the flow resistance introduced by a physical screen. A reason for this choice was that Teitel [24] proved that this model gave accurate results when simulating flows passing through straight screens. The loss factors used in the PMM was determined using the procedure given in chapter 3.1.2. The flow straightening effect introduced by a honeycomb was also modelled by the PMM as described in chapter 3.1.2. Two models using the PMM was presented in chapter 3.2, one closed and one open channel flow model. The results of the mesh independence tests given in chapter 3.4 were used to decide the cell size of the meshes used to produce the results in this thesis, to ensure that the presented solutions are mesh independent.

The closed channel model was used to verify that the PMM could accurately predict the flow obstruction introduced by a physical screen, with chapter 4.1 verifying this. Figure 4.3 and 4.5 show that the CFD-model accurately predicts the velocity profile downstream of the screen when compared with theoretical estimates obtained using Elder's [7] linearized relation given in equation (2.9). The comparison given in figure 4.5 proves that the screen

shape given by the iterative solution of equation (2.9) performs better at producing the desired velocity profile than the relation given by Dunn and Tavoularis [6].

A case modelling the set-up of the lab in the fluid mechanics building at NTNU, see figure 1.1, was constructed. The result from the CFD-simulation using this model was compared to experimental measurements provided by PhD Candidate Benjamin Smeltzer to validate the CFD-model. This comparison can be seen in figure 4.10, which shows that the CFD-model accurately predicted the velocity profile in the majority of the channel. The CFD-model was unfortunately not able to predict the strong shear measured in the region close to the free-surface in the lab, and there may be several reasons for this. It is believed that errors introduced by assuming a uniform velocity profile at the inlet and errors introduced by the model of the honeycomb, may explain a significant part of why the CFD-model fails to predict this strong shear near the free-surface. Nevertheless, this comparison validates that the CFD-model provides an adequately accurate prediction of the velocity profile resulting from flows passing through curved screens.

After the CFD-model had been sufficiently verified and validated, several cases were constructed to analyze how the flow was affected by varying:

- Screen shape/curvature.
- Inlet velocity.
- Water depth.

The effect of the screen shape was investigated by decreasing the radius of curvature of an initially straight screen mounted at a certain angle with respect to the bottom wall. Reducing the radius of curvature for a straight screen may produce screens that are perceived as either concave or convex by the flow. Both cases were investigated, in addition to the effect of changing the angle between the screen normal vector and the streamwise direction for straight screens. The results of these cases were given in chapter 4.3, and the velocity profile downstream of the screens for these cases showed that:

- The resulting velocity profile becomes increasingly concave, and the shear near the free-surface is reduced when reducing the radius of curvature of a convex screen. See figure 4.14.

- The resulting velocity profile becomes increasingly convex, and the shear near the free-surface is increased when reducing the radius of curvature of a concave screen. See figure 4.15.

- The mean shear of the downstream velocity profile increases and the shear near the free-surface decreases when increasing the angle between the screen normal vector and the streamwise direction for straight screens. See figure 4.16.

The results from the cases investigating the effects of varying the inlet velocity and water depth were given in chapter 4.4 and 4.5. The shape of the screen tested in these cases was the same as the shape of the screen in the lab in the fluid mechanics building at NTNU, which is given in figure 4.6. These results showed that:

- The rate at which the velocity profile is transformed is reduced when the inlet velocity increases. See figure 4.17. This may be explained by the fact that a greater flow resistance is needed to deflect the flow at the same rate when the inertia of the flow is increased by increasing the inlet velocity.

- A change in the water depth did, surprisingly, not have any effect on the normalized velocity profiles downstream of the screen. See figure 4.18.

The effect observed for the case where the water depth was reduced can probably not be generalized for all screen shapes. The reason for this is that reducing the water depth for a screen whose shape has both convex and concave regions will most likely result in a change in the normalized downstream velocity profile. Nevertheless, the observations made for the modifications of screen shape and inlet velocity are believed to be general.

A comparison between the velocity profiles predicted by the linearized relation in equation (2.9) and the velocity profiles resulting from the CFD-simulations showed an almost perfect agreement for the closed channel flow cases investigated. The shapes of the screens were only moderately curved such that the assumptions for the linearized theory were most likely not heavily violated in these cases. The linearized theory did unfortunately not predict the velocity profile accurately for the more curved screens tested in the open channel cases. This is probably explained by two effects:

1. The curvature of the screens violate the assumption that the flow problem may be linearized, something which equation (2.9) relies upon.

2. The linearized relation does not predict the effects of viscous boundary layers, as the effect of viscosity is neglected everywhere except in the near vicinity of the screen.

Bibliography

[1] B. J. Bailey et al. "Airflow resistance of greenhouse ventilators with and without insect screens". In: *Biosystems Engineering* 86.2 (2003), pp. 217–229.

[2] E. Brundrett. "Prediction of pressure drop for incompressible flow through screens". In: *Journal of fluids engineering* 115.2 (1993), pp. 239–242.

[3] I. P. Castro. "Some problems concerning the production of a linear shear flow using curved wire-gauze screens". In: *Journal of Fluid Mechanics* 76.4 (1976), pp. 689–709.

[4] Yunus A. Cengel and John M. Cimbala. Third. McGraw-Hill, 2014. Chap. 13, Open Channel Flows, pp. 726–728.

[5] G. Davis. "Non-uniform flow through wire screens". PhD thesis. Ph. D. dissertation, University of Cambridge, Cambridge, MA, 1957.

[6] W. Dunn and S. Tavoularis. "The use of curved screens for generating uniform shear at low Reynolds numbers". In: *Experiments in fluids* 42.2 (2007), pp. 281–290.

[7] J. W. Elder. "Steady flow through non-uniform gauzes of arbitrary shape". In: *Journal of Fluid Mechanics* 5.3 (1959), pp. 355–368.

[8] AN Fluent. *18.2, ANSYS Fluent Meshing User's Guide*. 2017. Chap. 22.2.2, Determining Volume Mesh Quality, pp. 327–335.

[9] AN Fluent. *18.2, Theory Guide, ANSYS Inc.* 2017. Chap. 6.2.3 Porous Media Conditions, pp. 263–289.

[10] AN Fluent. *18.2, Theory Guide, ANSYS Inc.* 2017. Chap. 17.3 Volume of Fluid (VOF) Model Theory, pp. 512–545.

[11] AN Fluent. *18.2, Theory Guide, ANSYS Inc.* 2017. Chap. 6.3 Boundary conditions, pp. 303–408.

[12] AN Fluent. *18.2, Theory Guide, ANSYS Inc.* 2017. Chap. 28.15 Monitoring Solution Convergence, pp. 1634–1645.

[13] S. I. Green et al. "Simulation of the flow through woven fabrics". In: *Computers & Fluids* 37.9 (2008), pp. 1148–1156.

[14] J. Groth and A. V. Johansson. "Turbulence reduction by screens". In: *Journal of Fluid Mechanics* 197 (1988), pp. 139–155.

[15] U. Karnik and S. Tavoularis. "Generation and manipulation of uniform shear with the use of screens". In: *Experiments in fluids* 5.4 (1987), pp. 247–254.

[16] D. R. Kotansky. "The use of honeycomb for shear flow generation." In: *AIAA Journal* 4.8 (1966), pp. 1490–1491.

[17] P. K. Kundu and I. M. Cohenand D. R. Dowling. Sixth. Elsevier, 2012. Chap. 11, Instability, pp. 533–594.

[18] Y. L. Lau and W. D. Baines. "Flow of stratified fluid through curved screens". In: *Journal of Fluid Mechanics* 33.4 (1968), pp. 721–738.

[19] J. L. Livesey and E. M. Laws. "Flow through non-uniform gauze screens". In: *Journal of Fluid Mechanics* 59.4 (1973), pp. 737–743.

[20] J. L. Livesey and J. T. Turner. "The generation of symmetrical duct velocity profiles of high uniform shear". In: *Journal of Fluid Mechanics* 20.2 (1964), pp. 201–208.

[21] D. J. Maull. "The wake characteristics of a bluff body in a shear flow". In: *AGARD Conf. Proceed.* 48. 1969, pp. 16–1.

[22] J. H. McCarthy. "Steady flow past non-uniform wire grids". In: *Journal of Fluid Mechanics* 19.4 (1964), pp. 491–512.

[23] P. R. Owen and H. K. Zienkiewicz. "The production of uniform shear flow in a wind tunnel". In: *Journal of Fluid Mechanics* 2.6 (1957), pp. 521–531.

[24] M. Teitel. "Using computational fluid dynamics simulations to determine pressure drops on woven screens". In: *Biosystems engineering* 105.2 (2010), pp. 172–179.

[25] J. T. Turner. "A computational method for the flow through non-uniform gauzes: the general two-dimensional case". In: *Journal of Fluid Mechanics* 36.2 (1969), pp. 367–383.

[26] O. Zikanov. *Essential computational fluid dynamics*. John Wiley & Sons, 2010. Chap. 13: Conducting CFD Analysis, pp. 280–295.

[27] E. Æsøy. "Experimental study of surface waves on strongly sheared currents-Laboratory, design, building, testing, and measurements". MA thesis. NTNU, 2017.

Appendix A

Matlab Scripts

A.1 Matlab Script for the Screen Shape

```
clc
clear all
close all

%Input parameters
d = 0.00045;%Diameter/projected thickness of wires in mesh
l = 0.00159; %axis-to-axis spacing between elements
h = 0.1; %Channel height
Uin = 0.05; %Uniform inlet velocity
dx = h/1998; %Infinitesimal length
z = 0:dx:h; %Vertical vector
beta = 0.25; %Outlet shear parameter
Uout = (1+beta*(z/h-0.5)); %Normalized outlet velocity profile
u = ones(size(Uout)); % Normalized inlet profile
tol = 1e-18; %Tolerance
tol2 = 10^-12; %Tolerance

%Fluid properties
rho = 998.2; %Density
mu = 0.001003; %Dynamic viscosity


%Derived parameters
sigma = (2*d*l-d^2)/l^2; %Solidity of screen
Re = rho*Uin*d/mu; %Reynolds number
K = ((0.05+0.95*sigma)/(0.95*(1-sigma)))^2+88*sigma/Re; %Pressure drop
 coeff. (Elder/Davis)
B = 1-1/sqrt(1+K^0.5); %Deflection coeff. (Elder)

%Screen shape by Dunn & Tavoularis (2007)
f = -0.738*(z/h).^6+2.812*(z/h).^5-3.839*(z/h).^4+2.687*(z/h).^3-...
    1.224*(z/h).^2 - 0.0054*z/h;
xDT = h*((2+K-B)*beta/(K*B)*f);

%Screen shape by Elder (1959)
w = pi*z/(2*h);
E = K/(2+K-B);
fn = w.^2.*log(w) -3/2*w.^2+1/18*w.^4+7/1350*w.^6;
xElder = 4*beta*h/(E*B*pi^3)*fn;


%Iterative solution of Elder's general solution
gamma = K;
s = 0;
diff = 1; diff2=diff;
x = zeros(size(z));
count = 0;

while diff>tol && diff2>tol2
    count = count+1; %Checking iterations before convergence
    %Updating coefficients and fucntions
    E = gamma/(2+gamma-B);
```

```
    A = 1-gamma.*(1-E);
    F = (Uout-1)./E-A*(u-1)./E;
    %Calculating Fourier coefficients
    alpha = zeros(1,1000);
    for i = 1:length(alpha)
        dalpha = 0;
        dn = 1/length(F);
        for j = 1:length(F)
            dalpha = dalpha + 2*F(j)*cos(i*pi*z(j)/h)*dn;
        end
        alpha(i) = dalpha;
    end
    nx(1) = 0;
    %Calcutating the screen slope
    for i = 1:length(z)
        tan(i) = 0;
        for j = 1:length(alpha)
            tan(i) = tan(i)+alpha(j)*sin(j*pi*z(i)/h);
        end
        tan(i) = 1/B*tan(i);
    end
    %Calculating the new screen shape
    for i = 2:length(tan)
        nx(i) = nx(i-1)+dx*(tan(i)+tan(i-1))/2;
    end
    %Calculating the new value of the mean loss coefficient
    theta = atan(tan);
    gamma_n = 0;
    dn = 1/length(theta);
    for i = 1:length(theta)
        gamma_n = gamma_n + K*cos(theta(i))^2*dn;
    end
   gamma=gamma_n;
   if count ==1
        plot(nx,z,'LineWidth',2)
        hold on
        diff1 = 1/dx*sqrt(sum((nx-x).^2));
   end
    %Calculating the two-norms used to check for convergence
    diff2 = 1/dx*sqrt(sum((nx-x).^2));

    diff=diff2/diff1;
    %Updating screen shape
    x = nx;
end
plot(x,z,'LineWidth',2)
hold on

%Saving the discrete screen shape in text-format
delete 'CastroShape.txt'
fid = fopen('CastroShape.txt','wt');
for i = 1:length(x)
    fprintf(fid, '%20.18f\t', [1 i x(i) 0 z(i)]);
    fprintf(fid,'\n');
```

```
end
fclose(fid);


plot(xDT,z,'LineWidth',2)
plot(xElder,z, 'LineWidth',2)
legend('First iteration','Iterative solution','Dunn and
 Tavoularis','Elder','Location','Best')
```

Published with MATLAB® R2018a

A.2 Matlab Function Computing the Downstream Velocity

```
%Function that calculates the downstream velocity profile for flow
 through
%a screen assuming uniform inlet velocity of water. x and z and points
 on the
%screen, d and s the wire diamater and the spacing between the wire
%centers. h is the channel height/water depth.
function U = ElderVelocity(x,z,U,d,l,h)
n = find(z<=h); %To ensure that only the wetted part of the screen is
 considered
x = x(n);
z=z(n);
dx1 = 0.5*(z(2)-z(1));
dx2 = 0.5*(z(3:end)-z(1:end-2));
dx3 = 0.5*(z(end)-z(end-1));
dx = [dx1; dx2; dx3];
Uin = U*ones(size(z)); %Uniform inlet velocity
uin = ones(size(x));


%Fluid properties
rho = 998.2; %Density
mu = 0.001003; %Dynamic viscosity


%Derived parameters
sigma = (2*d*l-d^2)/l^2; %Solidity of mesh
Re = rho*mean(Uin)*d/mu; %Reynolds number
Re = mean(Re);
K = ((0.05+0.95*sigma)/(0.95*(1-sigma)))^2+88*sigma/Re; %Pressure-drop
 coeff. (Elder/Davis)
B = 1-1/sqrt(1+K^0.5); %Deflection coeff. (Elder)

dxdz(1) = 0;
dxdz(2:length(x)) = (x(2:end)-x(1:end-1))./(z(2:end)-z(1:end-1));
theta = atan(dxdz);
Btan = B*tan(theta);

alpha = zeros(1,1000);
%Determining the Fourier Coefficients
for i = 1:length(alpha)
    dalpha = 0;
    dn = 1/length(Btan);
    for j = 1:length(Btan)
        dalpha = dalpha + 2*Btan(j)*sin(i*pi*z(j)/z(end))*dx(j)/h;
    end
    alpha(i) = dalpha;
end

%Calculating the effective loss coefficient
gamma = 0;
for i = 1:length(dxdz)
    gamma = gamma + K*cos(atan(theta(i)))^2*dx(i)/h;
```

```
end

E = gamma/(2+gamma-B);
A = 1-gamma.*(1-E);

%Calculating the velocity profile
u = zeros(size(x));
for i = 1:length(u)
    du=0;
    for j = 1:length(alpha)
        du = du +A*(uin(i)-1) +alpha(j)*cos(pi*j*z(i)/z(end));
    end
    u(i) = (1 + E*du);
end
U=u;
```

Published with MATLAB® R2018a

Appendix B

Contour Plots

B.1 Convex Screens

Figure B.1: Velocity contour plot resulting from the convex screen with a radius of curvature of 0.6m at a flow time of 15s.

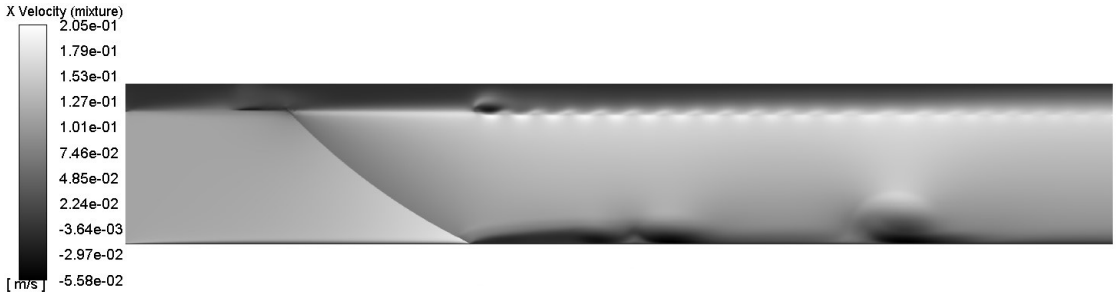

Figure B.2: Velocity contour plot resulting from the convex screen with a radius of curvature of 0.4m at a flow time of 15s.

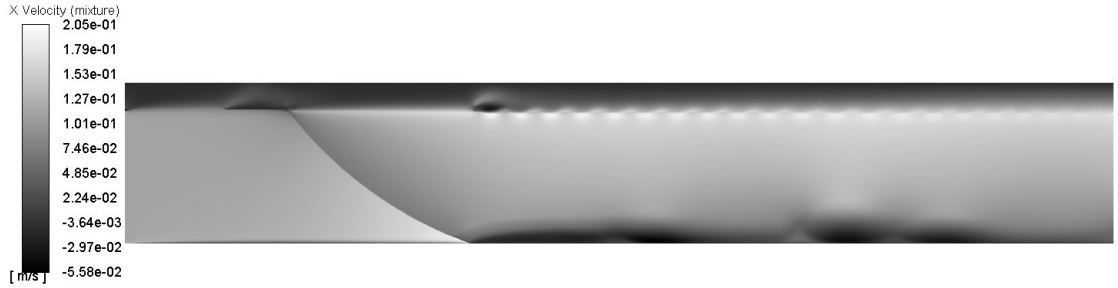

Figure B.3: Velocity contour plot resulting from the convex screen with a radius of curvature of 0.25m at a flow time of 15s.

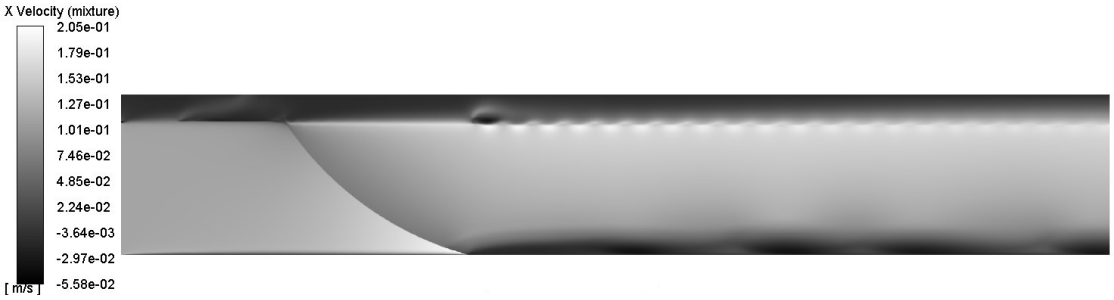

Figure B.4: Velocity contour plot resulting from the convex screen with a radius of curvature of 0.2m at a flow time of 15s.

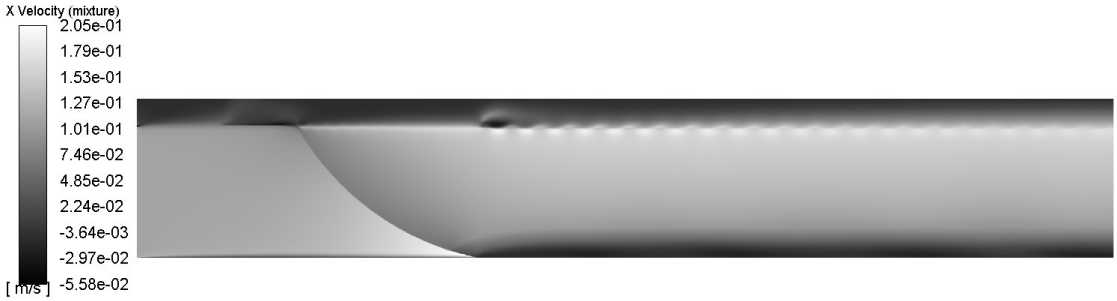

Figure B.5: Velocity contour plot resulting from the convex screen with a radius of curvature of 0.17m at a flow time of 15s.

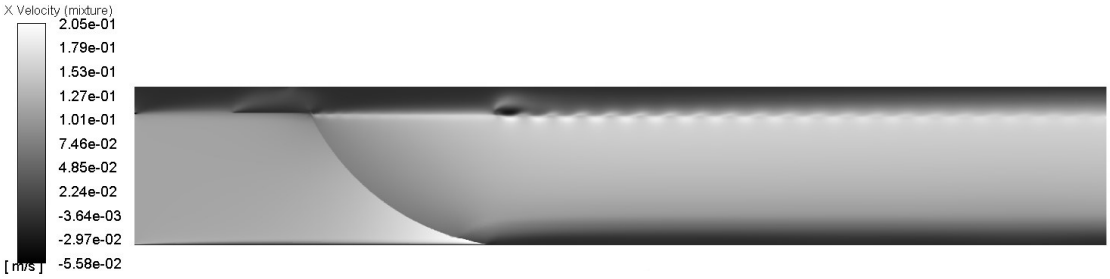

Figure B.6: Velocity contour plot resulting from the convex screen with a radius of curvature of 0.15m at a flow time of 15s.

B.2 Concave Screens

Figure B.7: Velocity contour plot resulting from the concave screen with a radius of curvature of 0.6m at a flow time of 15s.

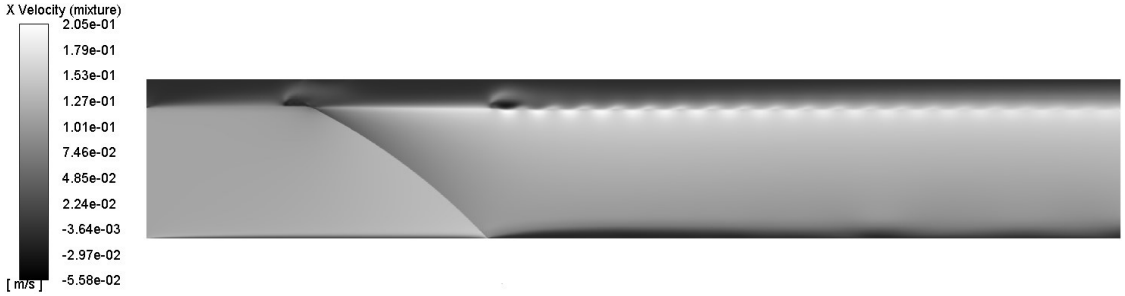

Figure B.8: Velocity contour plot resulting from the concave screen with a radius of curvature of 0.4m at a flow time of 15s.

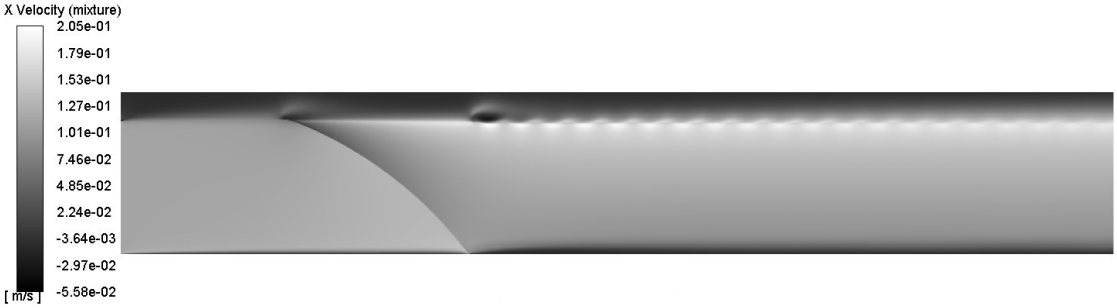

Figure B.9: Velocity contour plot resulting from the concave screen with a radius of curvature of 0.25m at a flow time of 15s.

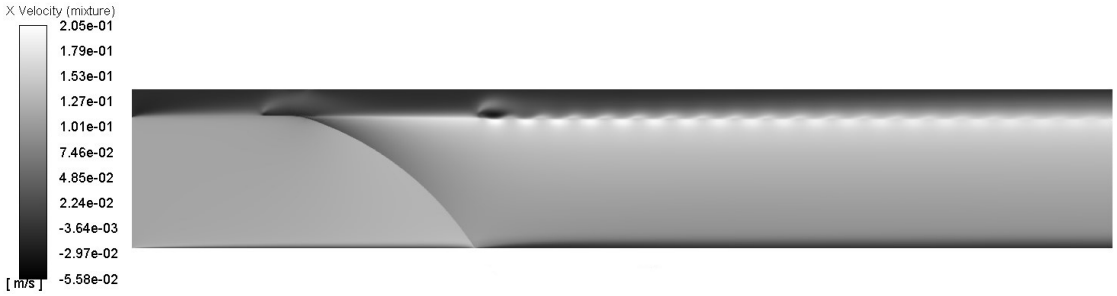

Figure B.10: Velocity contour plot resulting from the concave screen with a radius of curvature of 0.2m at a flow time of 15s.

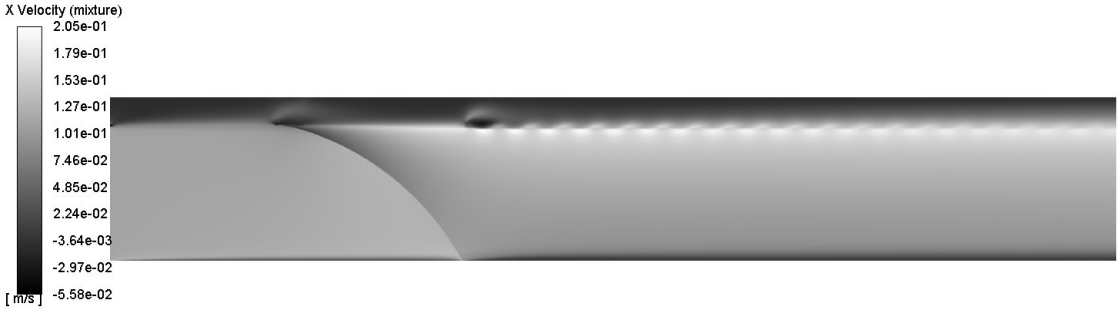

Figure B.11: Velocity contour plot resulting from the concave screen with a radius of curvature of 0.17m at a flow time of 15s.

Figure B.12: Velocity contour plot resulting from the concave screen with a radius of curvature of 0.15m at a flow time of 15s.

B.3 Straight Screens

Figure B.13: Velocity contour plot resulting from the straight screen mounted such that the angle between the screen normal and the streamwise direction is $\theta = 54°$ at a flow time of 15s.

Figure B.14: Velocity contour plot resulting from the straight screen mounted such that the angle between the screen normal and the streamwise direction is $\theta = 44°$ at a flow time of 15s.

Figure B.15: Velocity contour plot resulting from the straight screen mounted such that the angle between the screen normal and the streamwise direction is $\theta = 34°$ at a flow time of 15s.

B.4 Various Water Depths

Figure B.16: Velocity contour plot resulting from the lab set-up using a water depth of 0.08m at a flow time of 15s.

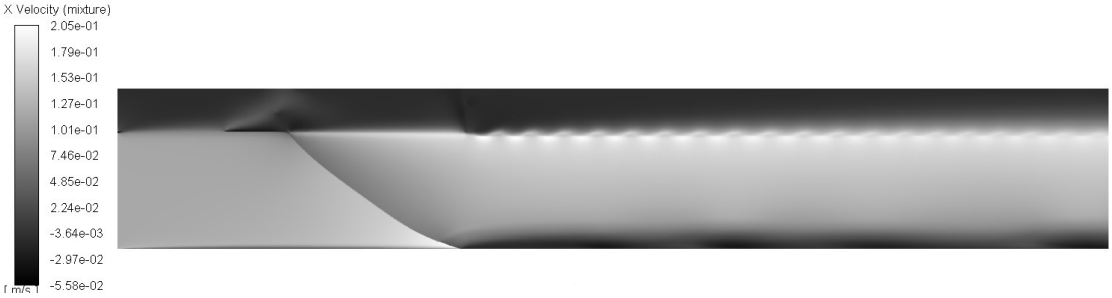

Figure B.17: Velocity contour plot resulting from the lab set-up using a water depth of 0.07m at a flow time of 15s.

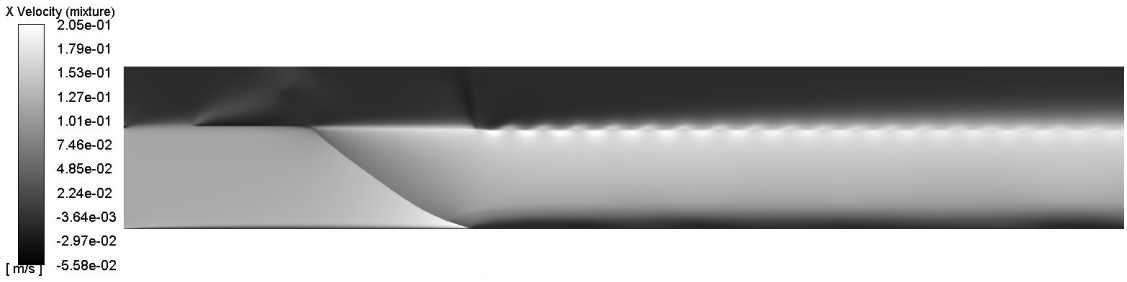

Figure B.18: Velocity contour plot resulting from the lab set-up using a water depth of 0.06m at a flow time of 15s.

B.5 Various Inlet Velocities

The contour plots are evaluated using the same boundaries for the normalized velocities, i.e. $\left(\frac{u(z)}{U_{inlet}}\right)_{min} = -0.875$ and $\left(\frac{u(z)}{U_{inlet}}\right)_{max} = 1.84$, in the legend.

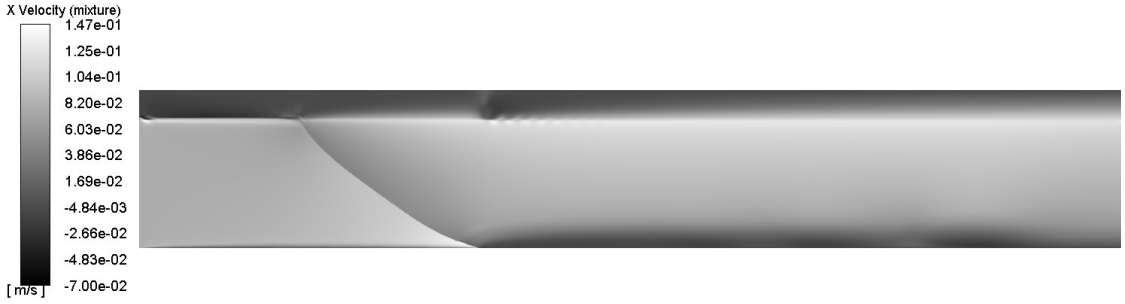

Figure B.19: Velocity contour plot resulting from the lab set-up using an inlet velocity of $0.08\frac{\mathrm{m}}{\mathrm{s}}$ at a flow time of 15s.

Figure B.20: Velocity contour plot resulting from the lab set-up using an inlet velocity of $0.12\frac{\mathrm{m}}{\mathrm{s}}$ at a flow time of 15s.

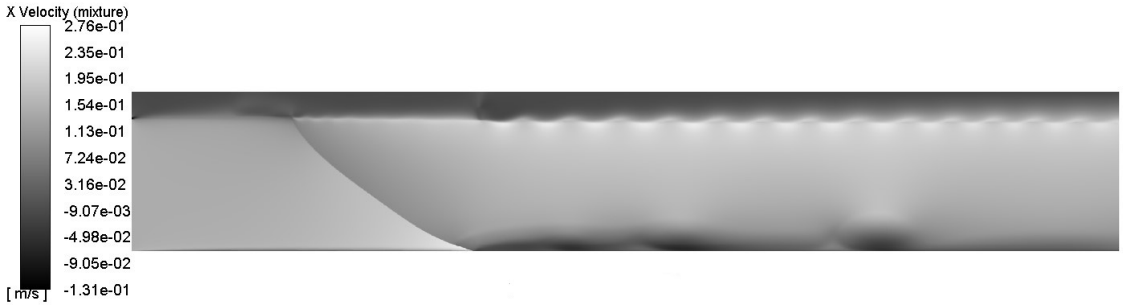

Figure B.21: Velocity contour plot resulting from the lab set-up using an inlet velocity of $0.15\frac{\mathrm{m}}{\mathrm{s}}$ at a flow time of 15s.